Patrik Ekström

A Dark Matter Search with AMANDA

Limits on the Muon Flux from Neutralino Annihilations at the Centre of the Earth with 1997-99 Data

Stockholm University
Department of Physics
2004

Patrik Ekström

A Dark Matter Search with AMANDA

Limits on the Muon Flux from Neutralino Annihilations at the Centre of the Earth with 1997-99 Data

Stockholm University
Department of Physics
2004

Doctoral Dissertation 2004
Fysikum
Stockholm University
Roslagstullsbacken 21
106 91 Stockholm

ISBN 91-7265-886-X
Printed by Universitetsservice US AB, Stockholm 2004

Abstract

The nature of the dark matter in the Universe is one of the greatest mysteries in modern astronomy. The neutralino is a nonbaryonic dark matter candidate in minimal supersymmetric extensions to the standard model of particle physics. If the dark matter halo of our galaxy is made up of neutralinos some would become gravitationally trapped inside massive bodies like the Earth. Their pair-wise annihilation produces neutrinos that can be detected by neutrino experiments looking in the direction of the centre of the Earth.

The AMANDA neutrino telescope, currently the largest in the world, consists of an array of light detectors buried deep in the Antarctic glacier at the geographical South Pole. The extremely transparent ice acts as a Cherenkov medium for muons passing the array and using the timing information of detected photons it is possible to reconstruct the muon direction.

A search has been performed for nearly vertically upgoing neutrino induced muons with AMANDA-B10 data taken over the three year period 1997-99. No excess above the atmospheric neutrino background expectation was found. Upper limits at the 90 % confidence level has been set on the annihilation rate of neutralinos at the centre of the Earth and on the muon flux induced by neutrinos created by the annihilation products.

List of refereed publications

[1] AMANDA Collaboration: E. Andrés et al., *The AMANDA Neutrino Telescope: Principle of Operation and First Results*, Astroparticle Physics **13** (2000) 1

[2] AMANDA Collaboration: E. Andrés et al., *Observation of High-Energy Neutrinos Using Čerenkov Detectors Embedded Deep in Antarctic Ice*, Nature **410** (2001) 441

[3] AMANDA Collaboration: J. Ahrens et al., *Search for Supernova Neutrino-Bursts with the Amanda Detector*, Astroparticle Physics **16** (2002) 345

[4] AMANDA Collaboration: J. Ahrens et al., *Observation of High Energy Atmospheric Neutrinos with the Antarctic Muon and Neutrino Detector Array*, Physical Review **D66** (2002) 012005

[5] AMANDA Collaboration: J. Ahrens et al., *Limits to the Muon Flux from WIMP Annihilation in the Center of the Earth with the AMANDA Detector*, Physical Review **D66** (2002) 032006

[6] AMANDA Collaboration: J. Ahrens et al., *Search for Neutrino–Induced Cascades with the AMANDA Detector*, Physical Review **D67** (2003) 012003

[7] AMANDA Collaboration: J. Ahrens et al., *Search for Point Sources of High-Energy Neutrinos with AMANDA*, Astrophysical Journal **583** (2003) 1040

[8] AMANDA Collaboration: J. Ahrens et al., *Limits on Diffuse Fluxes of High Energy Extraterrestrial Neutrinos with the AMANDA–B10 Detector*, Physical Review Letters **90** (2003) 251101

[9] AMANDA Collaboration: J. Ahrens et al., *Search for Extraterrestrial Point Sources of Neutrinos with AMANDA–II*, Physical Review Letters **92** (2004) 071102

[10] The SPASE Collaboration and The AMANDA Collaboration: J. Ahrens et al., *Calibration and Survey of AMANDA with the SPASE Detectors*, Nuclear Instruments and Methods **A522** (2004) 347

[11] AMANDA Collaboration: J. Ahrens et al., *Muon Track Reconstruction and Data Selection Techniques in AMANDA*, Nuclear Instruments and Methods A (2004), Article in Press

Contents

Chapter 1

Introduction

Already in the infancy of extragalactic astronomy there were observations suggesting that the luminous matter seen with the optical telescopes of the day was not the main contribution to the matter content in the Universe. Over the past decades astronomy have developed new observational techniques in order to cover the full range of the electromagnetic spectrum from radio to X-rays and gamma rays. All of these new areas of astronomy have added new pieces to the puzzle and formed the picture that the Universe is indeed mostly filled with matter that does not emit any radiation. The investigations into the possible nature of this dark matter have involved several fields of physics where there has been a surge of theoretical and experimental research activity during the past decade and the next few years will see even more.

The AMANDA experiment have embedded an array of photomultiplier tubes at two kilometres depth in the ice sheet below the Amundsen-Scott South Pole station in Antarctica. This detector array observes the Cherenkov light that is produced as high energy muons traverse the surrounding ice. With the information of when and where Cherenkov photons are detected the muon direction can be ascertained and at the high energies in question this is highly correlated with the direction of the neutrino that induced the muon. The focus of this work is the search for muons with a dark matter origin at the centre of the Earth. Another related application of AMANDA data is the search for dark matter accumulating at the centre of the Sun [1]. The AMANDA collaboration have also searched after muons induced by cosmic neutrinos from specific point sources in the sky, like active galactic nuclei [2,3]. The high energy part of the diffuse background summed over all such sources have been investigated both by looking for neutrino induced muons [4] as well as cascades [5]. Other analyses have examined the data for signals from gamma ray bursts [6], ultra-high energy neutrinos [7], magnetic monopoles [8] and supernovae [9]. Studies have also been performed on the prin-

cipal backgrounds of the neutrino telescope, the atmospheric muons [10–12] and the atmospheric neutrinos [13–15].

This thesis is structured as follows. In chapter 2 the observational evidence behind the dark matter problem as well as some of the potential dark matter candidates will be reviewed briefly. The various approaches of experiments that have been trying to detect these candidates are also presented. This will be followed in chapter 3 with an overview of the AMANDA experiment, the physics behind the neutrino telescope built in ice and the techniques involved in its operation. As part of my work in the AMANDA collaboration I have participated in three Antarctic expeditions in the summer seasons 1997-98, 1998-99 and 2000-01. The work centered on the timing and geometry calibration of the detector but also involved work during the deployment of strings 11-13.

Chapter 4 and chapter 5 describes the tools used for simulation and event reconstruction in this analysis. Chapter 4 also details the amount of simulations that I have performed for this work. The procedure used for data selection in each of the three years included in the analysis is laid out in chapter 6 and the details of my data analysis is contained in chapter 7. The final results for the 90 % confidence level upper limits on the muon flux from neutralino annihilations at the centre of the Earth are calculated in chapter 8. The obtained limits are discussed in chapter 9.

Chapter 2

Dark Matter and Neutrino Astrophysics

2.1 Dark Matter

2.1.1 The Dark Matter Problem

The study of the large-scale mass distribution of galaxies and clusters of galaxies is intimately connected with the determination of the total mass content of the Universe. Or rather the total energy density of the Universe.

In the early days of extragalactic astronomy in the 1930s the masses of galaxies, or *nebulae* as they were still called after the Latin word for cloud, were estimated using either their luminosities or their internal rotations.

In 1937 Fritz Zwicky [16] pointed out that these methods were unreliable as the luminosity could only be used for obtaining a lower limit on the mass and internal rotations could not alone be used for its determination.

Knowing the absolute luminosity of an object it is necessary to use a mass-luminosity relation to get the mass, but different kinds of stars and other luminous matter have different mass-luminosity relations. So in order to calculate the mass of the luminous material in a galaxy from its observed luminosity one needs to know its composition. The second problem pointed out by Zwicky was that of how much dark matter in the form of cool stars, solid bodies and gases a galaxy contains. Using the 18-inch Schmidt telescope on Mount Palomar Zwicky had already in 1933 [17] come to the conclusion that the large Coma cluster of galaxies needed more matter than could be observed directly in order to hold together.

He also suggested three methods that could be used for the mass determination of galaxies and clusters of galaxies [16–19]: the virial theorem of classical mechanics together with rotational velocities, gravitational lensing and a statis-

tical mechanics approach to the treatment of clusters of galaxies.

It was only decades later that the observational techniques had evolved to the point where velocity profiles could be made of galaxies out to tens of kiloparsecs. The rotational velocity versus radius is measured by observing Doppler shifts, either optically through spectral lines of ionised hydrogen (H II) or in radio by observing the 21 cm hyperfine transition of neutral hydrogen (H I). In particular the nearby spiral galaxy of Andromeda (M31) was studied in detail in the seventies, optically by Rubin and Ford [20] and in radio by Roberts and Whitehurst [21] and it was discovered that the rotational velocity was constant between 20 and 30 kpc.

Almost all of the visible mass of M31 is contained inside 20 kpc and if this was the total mass then the rotational velocity v_{rot} would depend on the radius r as $v_{rot}(r) \propto 1/\sqrt{r}$ for radii larger than 20 kpc. The fact that it does not show such a Keplerian fall-off with radius is a clear indication that there is a substantial mass contribution outside of the visible mass. This characteristic behaviour of the velocity profile has been seen in countless spiral galaxies since then (e.g. see Fig. 2.1) as well as in other types of galaxies. The outer regions of elliptical galaxies could not be studied in the same way as in spirals, instead their dynamics were investigated through X-ray observations of hot ionised gas envelopes [23].

The study of the dynamics of regular clusters of galaxies also showed that their mass was dominated by something other than the optically visible matter confirming with better precision the findings from the 1930s, for the Coma cluster the ratio of the observed to the dark matter was estimated as 1 to 7 [24].

X-ray observations of clusters provide an independent analysis of their dynamics, like elliptical galaxies clusters are filled with hot ionised gas emitting X-ray radiation through thermal bremsstrahlung which can be used to determine the mass, both of the gas and the total mass of the cluster. For regular clusters the gas content is 10 – 30 % of the total mass which is of the same order as the optically visible mass ($\sim$ 10 %) [25].

A third method to estimate the total mass of galaxy clusters comes from observing gravitational lensing effects of background galaxies, for weak lensing the lensed image of an object will be slightly distorted and by measuring galaxy ellipticities it is possible to reconstruct the surface density of the lens [26]. The deduced mass is in agreement with that of the previous two methods [27].

The total mass of clusters can be accounted for by the combination of all mass in the elliptical and spiral galaxy members and their large halos and the intracluster gas [28]. So the dark matter in galaxy clusters resides with the galaxies and furthermore this seems to be the case on even larger scales [29].

There are also more indirect clues for the presence of dark matter in the Universe. The energy density, Ω, is defined as $\Omega = \rho \ / \ \rho_c$ where ρ_c is the

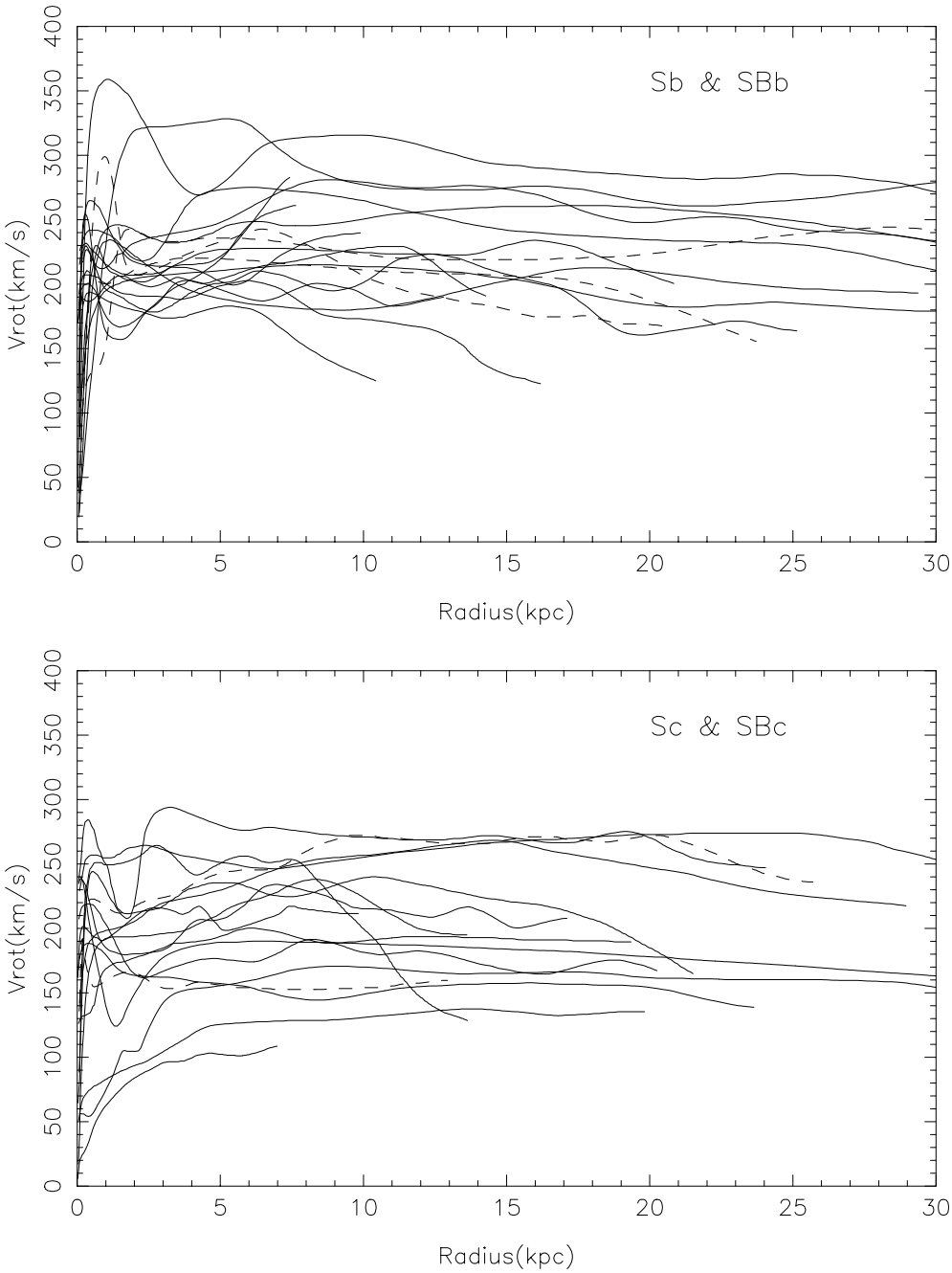

Figure 2.1: The rotational velocity as a function of radius for a selection of spiral galaxies. Figure taken from [22].

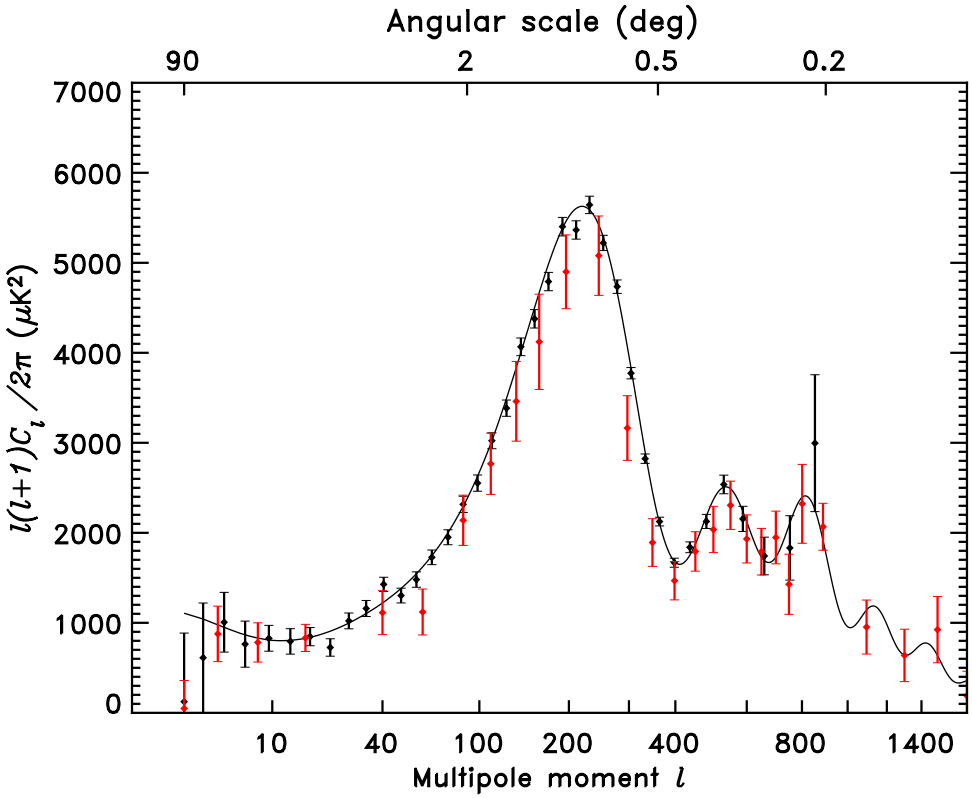

Figure 2.2: The WMAP combined angular power spectrum (black dots) compared with all previous CMB measurements combined (grey diamonds) as well as the best fit to a ΛCDM model. Figure taken from [36].

critical density between a forever expanding or an eventually collapsing universe. Through the theory of Big Bang nucleosynthesis it is possible to get a one-to-one relationship between the abundance of deuterium in the universe and the total baryon density. Observations of the deuterium level have been made on gas clouds in high-redshift quasars with the result [30,31] $\Omega_B h^2 = 0.020 \pm 0.002$ where $h = H_0$ / 100 km sec^{-1} Mpc^{-1}. With the present best value for the Hubble constant, $H_0 = 67$ km sec^{-1} Mpc^{-1}, that means $\Omega_B = 0.045$. The total matter content of galaxies and galaxy clusters give $\Omega_M \simeq 1/3$. Therefore it would seem that most of the matter in the universe is nonbaryonic and out of the baryonic mass only around one-tenth is visible.

The 2.73 K cosmic microwave background (CMB) observed back in 1965 for the first time was one of the corner stone predictions of the hot Big Bang model for

the beginning of the Universe [32,33]. With the formation of large-scale structures in the early Universe the density variations would have left their mark on the CMB as temperature variations of the same order, these μK anisotropies were finally seen with the DMR experiment aboard the COBE satellite decades later [34]. The initial formation is a problem that currently requires nonbaryonic dark matter because of the small fluctuations measured. Ordinary matter could not produce the structures seen today from these, it would be necessary to have something not coupled with the primordial radiation that could cluster freely in the early stages of the universe and around which ordinary matter could become gravitationally bound once it decoupled from the radiation. The best observations to date were done with the WMAP satellite [35] launched in 2001. Comparing the angular power spectrum data (see Fig. 2.2) with cosmological models the parameters for the best fit model is [37] $h = 0.72 \pm 0.05$, $\Omega_B h^2 = 0.024 \pm 0.001$ and $\Omega_M h^2 = 0.014 \pm 0.02$ confirming the conclusions about dark matter that have been drawn during the last decades.

So there is indirect evidence for the existence of dark matter in the Universe although the nature of it not known as it has not been directly detected or observed and is only seen through its gravitational effects. So what could the dark matter be?

2.1.2 Dark Matter Candidates

The earliest speculations on the nature of the dark matter of course centered on cool stars and gas as the likely culprit for the unseen matter. Later observations seem to have ruled out that such baryonic matter makes up any major part of the dark matter in the Universe, although it is clear that baryons do make up a part of it. It is at least as prominent as the luminous matter. The observations of high redshift quasars has shown that early in the history of the Universe baryons took the form of ionized gas. This is not seen at present so either it is still around in the form of ionised gas at a low temperature (difficult to observe) or it has condensed into unseen massive objects like brown dwarfs. Several experiments have searched for massive compact objects in the halo of our galaxy through the technique of microlensing, stars in the Large and Small Magellanic Clouds would become brighter for a short period of time if they were gravitationally lensed by an unseen massive object passing the line of sight. The results confirm that our galaxy's dark matter halo is not made up of objects lighter than 30 solar masses [38–41] although those could contribute to a small part of its mass.

Speculations on potential nonbaryonic dark matter candidates are abundant and there is a plethora of probable and improbable particles to choose from. Early on these fell into the three classes of hot, warm and cold dark matter [42]. Hot in

this respect means that the particles were in thermal equilibrium and relativistic at the time they decoupled from the radiation in the early Universe. The prime candidate for hot dark matter is a neutrino with a light mass of a few tens of eV or less which would have a relic density of the right magnitude to match the estimated Ω_M value. Warm dark matter would be made up of particles with a mass $m_X \sim 1$ keV and cold means that the particles were nonrelativistic when they lost thermal contact with the CMB and these would have a mass $m_X \gg 1$ keV.

Purely hot dark matter models have been ruled out by the CMB anisotropy measurements and the large-scale structure studies since structure formation would not be possible early on in these models. Warm dark matter scenarios are also incompatible with the WMAP results which favour cold dark matter, in particular the ΛCDM concordance model. But they could still constitute a minor part of the dark matter.

There are many very different candidates for the cold dark matter. One diverse category is that of the Weakly Interacting Massive Particle (WIMP). For a stable heavy neutral particle that were in thermal equilibrium at the time of decoupling the mass density at present is given by the annihilation rate [43,44] and for this to be of the right size to match the required dark matter mass density these particles would have to be interacting through the weak force. Some good WIMP candidates may be found in physics models beyond the standard model of particle physics, models of new physics predicting new particles.

The lightest supersymmetric particle (LSP) is the most studied dark matter candidate to date. In models with supersymmetry, which requires that each fermion has a bosonic superpartner and that each boson has a fermionic one [45], the LSP would unlike other superparticles be prevented from decaying. This is because of the conservation of its R-parity, the discrete symmetry which has a positive value for normal particles and a negative value for their superpartners. The neutralino is the LSP in the simplest models with conserved R-parity, and it is therefore a natural candidate since it is stable and as its mass and cross section is set by the weak scale $M_{weak} \sim 100$ GeV – 1 TeV it freezes out with the proper relic density [46,47]. The neutralino is the lowest mass state of the linear combination of the photino, zino and higgsinos (superpartners of the photon, Z^0 and Higgs bosons). There are many other possible dark matter candidates available from the vast zoo of supersymmetric models. Supergravity provides a low mass, O(keV), gravitino that could make up warm dark matter [48,49].

A similar concept to the LSP arises in models with extra dimensions where the lightest Kaluza-Klein particle (LKP) is stable and it is also a good solution to the dark matter problem.

A twist on the supersymmetric cold dark matter is the possibility that it

is made up of superweakly-interacting massive particles (superWIMPs) [58,59]. In some supergravity models the gravitino is the LSP and in those the next-to-lightest supersymmetric particle would decouple with the proper relic density and then these WIMPs would decay to gravitinos which only interact through gravity. Here models with extra dimensions also have a viable cold dark matter counterpart in the gravitons.

Another popular idea for the cold dark matter is the axion [50,51], originally introduced by adding a global symmetry to the standard model in order to make the strong interaction CP invariant [52–54]. This is a very light boson with a mass that is a fraction of an eV and it only very weakly interacts with ordinary matter. There are several different axion possibilities from theoretical models.

Although thermal relics from the Big Bang must obey a mass upper limit $O(100\,\mathrm{TeV})$ [55] particles that were not in thermal equilibrium at the time of decoupling do not [56]. So there are also categories of superheavy ($m_X > 10^{10}$ GeV) relic dark matter that can be explored. There are various weakly interacting as well as strongly interacting particles, the former are collected under the term wimpzillas [56] and the latter under simpzillas [57].

Superheavy dark matter candidates are also available in string and M theory. There are different mechanisms invented for the supersymmetry breakdown and one result of them is a hidden sector that only interacts with the observable weak-scale sector of particles extremely weakly. One good candidate is the cryptons which are stable or metastable bound states of matter in the hidden sector of string theory [60]. The lightest crypton could have the right mass and get the right relic abundance through gravitational interactions with the vacuum.

2.2 Dark Matter Detection

So there is clear evidence that there is a lot of dark matter in the Universe and there are plenty of theoretical candidates but how can it be detected and what kind of experiments can reveal its nature?

The dark matter candidates that only interact through gravity are impossible to detect directly but some of them give distinct signatures that can be observed in the early Universe. The decays of WIMPs to gravitinos would diminish the ^{7}Li abundance from the Big Bang nucleosynthesis [61] as well as distort the CMB radiation slightly from that of a perfect black body [59]. A caveat with the first observable is that there are astrophysical processes that also consume ^{7}Li so abundance determinations are model-dependent and affected by their uncertainties [62].

Any hot dark matter component that is made up of cosmological neutrinos can also not be measured directly due to their low mass and energy. So the deter-

mination of their possible contribution has to rely on neutrino mass or oscillation experiments (to get the neutrino mass) together with theoretical arguments and models of the evolution of the Universe.

The experiments aimed at WIMP dark matter detection fall into the two categories of direct and indirect detection. The former is looking for dark matter particles scattering off nuclei inside a detector volume while the latter is looking for secondary particles created through pair-wise annihilation of the dark matter.

The search for axions is performed through direct detection experiments exploiting the fact that they have a coupling to electromagnetic fields and that they can convert to two photons in a strong field environment [63].

2.2.1 Direct Detection Experiments

In the direct WIMP searches the experiment measures the energy deposited by nuclear recoils in a target material. The WIMPs are supposed to scatter elastically off nuclei whereas background in the form of gammas from natural radioactivity scatter off electrons. A more difficult background is neutrons induced by cosmic rays or from the surroundings which also scatter off nuclei. To reduce this background most detectors are placed deep underground.

A slow moving galactic halo WIMP with a mass of $O(\text{GeV})$ could make a nucleus recoil with an energy of $O(\text{keV})$. The recoil energy will manifest itself in different ways depending on the material that the WIMP interacts in and the various experiments have chosen different approaches for measuring it as well as in finding ways to reduce the background.

Some experiments use sodium iodine scintillator material that converts the ionisation energy to optical photons which are then measured with photomultipliers. These scintillators are capable of pulse shape discrimination which means that it is possible to distinguish between different types of particles through the shape of the emitted light pulse. Other experiments use two measurement techniques in coincidence in order to separate the electron recoil energy deposits from the nuclei ones. Due to inefficiencies only a part of the recoil energy is converted to ionisation that can be measured in the detector either through scintillation or direct measurement through electrodes. For crystals the remaining energy is converted into phonons that can be measured as a temperature increase if the thermal background is low enough.

The DAMA/NaI experiment [64], which took data for seven years until 2002 and was located underground in the Italian Gran Sasso National Laboratory, consisted of 115.5 kg NaI(Tl) scintillator material as detector target encased in shielding to reduce the radioactive background. All components were carefully chosen for their low radioactivity. DAMA searched for WIMPs through

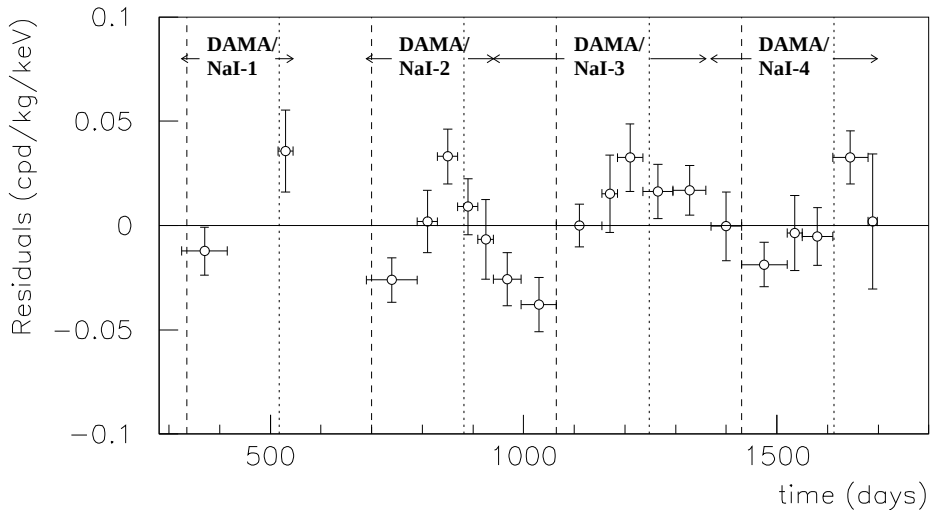

Figure 2.3: The possible annual modulation in count rate in the 2 – 6 keV energy region as reported by the DAMA/NaI collaboration. The dashed and dotted vertical lines represent the maxima and minima of the cosine for an expected WIMP signal. Figure taken from [65].

the annual modulation signature where the rate of WIMP induced recoils should show seasonal variations due to the Earth's motion around the Sun while passing through the galactic WIMP distribution. For the first four years with a total exposure of 57986 kg day they reported positive results for such a modulation [65] in the 2 – 6 keV energy range (see Fig. 2.3) at the 4 standard deviation confidence level. The claim is that it fits with a WIMP signal based on standard assumptions for the dark matter halo of our galaxy. The effects of varying some of these parameters have been investigated and different halo models tested producing greater ranges of possible WIMP masses and cross sections that could fit the data [66,67]. Another study points out that conclusions drawn on the WIMP mass and cross section can be incorrect if physically realistic models are not used [68]. There is some controversy over the DAMA results as other experiments (CDMS and EDELWEISS) have reported no signal for the WIMP region indicated by DAMA. A second generation detector DAMA/LIBRA using the same techniques but with $\sim$ 250 kg of NaI(Tl) as target material is currently being tested.

The Cryogenic Dark Matter Search (CDMS) and the EDELWEISS experiment

use setups similar to each other [69–72]. They are both bolometers that measure the heat as well as the ionisation induced by a scattering particle. CDMS are using both Ge and Si detectors while EDELWEISS are using only Ge. These are placed in a cryogenic environment at around 20 mK and particle interactions in the low-temperature Ge and Si crystals create phonons which are measured by attached heat sensors while the ionisation is collected with two electrodes. More specifically EDELWEISS is made up of three 320 g Ge detectors, although only one was used for the published analysis due to problems with the charge collection on two of them, and the experiment is placed deep underground in Laboratoire Souterrain de Modane in the Fréjus tunnel in the French-Italian alps. The crystals were shielded and low radioactivity material was used for surrounding equipment. The result was that no events were seen in the range 20 – 100 keV (one event was seen at 119 keV) with an exposure of 11.7 kg day and they exclude the DAMA candidate at more than 99.8 % confidence level using the same model assumptions.

The original measurement of CDMS used one 100 g Si and three 165 g Ge crystals and was made at the test site at the Stanford Underground Facility in California, USA, only 10 metres below the surface. The experiment is covered with shielding against radioactivity as well as a scintillator for a cosmic ray muon veto. The result was 13 events in the range 10 – 100 keV for 15.8 kg day of data [70]. To estimate the number of neutron background events they used simulations together with the rate of the Si detector, run separately, and the coincident rate of the Ge detectors and found that it agreed with the number of events observed. A new setup with four 250 g Ge and two 100 g Si detectors and an exposure of 28.3 kg day in the range 5 – 100 keV found 20 events [73], simulations again show that this is compatible with background from neutrons. A goodness-of-fit test exclude the most likely DAMA candidate at 99.98 % confidence level for standard WIMP interactions and dark matter halo parameters.

The Heidelberg Dark Matter Search (HDMS) [74,75] is also located in the Gran Sasso National Laboratory. The prototype used for the initial analysis was made up of a 200 g Ge inner target surrounded by a 2.1 kg Ge outer detector used for background rejection. Events which are seen in both the inner and the outer detector are thrown out since they are not the result of a WIMP-nucleon scatter in the inner detector. The WIMP limit after one year with 26.74 kg day of exposure is slightly better in the low-energy range than the earlier Heidelberg-Moscow experiment due to a lower energy threshold. The Heidelberg-Moscow experiment ran five ~ 2 kg Ge detectors at the same site searching for a neutrinoless double beta decay but also used one of them to look for WIMP scattering for three months [76].

Another Ge double beta decay experiment that is also used for a WIMP direct

detection search is IGEX [77] in the Canfranc Underground Laboratory in the Spanish Pyrenees. One of their 2.2 kg Ge detectors was used for 40 days to search for WIMP induced recoils. The detector was constructed with radiopure material components and surrounded by a lead neutron shielding and covered by a scintillator for a cosmic ray muon veto. With 80 kg day of data in the range 4 – 50 keV and the standard assumptions for the WIMP halo distribution and Earth's motion the obtained limit excludes part of the region of the DAMA candidate.

The results of CDMS and EDELWEISS has also been used to show that they rule out some simpzilla scenarios [78,79] under standard assumptions for the Earth's motion and the dark matter halo. The results indicate that the dark matter can only be made up solely of simpzillas if their mass is above 10^{15} GeV.

In the 1980s there were two similar US experiments performed in the search for cosmic axions at Brookhaven National Laboratory (BNL) [80] and at the University of Florida (UF) [81]. Both used a superconducting solenoid giving a $\sim$ 8.5 T magnetic field in a small ($\sim$ 15 cm diameter and 40 cm long), low temperature (2.2 K, 4.2 K) microwave cavity. The BNL experiment could scan the frequency range 1.09 – 3.93 GHz which corresponds to an axion mass range of 4.5 – 16.3 μeV and seeing no signal they set upper limits for the axion-photon coupling constant $g^2_{\mathrm{A}\gamma\gamma}$ and the galactic halo abundance. The UF setup could only investigate the mass range 5.4 – 7.6 μeV for which their coupling limits were lower than that of BNL, for the low mass end the limit was 3.3×10^{-28} GeV^{-2} at the 97.5 % confidence level. However, the sensitivity of both experiments were orders of magnitude away from the predictions from the standard axion halo models.

They were followed by a large-scale microcavity search [82] in the 1990s, placed at Lawrence Livermore National Laboratory in California, that have reached the sensitivity to explore realistic axion dark matter models. With a much larger cavity (50 cm diameter and 1 m length), a lower temperature (1.3 K) and a 7.6 T static magnetic field this experiment set a limit of $\sim 10^{-30}$ GeV^{-2} at 90 % confidence level for the coupling constant in the 2.9 – 3.3 μeV mass range.

2.2.2 Indirect Detection Experiments

The experiments that search for dark matter particles indirectly do so by looking for the products of their pairwise annihilation. If the dark matter halo of our galaxy is made up of WIMPs then some of them should scatter elastically off nucleons in stars or planets and loose enough momentum to become gravitationally trapped. These WIMPs would collect at the centre of these objects and as they are Majorana particles they are their own anti-particles and would eventu-

ally pairwise annihilate. Among the products would be neutrinos that could be detected. The accumulation would give relatively high densities of WIMPs and an increased annihilation rate. Another place where the density of WIMPs could be higher is near the centre of the galaxy, in certain halo models there could be even be density spikes or cusps where the annihilation rate would be high enough for a noticeable flux of gamma radiation to be produced. The rate of annihilation of WIMPs in the halo in general is substantially lower but apart from neutrinos and gammas it would also generate positrons and anti-protons that could be measured. If the halo distribution is not smooth but the WIMPs instead are clumped together in high density dark matter pockets then there could be a noticeable flux, especially if such clumps are located nearby.

The gamma radiation from WIMP annihilation near the galactic center can take two different forms. It can be monochromatic if the annihilation is into $\gamma\gamma$ or $Z^0\gamma$ or continuous if the photons are produced by secondary processes like π^0-decays (e.g. π^0s produced in the quark jets after WIMP annihilation into $q\bar{q}$). The monochromatic emission is suppressed and although distinct, since there is no background from standard astrophysical processes, it is expected to be weak if not enhanced through some very high density regions like cusps or spikes. The continuum emission is stronger and a WIMP dark matter halo would show an excess from the centre of the galaxy depending on the halo model. The overall diffuse contribution from annihilations in the halo could also show an excess if the dark matter was clumped [83].

Data from the EGRET instrument onboard the Compton Gamma Ray Observatory satellite show a strong excess of gamma ray emission in the direction of the galactic centre [84] above the diffuse component expected from standard processes. EGRET has also measured the extragalactic component of the gamma ray flux up to 100 GeV [85] but a signature of a diffuse contribution from WIMP annihilation in extragalactic halos will need higher resolution and might need higher energies in order to be seen [86].

A 511 keV emission line was observed in the same direction for the first time in 1972 and has been studied several times since then, the latest measurement with the SPI spectrometer on the European INTEGRAL satellite [87] have now shown that a single compact object is ruled out as the emitter.

Non-observation of gamma-rays with energy above 1 GeV in the direction of the Draco dwarf galaxy with EGRET has been used to set model dependent limits on neutralino dark matter [88].

The HEGRA collaboration using their system of five imaging atmospheric Cherenkov telescopes on the island of La Palma have searched for TeV gamma ray emission from the centre of the Andromeda galaxy [89] but found no evidence of any monochromatic signal.

WIMP annihilations in the halo could also produce positrons that would leave a very distinct mark on the cosmic ray positron spectrum [90], the excess would produce a clear bump in a plot of positron fraction ($e^+/(e^-+e^+)$) versus positron energy. The HEAT (High-Energy Antimatter Telescope) [91] balloon experiment did find indications of such an excess in their 1994 and 1995 measurements although more data is needed to draw any conclusions. A smoothly distributed standard WIMP halo would not be able to account for the excess in the HEAT measurement since the predicted positron flux is too low while a clumpy halo could do this [92,93].

The flux of antiprotons from WIMP annihilations would be higher than that of positrons but it would not come in the form of such a clear signature [94]. The cosmic ray antiproton energy spectrum has been measured by BESS [95], another balloon experiment, and no indications of a contribution from dark matter is seen.

For WIMPs trapped and annihilating inside massive compact objects most annihilation products are quickly absorbed. The only particles that can escape and be detected are high energy neutrinos. A flux of these coming from the centre of the Earth or the Sun would thus be one signature of WIMP dark matter. Neutrino telescopes actually look for neutrino induced muons that are created when the muon neutrinos interact around the detector. Since muons do not propagate far in the Earth any muons that can be identified as upgoing must originate from a muon neutrino interaction. There is an irreducible background for such neutrinos coming from the atmosphere on the other side of the Earth where cosmic ray interactions generate muon neutrinos. So an experiment would have to look for an excess above the background events. No such excess has been observed.

The experiments that have looked for this WIMP signature have different approaches to the muon tracking. The Baksan underground scintillator telescope took 10.55 years of data between 1978 and 1993. A search within a 30° angular cone in the direction of the centre of the Earth and the Sun [96] resulted in 69 events observed from the Earth with an expectation of 71 from atmospheric neutrinos and 23 events from the Sun where 24 ± 2 was expected.

The Macro detector was located in the Gran Sasso National Laboratory and took data from 1989 to 1999. It consisted of a large volume of streamer tubes and scintillation counters used for particle tracking and timing respectively and absorbers to give a ~ 1 GeV energy threshold [97]. Time-of-flight was used to separate upward- and downward-going muons. From the Earth they observed a deficit of events near the vertical angular region of interest for WIMPs but after renormalisation presented limits on the muon flux from WIMPs. From the Sun the observation matched the expectation from Monte Carlo simulations.

The Super-Kamiokande detector is a 50 kton cylindrical water tank placed

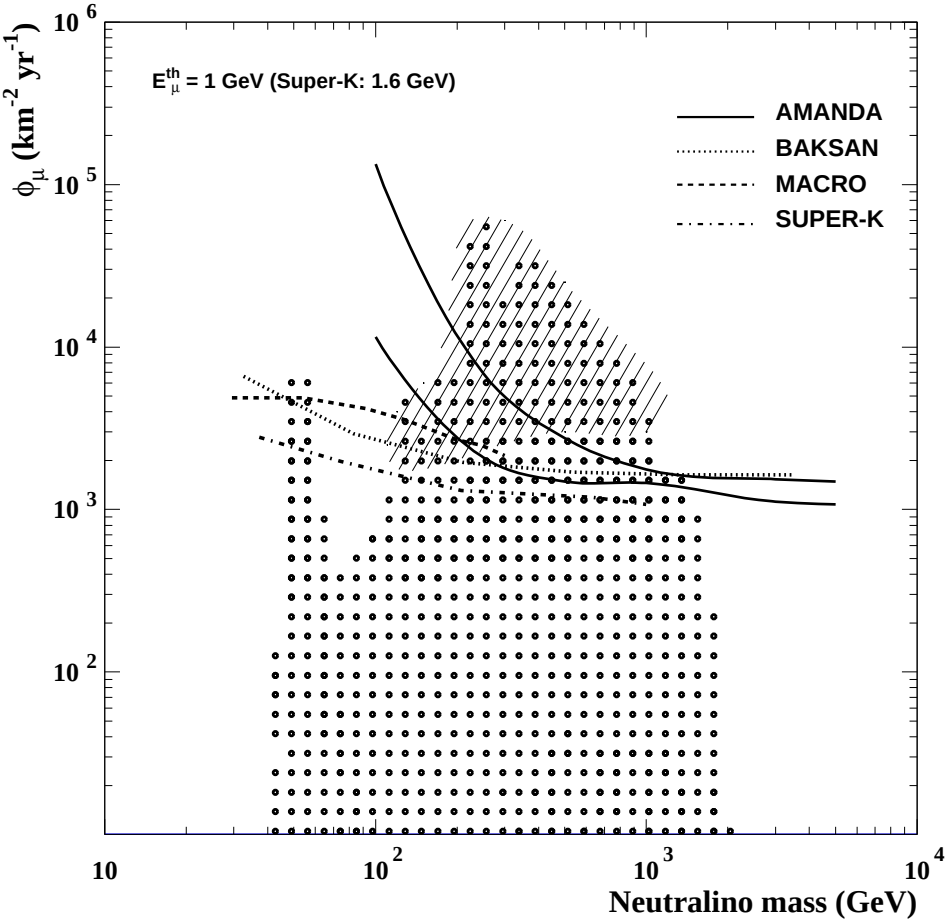

Figure 2.4: Limits on the muon flux from neutralino annihilations at the centre of the Earth from AMANDA, Baksan, Macro and Super-Kamiokande. The dots represent the predictions of various supersymmetric models and the shaded area indicates models excluded by the DAMA result. The two limits given for AMANDA represent two extreme annihilation cases. Figure taken from a previous publication [104].

deep underground in the Kamioka mine, Japan [98,99]. The volume is divided into an inner detector part and an outer cosmic ray veto part by a barrier of inward- as well as outward-facing photomultiplier tubes. It takes advantage of the fact that the high energy muons will emit Cherenkov light when passing through the water, the arrival times of this light is then used to reconstruct the muon trajectory. The result for 1268 days of livetime was that no significant excess above the atmospheric neutrino background expectation was found from the Earth, Sun or toward the galactic centre [100].

The Baikal neutrino telescope [101] is also a water Cherenkov detector but unlike Super-Kamiokande the optical sensors are placed deep underwater in a lattice formation throughout a large instrumented volume in Lake Baikal, Russia. The data from 1996, 1998 and 1999 with the NT-200 array give a limit that is higher than those of the other experiments [102].

The AMANDA neutrino telescope [103] is a large ice Cherenkov detector buried deep in the Antarctic glacier at the South Pole. It will be described in more detail in the next chapter. The limit on the neutrino induced muon flux from neutralino annihilations at the centre of the Earth obtained with the first year of data of the AMANDA-B10 array [104] is shown in Fig. 2.4. The result is also compared with that of Baksan, Macro and Super-Kamiokande as well as with supersymmetric model predictions.

Chapter 3

The AMANDA Experiment

Observing the high energy neutrino sky has been a goal for a couple of decades [105–107] as it would open up a new and very interesting window to the Universe.

Extremely high energy gamma and cosmic rays have been detected and it is anticipated that the processes generating them would also yield neutrinos of similar energies. The cosmic rays interact with galactic and intergalactic magnetic fields which will deflect them on their way to Earth. Photons will not be deflected but on the other hand they cannot traverse intervening matter. As neutrinos only interact through the weak force neither of these drawbacks will affect them and they would point right back to the source regions. Neutrinos are generated by charged pion decays, pions being produced when the ultra-high energy cosmic rays and photons interact with target material in cosmic accelerators (e.g. active galactic nuclei and gamma ray bursts), the interstellar medium or the atmosphere of the Earth. As illustrated in the previous chapter the neutralino dark matter candidate is also a possible source of high energy neutrinos.

The aim of the Antarctic Muon And Neutrino Detector Array (AMANDA) collaboration has been to build and operate a high energy neutrino telescope in the glacial icecap at the geographical South Pole. The first tests performed in Greenland in 1990 [108,109] were followed by in situ tests at the South Pole in 1992-93. This demonstrated the feasibility of ice as a medium for a large neutrino detector at a reasonable cost. The experiment has since then been brought to completion in stages during the 1990s until the final elements of the AMANDA detector were deployed in February 2001. Work is already underway for the next phase of large-scale neutrino telescopes, the IceCube collaboration is building on the development done for AMANDA and will construct a kilometre sized array at the same location between 2004 and 2008.

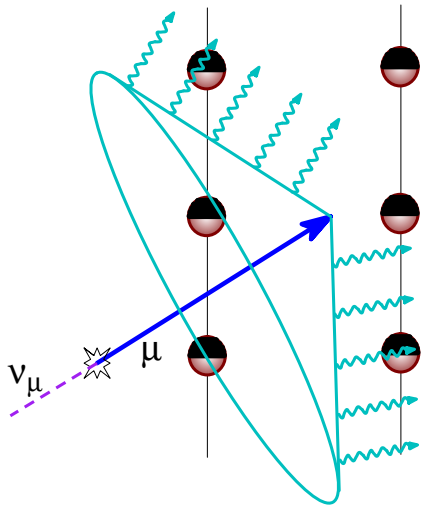

Figure 3.1: As the muon travels through the ice with a velocity exceeding that of light, c_{ice}, it emits Cherenkov photons. The light cone formed is here illustrated travelling through the AMANDA detector hitting the OMs in a time sequence.

3.1 Method of Detection

The working principle of the neutrino telescope is to detect the Cherenkov light emitted by a high energy muon as it travels through a transparent medium. Using light detectors with good timing resolution located in that medium it is possible to reconstruct the direction of the muon if enough detectors are hit by light from the Cherenkov cone (see Fig. 3.1). High energy muon neutrinos are capable of travelling through the Earth which muons with their relatively short absorption lengths are not. A neutrino telescope is therefore designed to look down as upgoing muons must have been produced by charged current neutrino-nucleon interactions below it. Although the cross section is very small the flux of neutrinos is estimated to be sufficiently large so that upgoing muons will be detectable if a big enough volume is instrumented (with the appropriate spacing depending on the optical properties of the medium in question).

3.1.1 Muon and Photon Propagation

A charged particle propagating through a medium with a velocity exceeding that of the speed of light in that medium will emit Cherenkov radiation at fixed angle relative to the trajectory. This Cherenkov angle θ_c is determined by the refractive index n of the medium and the velocity of the particle through the relation

$$\cos\theta_c = \frac{1}{\beta n}. \tag{3.1}$$

where $\beta = v/c$ and c is the velocity of light in vacuum.
The Cherenkov photons are the main directional information used in reconstructing the muon track but the energy loss due to this process is negligible. The energy loss of very high energy muons is dominated by the three main stochastic processes bremsstrahlung, pair production and photonuclear interactions. Bremsstrahlung is the radiation of high energy photons when the relativistic muon interacts with the electric field of the atoms. The muons can also create an e^+e^--pair through an exchange of a virtual photon with nuclei or interact with the nuclei via a real or a virtual photon creating hadrons. The continuous ionisation energy loss is less important at the very high energies but it is the dominating energy loss process at lower energies. The average muon energy loss per distance travelled in a medium can be approximately described by

$$-\frac{dE}{dx} = a(E) + b(E)E \tag{3.2}$$

where $a(E)$ represents the ionisation energy loss and $b(E)E$ the stochastic. The two parameters a and b only vary slightly with energy and are mainly dependent on the medium at hand. The stochastic energy losses will appear as bursts of light at points along the muon track as the electromagnetic or hadronic products cascade. Since the muons are relativistic most of these secondaries will be relativistic as well and boosted in the same direction they will produce Cherenkov radiation that will roughly coincide with the angle of the parent muons.

The average distance a muon of a given energy E_μ will be able to propagate through a medium can be estimated through integration of Eq. (3.2), under the assumption that a and b are constant, to be

$$\langle d_\mu \rangle = \frac{1}{b}\ln\left(1 + \frac{b}{a}E_\mu\right). \tag{3.3}$$

A fit of Eq. (3.2) to a full simulation of muon energy loss in ice, which will be discussed in more detail in the next chapter, expressed in metres water equivalent (mwe) gives [12,110] $a = 2.6 \times 10^{-1}$ GeV mwe^{-1} and $b = 3.6 \times 10^{-4}$ mwe^{-1} for

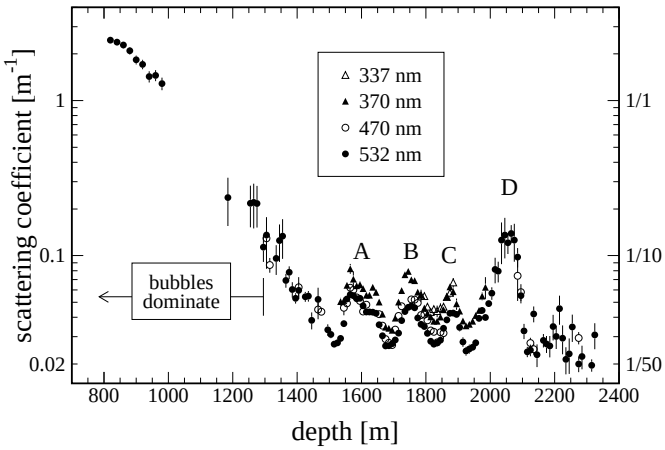

(a) The variation of the effective scattering coefficient with depth. Bubbles in the ice dominate at depths above 1300 metres. Peaks in the scattering A, B, C and D have been identified with dust peaks in Vostok and Dome Fuji data [114].

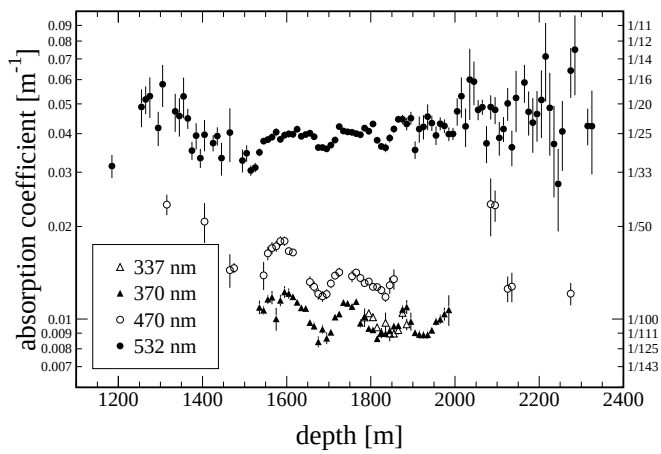

(b) The absorption coefficient have a strong wavelength dependence but does not vary as strongly as the scattering coefficient with depth.

Figure 3.2: The measured ice properties (preliminary results) at the South Pole as a function of depth at four different wavelengths [115]. See [113] for details on the method and results at 532 nm.

energies between 20 GeV and 10^{11} GeV. Therefore a 100 GeV muon will on average have a range of ~ 360 mwe.

The photons produced in energy loss processes will propagate through the deep Antarctic glacial ice before they can be detected by AMANDA. It is therefore crucial to fully understand the effects of the scattering and absorption of photons in the ice on their measured arrival time distributions at the individual light detectors. Scattering will increase the path length of the photon and shift parts of the distribution to later times while absorption of course will remove photons. A lot of work has gone into determining the ice properties in and around the detector and the scattering and absorption of the ice have been measured between the depths of 800 m and 2300 m [111–113]. The ice formed through snow accumulation on the surface followed by subsequent compactification with depth, this means that climatological changes in the past can show up as changes in the ice properties with depth. Impurities in the ice can act as both scattering centres and absorbers while the ice itself can only absorb although this latter effect only concerns wavelengths outside the region of observability of the AMANDA light detectors. The photon flux at a distance d from the source can be expressed through $\phi_\gamma = e^{(-d/\sqrt{\lambda_a \lambda_e/3})}/d$ where λ_a is the absorption length and λ_e the effective scattering length of the ice. The effective scattering length depends on the mean of the cosine of the scattering angle θ at each interaction and the geometrical distance between scatterings λ_g as $\lambda_e = \lambda_g(1 - \langle\cos\theta\rangle)^{-1}$.

The measurements were performed with both pulsed and continuous light sources *in situ*, i.e. these light sources were deployed together with the light detectors [111–113]. The pulsed light was used to determine the scattering and absorption independently of each other. Data recorded with the light detectors was compared to a range of ice properties through Monte Carlo simulations and a chi-square minimisation gave the ice parameters that best fit the data. The bulk of data was taken with light at 532 nm supplied by a dye laser at the surface and sent down through optical fibres to diffuser balls placed nearby the light detectors down in the ice. This setup allowed the full depth range of the detector to be probed. Pulsed data was also taken at three other wavelengths, 337 nm from N_2 lasers buried at two locations at the bottom of the array and 370 nm and 470 nm from LEDs installed above some of the light detectors. While scattering is virtually independent of wavelength absorption is not, so continuous DC light sources at other wavelengths were used to determine the product $\lambda_a\lambda_e$ and using the scattering from the pulsed measurements this allowed the determination of the absorption. The measured ice properties expressed through the absorption and effective scattering coefficients a and b_e, defined as the inverse lengths $a = \lambda_a^{-1}$ and $b_e = \lambda_e^{-1}$, are shown in Fig. 3.2 (preliminary results [115]).

3.1.2 Neutrino Interactions

The muons are generated by a muon neutrino or anti-neutrino interacting with a nucleon, a charged current interaction through the exchange of a W^+ or W^- with one of the constituent quarks. The quark will then hadronise so that the end product of the incoming neutrino that undergoes deep inelastic scattering off a nucleon will be an outgoing muon accompanied by a hadronic shower.

Due to the relativistic nature of the interaction the neutrino and muon will have almost the same direction, the angular deviation between the neutrino and muon trajectories is $\theta_{\nu\mu} \sim 1.5/\sqrt{E_\nu}$ with E_ν in TeV [13].

The neutrino-nucleon charged current cross section at high energies can be calculated in the standard model of particle physics. It is dependent on the parton distribution functions describing the fine structure of the nucleons in terms of the constituent quarks and gluons. The best fine structure measurements has been made by the ZEUS and H1 experiments at the HERA electron-proton collider located in DESY, Hamburg, Germany and by the DØ experiment using the Tevatron p$\bar{\text{p}}$-collider at Fermi National Accelerator Laboratory, USA. The functions are parametrised by the interacting parton's fraction of the nucleon momentum x and by the energy-momentum transfer Q^2. With the two Bjorken scaling variables x and $y = (E_\nu - E_\mu)/E_\nu$ the differential charged current cross section for a neutrino with energy E_ν creating a muon with energy E_μ can be expressed as [116]

$$\frac{d\sigma^{CC}}{dxdy} = \frac{2G_F^2 M E_\nu}{\pi}\left(\frac{M_W^2}{Q^2 + M_W^2}\right)^2 [xq(x,Q^2) + x(1-y)^2\bar{q}(x,Q^2)] \tag{3.4}$$

where q, $\bar{q}$ are parton distributions, M and M_W are the nucleon and W masses and G_F is the Fermi constant. Up to neutrino energies of 10^{16} eV, which is above the energy region of interest in this work, the parton distribution functions and thereby σ_{CC} have been determined through measurements. For higher energies the cross section have been extrapolated from theory although the uncertainties are substantial for ultra-high energies $\sim 10^{21}$ eV [117].

The neutral current cross section is smaller than the charged current one but still large enough that neutral current interactions can reduce the energy as well as alter the direction of high energy neutrinos while propagating through the Earth. The Earth is even opaque to ultra-high energy neutrinos [117].

3.1.3 Atmospheric Muons and Neutrinos

A cosmic ray interacting with a nucleus in the upper atmosphere produces showers with plenty of secondary pions and kaons that decay and generate muons and

muon neutrinos. In order to reduce the amount of cosmic ray muons that go through a muon detector searching for muons from other sources scientists have gone deep underground. Although the high energy muons can penetrate several kilometres underground most cosmic ray muons are relatively low energy and detectors can be shielded from the major part if they are placed below a kilometre or two of overburden. But even after avoiding the brunt of this background by going deep underground it will still outnumber the expected number of neutrino induced muons by many orders of magnitude at the depth of AMANDA. With one to two kilometres of ice acting as shielding these downgoing atmospheric muons are still about a factor of 10^5 more numerous than the upgoing muon signal.

Neutrinos generated by cosmic ray showers in the atmosphere on the opposite side of the Earth will be impossible to distinguish from cosmic or WIMP induced neutrinos on an individual basis. But due to the different ways in which they are generated the energy spectra will have different slopes and in fact cosmic neutrinos are expected to dominate over the atmospheric above energies of 10 TeV. The atmospheric neutrinos can be made good use of since they are a known source that has to be there and their observation is on one hand a proof that detectors are working and on the other hand they can be used for calibration. The observation of atmospheric neutrinos by AMANDA [13,14] was proof that large under-ice neutrino telescopes can and do work. For WIMP searches any potential signal will have be observed as an excess above this background of atmospheric neutrinos.

3.2 The Detector Array

The first stage of construction was undertaken in the 1993-94 Antarctic summer season (November to February) and resulted in a four string detector instrumented with optical modules (OMs) between depths of 800 and 1000 metres. The OMs (see illustration in Fig. 3.3) consists of 8 inch photomultiplier tubes (PMTs) encased in glass spheres that act as protection against pressure. A silicon gel is placed between the PMT cathode surface and the surrounding glass in order to minimize the optical losses. Most of the PMTs used in AMANDA are Hamamatsu R5912-2 (with 14 dynodes) although a few Thorn EMI 9353 were also deployed for evaluation. Two different types of glass spheres have been used, a 12 inch diameter sphere from Billings was used early on and this was subsequently replaced by a 13 inch sphere from Benthos for the later stages of the array.

The main design element of AMANDA is the string. The OMs are mounted on the last few hundred metres of a one to two and a half kilometre long coaxial or twisted quad cable with one and a half inch diameter. The cables are used

both for supplying the high voltage to the PMTs as well as retrieving the PMT signals. In order to deploy the strings to the desired depths, the Polar Ice Coring Office (PICO) used a high-pressure hot water drill to melt 60 cm wide holes in the ice into which the strings were lowered and then allowed to freeze in.

It was discovered that the optical properties above one thousand metres depth were not as satisfactory as had been predicted before deployment. The problem found was a very short effective scattering length on the order of decimetres which effectively randomized the direction of the Cherenkov photons so that the muon trajectories could not be reconstructed [111,112].

Air, profuse throughout the snow of the firn layer just below the surface, will form bubbles as it is trapped when the firn transforms into ice. The size and concentration of the bubbles in the ice depend mainly on pressure and therefore depth. At first the bubbles only decrease in size with depth while their concentration remains constant but as sufficient pressure is reached it induces a phase transition of these bubbles into air hydrate crystals diluting them so that below a certain depth no bubbles remain [118]. The difference of refractive index between the air hydrate and the ice crystals is very small (around four permille) so the scattering off these will become negligible. At depths below 1400 metres it is other contaminants in the ice that will scatter and absorb the photons, namely salt and mineral grains, acid droplets and soot [118].

The first detector, called AMANDA-A, was still found to be useful. The extensive studies to understand the ice properties of the detector medium [111,112] showed that it could not be used in the designed manner of reconstructing muon directions although the ice made it even better for use in a calorimetry fashion. Unlike the high energy muons that have a mean range in the ice of 10^2 – 10^4 metres, electrons created by ν_e and $\bar{\nu}_e$ interactions loose all their energy in an electromagnetic cascade ranging only metres. The short scattering length and very long absorption length was taken advantage of in an analysis putting upper limits on the flux of $\nu_e + \bar{\nu}_e$ [119]. However, the plug was later pulled on the AMANDA-A part of the detector and the corresponding surface electronics removed.

During 1995-96 four more strings were deployed, going as deep as 2000 metres in order to avoid the bubbles. Each string contained twenty OMs spaced twenty metres apart, starting at a depth around 1600 metres for the top module.

As the ice properties were deemed to be satisfactory with an absorption length of around 100 metres and an effective scattering length of 25 metres [113] another six strings were deployed at the same depth in 1996-97 but spread out in pairs on a circle with radius 60 metres around the first four. While the first four were coaxial cables these six were twisted quad cables, allowing each string to support 36 modules. The OMs on the first four deep strings have glass spheres

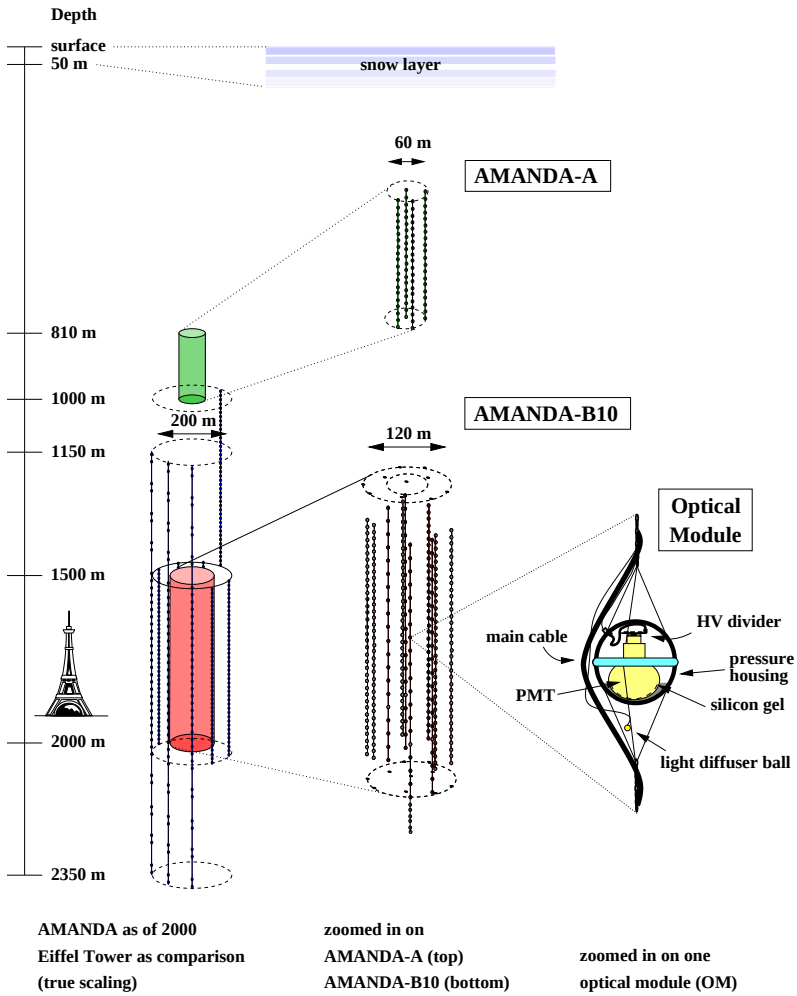

Figure 3.3: The AMANDA-II detector layout.

manufactured by Billings while the latter six have spheres from Benthos. This ten string detector with 302 OMs in total is referred to as AMANDA-B10.

After the completion of AMANDA-B10 the construction of the next stage, AMANDA-II, began in the 1997-98 season with the addition of three strings, each with 42 OMs located between 1200 and 2350 metres. A further six strings with 48 OMs per string were deployed in 1999-2000 on a circle with a radius of 90 metres around AMANDA-B10. These nineteen strings carry a total of 677 OMs (see Fig. 3.3).

3.3 Data Acquisition

The OMs are operated at a high gain of 10^9 so that the pulses generated in the PMTs can be transmitted to the surface through two kilometres of cable. This cable transport will both weaken and disperse the pulses so that a typical 1 V PMT pulse with a rise time of 3 ns and a full width half maximum (FWHM) value of 7 ns will arrive at the surface with an amplitude of 10 mV and a rise time of 60 (200) ns and a FWHM of 250 (600) ns for the twisted quad (coaxial) cables.

The data acquisition (DAQ) electronics for AMANDA is housed in the Martin A. Pomerantz (MAPO) building, named after the first Antarctic astronomer and located nearly a kilometre away from the South Pole Station almost directly above the array. The cables are connected to SWAMP (SWedish AMPlifier) circuits through which the 2 – 2.5 kV high voltage from the LeCroy 1440 and 1458 generators is routed and the PMT pulses are received and amplified. There are different outputs from the SWAMPs, one is delayed by 2 μs and then fed into peak sensing ADCs (Phillips 7164) and the others are sent into discriminators (Lecroy 4413). From the discriminators signals are sent both into a trigger unit, the Digital Multiplicity Adder (DMAD), as well as into TDCs (Lecroy 3377). The TDCs can store the leading and trailing edges of eight pulses, the two times when the pulse matches the discriminator threshold voltage, during a 32 μs time window with 1 ns resolution. The ADC on the other hand only records the maximum ADC value overall of the same eight pulses.

The main trigger condition is the multiplicity trigger. If a given number of channels register pulses that pass the discriminator threshold the event data is read out. Each discriminator channel sends a 2 μs pulse when a PMT pulse exceeds the threshold and these are added up to check if the trigger multiplicity is satisfied. When the trigger condition is met a veto is issued for the trigger unit, the ADC gate is opened for 4 μs (with the 2 μs delay that amounts to $\pm$ 2 μs around the trigger time) and 10 μs later a common stop is sent to the TDCs and the 32 μs buffer is read out. The multiplicity required has been chosen

so that the trigger rate is kept around 100 Hz, this is limited by the read out capacity of the system. In 1997 the trigger threshold was set to 16 channels, in 1998 although three more strings had been added it was lowered to 12 and in 1999 it was set to 18. The DAQ has been modified quite a bit over the three years covered in this work, from a purely CAMAC based system in 1997 read out with a MacIntosh PowerMac 7200 to a mainly VME-based one read out through a VME CPU running Lynx and which was connected to PCs running Linux for slow control and data storage in 1998 and 1999.

3.4 Timing and Geometry Calibration

After a photon hits the photomultiplier inside the OM down deep in the ice there are several 'delays' before the return pulse is registered up at the surface by the data acquisition system. There is the high voltage dependent cascading in the PMT (around 70 ns at normal AMANDA settings) as well as the almost two kilometre transport through the electrical cable ($\sim$ 8 μs) and the DAQ itself. These are collectively referred to as the electronic delay and it is this quantity that is sought after in the timing calibration.

The actual cable transport time measurements are done with a fast diode pumped YAG laser located at the surface sending pulses down optical fibres to diffusing nylon spheres located some tens of centimetres (or 9.5 metres in some cases) from the OM in question. The response of the OMs is read out using the main DAQ, which in the 1997-98 season unfortunately could only read out data at a maximum rate of 100 Hz. Separate measurements were therefore also made by using a timing DAQ so that the system could be run at the kHz scale. In the 1998-99 season there was a new DAQ in place capable of reading out data at higher rates and all timing calibration was done with the main DAQ.

The photomultiplier pulse is not only delayed but it is also distorted during the propagation through roughly two kilometres of electrical cable. The arrival time of the pulse is determined by a discriminator threshold setting for the TDC and the pulse deformation induces a time walk for low amplitude signals which has to be taken into account. The correction for the pulse propagation in the cable was found by fitting the leading edge (LE) time versus the ADC value to get the LE time of an infinite pulse. This gives the two parameter correction [120]

$$\mathrm{LE}_{corrected} = \mathrm{LE}_{raw} - t_0 - \frac{\alpha}{\sqrt{\mathrm{ADC}}} \tag{3.5}$$

which takes care of the delay (by t_0) as well as the deformation of the pulse (by the α term). More details on the timing calibration procedure for the 1997 and 1998 data is given in appendix A.

A very related issue is the geometry calibration, the determination of the relative positions of the OMs in the ice as well as the absolute position of the reference coordinate system. This is done with using the YAG laser to send light from the diffuser balls on one string and detecting the photons with OMs on another and fitting the relative distances of emitter and receivers [121]. This process is repeated for all combinations needed to map the whole detector array. The absolute position of the array could be ascertained by using two sets of data. During the drilling of the holes for the deployment of the strings the position of the drillhead was logged continuously. Secondly, depth sensors were deployed with the strings and read out during the descent and during the freeze in.

Chapter 4

Event Simulation

The event simulation is performed in three separate steps. The different event generation programs create samples of muons that are propagated to the vicinity of the detector with separate muon propagation software. The detector response to the light emitted by the passage of these muons is then simulated and a set of events that trigger AMANDA is produced. For consistency a single version of each of the programs needed for the three steps have been used in the simulation.

4.1 Generators

There are different generators for the various signals and backgrounds that are interesting with respect to AMANDA. The overwhelmingly dominating background is the atmospheric muons created in air showers caused by cosmic rays interacting in the atmosphere above the detector. The upgoing events are dominated by muons induced by atmospheric neutrinos originating in cosmic ray showers on the other side of the Earth. The signal that is sought among these two backgrounds in this work is that of upgoing muons induced by neutrinos which are byproducts of neutralino annihilations at the centre of the Earth.

4.1.1 Atmospheric Muons

The air showers in which the atmospheric muons are generated have been simulated with CORSIKA [122,123] (version 6.020). To be precise a specialised AMANDA version of this code (as described in [12]) have been used, which is better suited for the large cylindrical detector volume. The AMANDA version also includes the atmospheric profile and magnetic field for the South Pole.

The input is a cosmic ray spectrum with spectral index $\gamma = 2.7$ and the measured allparticle composition as described in [124]. For the high energy hadronic

interaction the QGSJET model have been used. The output from CORSIKA can be any of a number of particles including muons and neutrinos which are the only two that can reach the depth of the AMANDA detector. However, the rate of muons are several orders of magnitude larger than that of atmospheric neutrinos that interact to produce muons which can trigger the detector so the latter are ignored and the output only contains atmospheric muons. The primaries are simulated with energies between 600 GeV and 10^{11} GeV with a low energy cutoff for the primaries that is proportional to the atomic weight. In the simulation a curved surface for the Earth is used and the muons are generated on a surface just below the ground level (at 35 metres depth in order to compensate for the firn layer on top of the ice). The muons are only kept if they are estimated to reach a cylinder volume of 800 metres height and 400 metres radius around the detector. Every muon event have been oversampled 10 times through random redistribution at this surface level. In this work a total of 5.84×10^{12} showers have been generated, corresponding to a livetime of 276.1 days. This livetime is divided over the three years as 30.2 days for 1997, 63.1 days for 1998 and 182.8 days for 1999.

4.1.2 Atmospheric Neutrinos

The atmospheric neutrino generation is performed with NUSIM, a program based on neutrino interaction Monte Carlo simulation code described in [125]. As a starting point for NUSIM neutrinos with an E^{-1} energy spectrum are spread out randomly within a given solid angle on the surface at the other side of the Earth. As a means of speeding up the simulation NUSIM biases the muon generation by forcing every neutrino to interact near the the detector. The events are assigned a weight based on the probability of their occurrence such that the sum of weights gives the number of muons.

The atmospheric neutrino flux used is that of Lipari [126] and the preliminary reference Earth model [127] is implemented as the density profile for the propagation of the neutrinos through the Earth. The propagation itself is performed through a recursive algorithm which samples probability distributions to decide if the neutrino at the next interaction point suffers absorption through a charged current interaction or energy loss through a neutral current interaction and how far it has travelled before interacting. Neutrinos and anti-neutrinos are treated separately using the corresponding cross sections. The neutrino-nucleon interaction cross sections are calculated using the MRS G [128] parton distributions.

The simulated muon events induced by atmospheric neutrinos are generated in a cylindrical volume with a height of 500 metres and a radius of 100 metres and a centre that coincides with the detector centre at a depth of 1730 metres.

For neutrino interactions where the muon is estimated to reach this volume the energy and direction of the hadronic shower is also calculated and saved in the output along with the muon. The hadronic shower is particularly important for the events with low energy muons as the extra light from the shower can assist an event in passing the trigger multiplicity threshold where the light from the muon alone would not have sufficed. Low energy muons are central in the analysis of low neutralino mass scenarios. The muons are created with energies in the range from 10 GeV to 10^8 GeV and for zenith angles between 80° and 180°. A total of 1.2×10^8 atmospheric neutrino events have been simulated in this work, 2×10^7 for each year of data and for two different ice models.

4.1.3 Neutralinos at the centre of the Earth

The high energy muon neutrinos created through neutralino annihilations at the centre of the Earth is generated with the WIMPSIMP code [131]. For the use of the neutralino as the WIMP dark matter candidate the minimal extension to supersymmetric standard model (MSSM) detailed in [130] is applied. Within the MSSM the neutralino is the lightest linear combination of the neutral gauginos $\widetilde{B}$, $\widetilde{W}_3$ and the neutral Higgsinos $\widetilde{H}_1^0$, $\widetilde{H}_2^0$. In the calculation of the neutralino capture rates the local dark matter density is assumed to be 0.3 GeV/cm^3. The input in the WIMPSIMP code is tables with 1.25×10^6 events produced through Monte Carlo simulations of the annihilation process with an approximate treatment of the hadronisation [129].

Six neutralino masses is used for the generation of the signal samples: $M_\chi =$ 100, 250, 500, 1000, 3000 and 5000 GeV/c^2. The annihilation channels chosen for the signal samples follows earlier work [104,129] and they are extreme cases of the neutrino energy spectrum. The W^+W^--channel is used for the hard annihilation spectrum and the $b\bar{b}$-channel for the soft spectrum.

The program GENNIUP is used for the propagation of the neutrinos to a generation volume around the detector and for creating the muon and the accompanying hadronic shower at the interaction point. The GENNIUP code uses PYTHIA [132] (version 6.215) for the detailed simulation of the neutrino-nucleon interaction. The average momentum direction and the total energy of all the other particles created in the hadronic shower, besides the muon, is calculated for use in the detector simulation which models the light output of the hadronic shower. There is a cutoff for neutrino energies below 15 GeV at the interaction and an imposed muon energy threshold of 10 GeV. The active volumes used for the different neutralino masses as well as the number of muon events generated for the signal samples that are used in the calculation of the final results of the analysis is presented in Table 4.1.

	Generation volume			Number of generated muons	
M_χ (GeV/c^2)	Height (m)	Radius (m)	Depth (m)	Hard channel	Soft channel
100	950	190	1730	880258	688876
250	1550	230	1905	955668	834771
500	2350	270	2305	978139	902521
1000	3500	290	2780	989277	941528
3000	6150	320	4105	996550	973259
5000	7600	410	4830	998141	980633

Table 4.1: The height, radius and depth of the centre of the cylindrical generation volumes used with GENNIUP for the neutralino signal events as a function of neutralino mass. The number of muon events generated for the hard and soft annihilation channels in the samples used for the final results of the analysis is also given.

All the neutrinos are forced to interact and in order to compensate for the variation of the neutrino-nucleon cross section with energy the input neutrino spectrum is weighted with the neutrino energy to recover the original spectrum.

4.2 Muon Propagation

The muon propagation of the generated events is performed with the MMC (Muon Monte Carlo) program [12,110]. The active volume is defined as the region where light from the muon can be detected by AMANDA. In this volume the muon propagation is treated with considerable detail as the light created by the energy loss processes is needed as input to the detector simulation. In the implementation of MMC for AMANDA the ice is divided into three regions. For computational reasons the first region which considers the propagation of the muon from the point of creation, or in the case of atmospheric muons the generation surface, to the active volume treat the energy loss processes in a simplified way. The second region considers the propagation through the active volume around the detector, this volume is chosen as a cylinder with a height of 800 metres and a radius of 400 metres. In the third region, propagation after leaving the active volume, the average muon range given the muon energy at the exit point of the active volume is calculated and used for estimation of the end point of the muon track.

There is also the possibility to use two different media during the muon propagation with MMC, for AMANDA the option is available to insert the rock surface below the detector. In future neutralino simulations this can be utilised when two different media is used in the generation of the muon through the neutrino-nucleon interaction.

4.3 Detector Response

The detector response to cascades and muons that propagate through or in the vicinity of the array is simulated with the program AMASIM [133]. The muon energy loss processes are simulated with the muon propagation software and the deposited light is propagated through the ice to the optical modules by the photon simulation. The simulation then models the PMT response to this light, the cable transport of the PMT signals and how these finally are processed by the DAQ electronics.

Instead of tracking individual photons AMASIM uses lookup tables storing the mean amplitude and arrival time distribution of photons from sources as a function of location. The photon tables are generated with PTD (the methodology of the PTD code is described in [134]) where the input parameters from the detector Monte Carlo are the distance to the light source and the relative orientation of the light source to the OM. The output is the arrival time and the number of photoelectrons seen by an AMANDA OM, factoring in the glass, gel, hole ice, OM curvature, cathode sensitivity and the light distribution (applying only a relative sensitivity in the detector simulation). The depth dependence of the ice properties (illustrated in Fig. 3.2) cannot be taken into account directly in the tables created with PTD. Instead they are implemented by using several tables with different ice properties. A number of vertical layers are defined through the detector and a specific set of values for the scattering and absorption are chosen for each layer. A table created for these values is then used for all the OMs that reside inside a layer.

The MAM layered ice model is used for the signal and background simulations in this work. As an estimation of systematic uncertainties due to the ice properties used in the detector simulation the KGM ice model is used for comparison. The difference between the two models is that the MAM model has longer absorption lengths resulting in a better agreement between data and atmospheric muon simulations.

The disadvantages of the PTD layered approach (where each OM resides in homogeneous ice where the ice properties are averaged) have lead to the development of Photonics [135,136]. This program propagates photons through ice with varying properties along the path. The layers in the ice as well as other dependencies, e.g. wavelength dependence of scattering and absorption, can be properly taken into account. However, although a full detector simulation that utilises Photonics for the photon propagation is under development it has not reached a stage where it could be used in this work.

For the simulated response of the photomultiplier tube a single photoelectron pulse measured in the laboratory is used with the number of photoelectrons ob-

tained from the photon table to derive a pulse amplitude. The arrival time of each photoelectron is smeared with a time-jitter in the form of a Gaussian with a width of 7 ns.

As AMANDA is a test-bed for technology and was constructed over several years there are several different combinations of optical modules, cables and amplifiers at the surface that each produce characteristic pulse shapes as seen in the SWAMP output. These pulse shapes have been digitised and are used to simulate the SWAMP output pulse. The time at the surface is given by the smeared arrival time plus the experimentally obtained t_0:s for the cable transport. The amplitude is scaled and if there are several pulses they are superimposed. The threshold condition can then be applied for each channel to obtain the leading and trailing edge that would be measured by a TDC and the 2 μs pulse that is used for building the trigger.

Dark noise have been included in the simulation. The noise rate of each channel have been estimated from data and the noise hits are randomly distributed accordingly within the time window of each channel (a window larger than the 32 μs TDC window). The simulated discriminator pulses are checked to see if the multiplicity trigger (or any other trigger) requirement is fulfilled in which case the event is saved.

Chapter 5

Event Reconstruction

The events that trigger AMANDA can be reconstructed in several ways based on the recorded pulse information and the different algorithms are collected in the software package RECOOS [137]. Since the overwhelming majority of muon events in AMANDA are downgoing atmospheric muons an initial classification that is quick and simple is required to reduce the recorded data to more manageable quantities of interesting events. The classification needs to have a good rejection capability of downgoing events and at the same time a good efficiency for upgoing events. For the selected events more elaborate reconstruction methods can be utilised, in particular the main muon track reconstruction is a maximum likelihood optimisation using the PMT pulse arrival times, widths and amplitudes for the detected photons. For cascades a hypotheses of spherical propagation is used instead of the Cherenkov one used for track reconstructions.

5.1 Reconstruction Methods

5.1.1 First Guess Algorithms

Line fit

The line fit (LF) is an analytical solution and therefore relatively quick to calculate. It uses the time and position of the hit OMs together with the assumption that the photons are traversing the detector with velocity $\bar{v}$ along a straight line. This hypothesis can be expressed through the relation $\bar{r}_{OM} = \bar{r}_0 + \bar{v}t_{OM}$ where $\bar{r}_{OM}$ is the position of the OM and t_{OM} is the time of the hit. Summed over all the hits one constructs

$$\sum_{i=1}^{N_{hit}} (\bar{r}_i - \bar{r}_0 - \bar{v}t_i)^2 \tag{5.1}$$

and minimising this χ^2-like function gives the vertex and velocity

$$\bar{r}_0 = \langle \bar{r}_i \rangle + \bar{v}\langle t_i \rangle \tag{5.2}$$

$$\bar{v} = \frac{\langle \bar{r}_i t_i \rangle - \langle \bar{r}_i \rangle \langle t_i \rangle}{\langle t_i^2 \rangle - \langle t_i \rangle^2}. \tag{5.3}$$

The direction of the velocity vector $\bar{v}$ can be used to determine if the event is up- or downgoing with the zenith angle defined as $\theta_{LF} = -\arccos(v_z/|\bar{v}|)$. The speed of the line fit, $v_{LF} = |\bar{v}|$, is also useful for another kind of event classification as elongated muon events have large values unlike cascade-like events which have low values.

Tensor of inertia fit

With the tensor of inertia fit (TIF) the hits are seen as virtual mass points and analogous to the tensor of inertia in mechanics this object can be calculated and the eigenvalues I_i of its three axes can be used for classification of events. With I_1 being the smallest eigenvalue the sphericity of an event can be defined as $3I_1/(I_1 + I_2 + I_3)$. The sphericity is close to one for contained cascade-like events since the three eigenvalues are similar but for long tracks I_1 is much smaller than the other two. Another related and useful concept that is calculated as a part of TIF is the centre of gravity (COG) of the hits, $\bar{r}_{COG} = \langle \bar{r}_i \rangle$.

Direct walk fit

In the direct walk (DW) fit the hits are paired and examined if they are to be considered as track elements. I.e. if the time difference between hits in OMs separated by more than 50 metres is such that the hits are plausible as unscattered photons arriving from a passing muon. The criterion is $|\delta t| < d_{OM}/c + t_{win}$, where $d_{OM} > 50$ m is the distance between the OMs and t_{win} is a time window which starts out at 30 ns but if the number of track elements found in the event is too large (> 200) it is shortened by 5 ns and the track elements are re-examined. The direction of the track element is defined by the line connecting the two OMs and its position as the halfway point between the two OMs.

The track elements are then checked against all other hits to search for associated hits, hits that agree with the Cherenkov hypothesis including scattering delays. The associated hits of a track element must satisfy two relations: $t_{res} \in \{-30, 300\}$ ns, where $t_{res} = t_{hit} - t_{dir}$ is the residual time of the hit obtained by subtracting the time a Cherenkov photon would have arrived when travelling directly from the track element to the hit OM without scattering, and

$d_{hit} < 25\sqrt[4]{t_{res} + 30}$, where d_{hit} is the distance from the track element to the hit OM.

A track element is considered to be a track candidate if the number of associated hits, N_a, is ten or greater and if $\sigma_L > 20$ m, where $\sigma_L^2 = N_a^{-1} \sum_i (L_i - \langle L \rangle)^2$ and L_i is the projected length of the hit along the track element, measuring from the center.

If there is more than one candidate that fulfil the quality criterion

$$Q_{cand} \geq 0.7 \cdot Q_{max}$$

where

$$Q_{cand} = \min(N_a, 0.3 \cdot \sigma_L + 7)$$

and Q_{max} is the maximum Q_{cand} value, then a search for clusters is done. The number of candidates within a 15° cone around each track candidate is counted and the direct walk track fit is selected as the candidate with the largest number of candidates inside the cone. The direct walk track direction is computed as the average of the candidates within the selected cone.

Plane wave fit

The plane wave fit is similar to the line fit but more suited for cascade events as it instead assumes that the light is propagating through the detector as a plane wave. With $\bar{n}$ as the surface normal vector the function to be minimised is

$$\sum_{i=1}^{N_{hit}} (\bar{r}_i \bar{n} + v(t_i - t_0))^2. \tag{5.4}$$

5.1.2 Maximum Likelihood Algorithms

The first guess algorithms are not only used to reduce the data set but also serve as seed solutions to the main reconstruction algorithms which are based on maximisation of a likelihood function. The likelihood function is the product of the individual likelihoods for detection of the photons from the hypothesised track solution $\bar{h}$. The likelihood for an event $\bar{e}$ given a hypothesis $\bar{h}_j$ can be written as

$$\mathcal{L}(\bar{e}|\bar{h}_j) = \prod_{n=1}^{N_{hit}} \mathcal{L}(e_i|\bar{h}_j) \tag{5.5}$$

where e_i represents the measured parameters for the ith channel with a hit. The individual likelihoods $\mathcal{L}(e_i|\bar{h}_j)$ are estimated through simulations of photon propagation in ice, the reconstructions in this analysis use timing likelihoods

constructed from probability density functions (pdfs) for photon arrival times at the PMTs. The muon reconstruction assumes that the track is that of a single, minimum ionising muon with an infinite range. The pdfs used are analytical approximations to the distributions produced when simulating the scattering and absorption of photons in ice. They also modified to include the effects of PMT jitter and dark noise.

The Cherenkov photons are emitted at a fixed angle θ_c with respect to the track and as the PMT sensitivities are angular dependent the pdfs are dependent on the orientation of the PMT relative to the muon direction as well as the distance. A pdf that only includes the effect of scattering and absorption for an isotropic diffusion of light in a medium with refractive index n has been parametrised with a Gamma distribution [138]

$$p(t_{res}, d) = \frac{\tau^{-(d/\lambda_s)} t_{res}^{(d/\lambda_s - 1)}}{\Gamma(d/\lambda_s)} \cdot e^{-(t_{res}/\tau + ct_{res}/n\lambda_a + d/\lambda_a)} \tag{5.6}$$

and is here referred to as the Pandel function where τ is the scattering time, λ_s the scattering length and λ_a the absorption length. This function has been fit to Monte Carlo simulations of photon propagation for both muon tracks and cascades (an example of the parameters for muon tracks can be found in [137]). To include the effect of PMT jitter this function is convoluted with a Gaussian $G(t_{res})$ of width σ_{jitter} to form the patched Pandel (or upandel) function $\tilde{p}$. The implementation used in the reconstruction is

$$\tilde{p}(t_{res}, d) = \begin{cases} G(t_{res}) & \text{for} \quad t_{res} \leq 0 \\ P(t_{res}) & \text{for} \quad 0 < t_{res} < \sqrt{2\pi}\sigma_{jitter} \\ p(t_{res}, d) & \text{for} \quad t_{res} \geq \sqrt{2\pi}\sigma_{jitter} \end{cases} \tag{5.7}$$

where $P(t_{res})$ is a third order polynomial and $\tilde{p}$ is everywhere continuous and differentiable. The patched Pandel function is only an approximation used since it is easily calculable and a numerical convolution is too time consuming. However, an analytical convolution has recently been found and this exact solution can be used in future analyses. Finally, noise is included by adding a constant probability to the result of Eq. (5.7).

The single muon track hypothesis has five parameters, a vertex $\bar{r}_0$ and a direction given by two angles θ and ϕ. The likelihood

$$\mathcal{L}(\bar{t}_{res}, \bar{d}_{OM} | \bar{r}_0, \theta, \phi) = \prod_{n=1}^{N_{hit}} \tilde{p}(t_{res,n}, d_{OM,n} | \bar{r}_0, \theta, \phi) \tag{5.8}$$

can be used to search for the track parameters that give the maximum value for the time residuals of the hits $t_{res,n}$ and the OM positions $d_{OM,n}$.

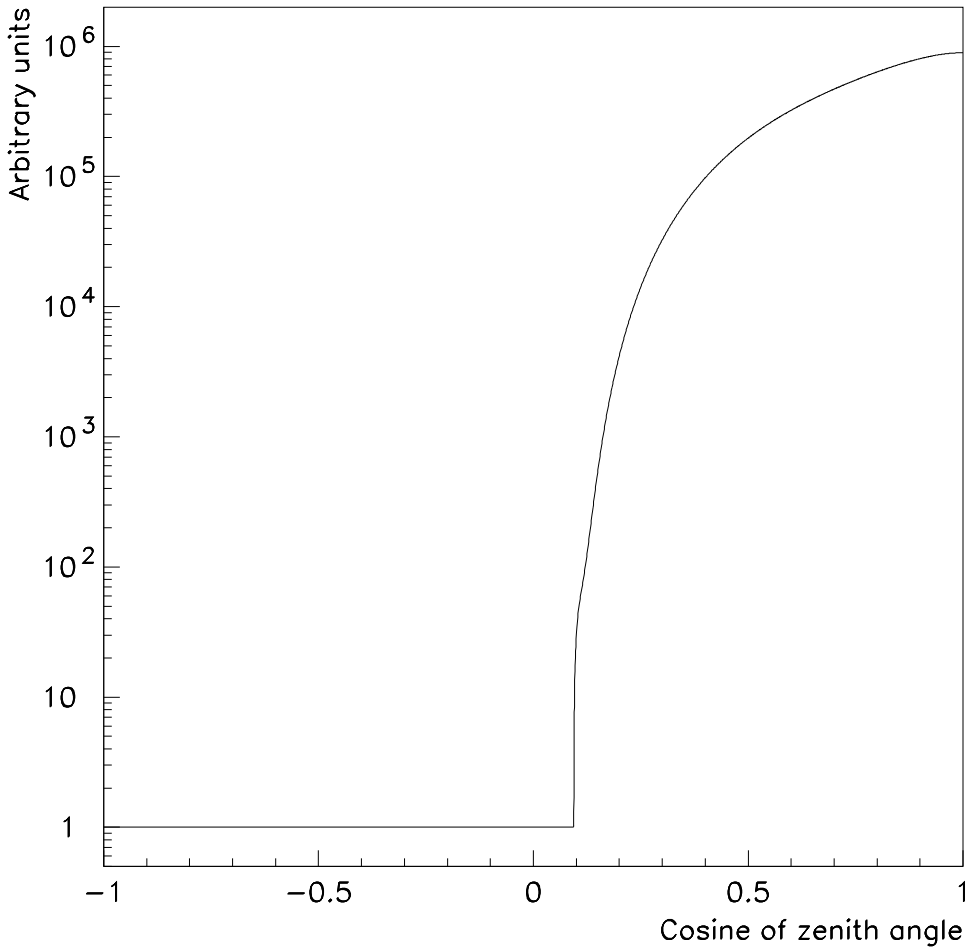

Figure 5.1: The function used for the prior in the Bayesian muon track reconstruction. For downgoing muons it is a parametrisation of the angular distribution of triggered events in simulations of atmospheric muons while it is flat for upgoing muons and downgoing muons just above the horizon.

Maximising Eq. (5.8) yields the track solution for which the observed data has the highest likelihood. But it does not consider the likelihood of the track itself. The probability of a hypotheses A given B can be calculated from the probability of A, B and that of B given A through Bayes' theorem which states that $P(A|B) = P(B|A)P(A)/P(B)$. Applied to our scenario this can be written as

$$P(\bar{r}_0, \theta, \phi | \bar{t}_{res}, \bar{d}_{OM}) = \frac{\mathcal{L}(\bar{t}_{res}, \bar{d}_{OM} | \bar{r}_0, \theta, \phi) P(\bar{r}_0, \theta, \phi)}{P(\bar{t}_{res}, \bar{d}_{OM})} \tag{5.9}$$

where the denominator $P(\bar{t}_{res}, \bar{d}_{OM})$, a constant which is the probability of an observation, can be ignored during the optimisation. The probability of a track, $P(\bar{r}_0, \theta, \phi)$, is the *Bayesian prior* and here it corresponds to the muon flux at the detector. The flux deep underground has been measured by other experiments and is characterised by its zenith angle dependence, therefore a one-dimensional parametrisation (see Fig. 5.1) based on Monte Carlo simulations of atmospheric muons is used as the prior function in Eq. (5.9) for the Bayesian track reconstruction. With this prior multiplied to Eq. (5.8) the track solution that maximises Eq. (5.9) is the most probable track given the observed data.

Although this is a muon analysis a cascade reconstruction is also used as a secondary hypothesis for each event and it is then tested against the single muon track reconstruction. The methodology of the cascade reconstructions is very similar to that of muon tracks. The difference lies in the coordinate system used to describe the cascade and in a separate parametrisation of the Pandel function in the photon arrival time pdf. The cascade pdf is based on Monte Carlo simulations of spherical light propagation from a point with a higher intensity in the forward direction.

For the cascade reconstruction a further improvement of the likelihood can be made, the standard Pandel pdfs are based on an assumption that all hits are single photoelectrons but for multi-photoelectron (mpe) hits where only the time of the first photoelectron out of N is considered, the pdf will be different (since on average a single photon scatters more than the first of N photons). The pdf for N photoelectrons is [5]

$$p_{mpe}(N, t_{res}, d) = Np(t_{res}, d) \left(\int_{t_{res}}^{\infty} dt p(t, d) \right)^{N-1} \tag{5.10}$$

and for the mpe cascade reconstruction this pdf is used in the likelihood calculation (Eq. (5.8) with the cascade parametrisation of the upandel function). In this analysis the mpe correction is only used for the cascade reconstructions although it is possible to do the same for the track reconstructions. The effect of using

the mpe pdf is more significant for cascade events than for low energy minimum ionising muons.

Chapter 6

Data Selection

The AMANDA data for 1997, 1998 and 1999 was taken during the Austral winter season between the middle of February through to the beginning of November. The summer months were dedicated to deployment of new strings, revamping of the electronics, calibration and general maintenance work.

The maximum likelihood algorithms require a few tenths of a CPU-second per event and as there are on the order of 10^9 events in the data set of each year this means that a full reconstruction of every event would be very time consuming. The need to reduce the amount of data events that are to be reconstructed meant that the very fast line fit first guess were used together with a zenith angle cut as a first step. The events that passed this filter were then reconstructed with a maximum likelihood algorithm. After this reconstruction and subsequent cuts the data is reduced by about a factor of a hundred. The two steps in this procedure is called the level one and the level two filtering. The level two filtering of 1997, 1998 and 1999 data have been done on machines at NERSC in Lawrence Berkeley National Laboratory, California, USA.

The hits recorded in AMANDA data do not all come from light emitted by cascades or muons passing through the detector array. There are hits induced by dark noise in the PMTs, by radioactive potassium in the glass used to house the PMTs and there is also PMT pre- and afterpulsing. Noise in the DAQ electronics at the surface and cross talk between channels, either created in the strings or in the electronics, can also contribute hits to the events. These hits are not desired and several criteria have been developed that the hits must fulfill if they are to be used in the reconstruction. This selection procedure is referred to as hit cleaning. There are also some OMs that are malfunctioning or that have ceased to function and the removal of all hits from these OMs is also included in the hit cleaning.

Every year there are also some problematic runs, e.g. where large parts of the array failed due to problems in MAPO. The level two filtering loops over all

the events that have been collected for each year. During the filtering process for the 1997, 1998 and 1999 data a second objective was to gather statistics of the detector performance over the data taking periods. The statistics collected of the behaviour of each OM is e.g. dark noise rates, ADC and TDC rates for all channels, rates of the different triggers, the number of events in each file as well as the parameters of a exponential fit to the distribution of the time difference between events. The harvested information is then compiled per run and the summed statistics for each run was examined and bad runs identified.

The read out of the events in the data taking creates deadtime for the detector. From the time difference between events calculated during the filtering the true rate, r_{true}, can be estimated by doing an exponential fit to the distribution per data file. The deadtime corrected livetime of the detector can then be calculated as the sum over all the files in good runs of N/r_{true}, where N is the number of events in the file.

The reconstructions performed at filter level one and two is similar for all three years 1997-99 and the level one filtering with the line fit calculation and subsequent cut mainly differs in the cut value used, in the 1997 filtering it is 50° while for 1998 and 1999 data it is 70° (where 0° means straight downgoing and 180° is vertically upgoing). This fast filtering rejects around 80 – 90 % of the triggered events.

The data samples used in this work is the filter chain designed for upgoing muons where the maximum likelihood reconstruction performed is for a muon track. Other filter chains have been designed for different analyses like cascades, GRBs and high energy events. Different trigger requirements have also been filtered out separately.

The cuts applied at filter level two is firstly a demand that the zenith angle of the muon track reconstruction is greater than 80° and secondly that the muon track solution found used at least three hits which have time residuals in the interval from −10 ns to 25 ns. The time residual of a hit is calculated by subtracting the expected arrival time of an unscattered Cherenkov photon emitted by the track from the actual time of the hit. A more detailed accounting of the level two filtering, including the lists of which OMs were excluded from use in the reconstructions is presented in appendix B.

Using the data compiled on OM and detector performance during the offline filtering it is possible to identify channels that are occasionally not working properly and which should not be used for analysis in those particular runs. It is also possible to identify runs where the detector as a whole or at least large parts of it is not functioning. The runs that have been identified as bad in some form or another is skipped in further processing of the data. For all analysis the events in the good runs that have passed the cuts at filter level two are reconstructed

again. In the new reconstructions hits from OMs that have been listed as bad are excluded on a per run basis. More details on the level two filtering and the bad OM lists used there as well as the enlarged bad OM lists used for higher level analysis along with the bad run list for 1997, 1998 and 1999 data can be found in appendix B.

The deadtime corrected livetime of the good runs for the three years included in this work is 130.1 days in 1997, 183.6 days in 1998 and 222.6 in 1999. The total livetime of the detector is thus 536.3 days for the usable data in 1997-99.

Chapter 7

Data Analysis

7.1 Blindness

As a means of reducing the risk of biasing the analysis a blindness approach was implemented. Since the search is for neutrino induced muons from the direction of the centre of the Earth which is a fixed direction the best way to blind the analysis is by sampling the data. Therefore the cuts on filter levels three through five was optimised using a subset of the data sample and this subset was then excluded in the calculation of the final results.

The data analysis starts with the level two filtered upgoing track samples for 1997, 1998 and 1999 data which were described in the previous chapter. For the three years included in this analysis the subsample of the data used when establishing the cuts was around 20 percent for each year. The selection process came naturally from the name convention for the data files, each data file is tagged with year, day, run and file number within this run. The optimisation subset was chosen as all files where the file number ended with a 0 or a 5. Due to slight differences in the detector setup and DAQ software the relative size of this subset with respect to the total data set varies a little between the years. The relative size is 23.1 % for 1997, 20.5 % for 1998 and 20.9 % for 1999. The total deadtime corrected livetime for the cut optimisation samples is 114.42 days and for the remaining sample it is 421.92 days.

For each analysis the signal efficiency is estimated from a second sample of the simulated signal, independent from the sample used for optimising the cuts. In the same way the simulated atmospheric neutrino background samples for each year is divided in two, the first half is used for the cut optimisation on filter level six and the second half is used to calculate the expected number of events presented for each filter level.

7.2 Filter Level Three

7.2.1 Flare and Cross Talk Cleaning

The aim of the level three filter is to reduce the downgoing muon background as much as possible while retaining most if not all of the nearly vertically upgoing muons.

In the data there is a non-simulated background where the events are characterised by a large number of almost simultaneous hits on the six outer strings of the AMANDA-B10 array while having almost no hits on the inner four strings. The timing calibration of the events cause these to be reconstructed as upward going tracks and they therefore pass the level one and level two filters.

The first cut on level three is designed to remove these events from the data. Ideally this should have been done earlier in the filter chain but at the time when the filtering took place there was not a sufficient understanding of these events, they were noticed and studied later on at higher cut levels in various analyses. So they were not removed before level three in any of the three years of data considered in this analysis. These events, referred to as "flare events", seem to be induced in the DAQ electronics and the most likely suspect at the moment is the high voltage supplies.

This "flare"-cleaning is different for 1997 data with respect to 1998 and 1999 data. For the latter two years the number of TDC-edges is used but for 1997 this event information is not available in the higher level data format and instead the number of hit OMs on the outer versus the inner strings is used.

For 1998 and 1999 the following cleaning was used: A hit is considered as a potential flare hit if has 16 TDC-edges (the maximum possible with 8 TDCs and a sign of TDC overflow) and it resides on any of the twisted quad strings of the AMANDA-B10 array (strings 5-10). If all six strings 5-10 have more than 240 such hits then the event is classified as a "flare event" and removed.

In the 1997 data the event was rejected if there were more than a hundred OMs hit on all six strings 5-10 while less than five OMs had been hit on the inner four coaxial cable strings 1-4.

Another source for misreconstructions that is removed at level three is cross talk in the twisted quad cables on strings 5-10. PMT pulses with an amplitude above a certain threshold, which varies from channel to channel, induce short pulses in channels that are in close proximity inside the cable during the transport back to the DAQ on the surface. These hits are cleaned using the *xt-filt* program [139] and just like in the normal hit cleaning they are not removed from the data but simply not used during the subsequent reconstructions.

Two different approaches to the cross talk problem are used as these pulses can

			Number of events		
Year	Type	Livetime	L0	L2	L3
1997	N_{data}	30.05d	2.4×10^8	5.1×10^6	3.5×10^5
	$N_{atm.\nu}$	30.05d	1314.3	706.7	326.1
	$N_{atm.\mu}$	30.17d	2.0×10^8	4.4×10^6	2.7×10^5
1998	N_{data}	37.92d	5.5×10^8	2.6×10^6	1.9×10^5
	$N_{atm.\nu}$	37.92d	2431.7	418.7	207.5
	$N_{atm.\mu}$	63.07d	5.6×10^8	2.7×10^6	2.1×10^5
1999	N_{data}	46.45d	2.7×10^8	2.7×10^6	3.2×10^5
	$N_{atm.\nu}$	46.45d	818.0	471.9	328.7
	$N_{atm.\mu}$	73.13d	2.9×10^8	2.3×10^6	2.8×10^5

Table 7.1: The number of events at trigger level (L0) and that pass the level two (L2) and three filtering (L3) for the blind subsets of data, the atmospheric neutrino and atmospheric muon simulations. The livetime of the samples is given in units of days.

be identified either solely by their short duration and amplitude or by the looking at the time difference between high and low amplitude hits in channels known to cross talk to each other. The first is an extension of the hit cleaning done by requiring TOT $>$ 125 ns for all channels. For hybrid OMs (specially designed dual read out OMs for testing optical transmission of the PMT pulse) the electrical pulses are actually longer and the cleaning cut was raised to TOT $>$ 200 ns. A further improvement is that for each channel in strings 5-10 a function was fitted to the ADC versus TOT distribution of hits in the timing calibration data set (see section 3.4) [139]. The function is then used to exclude hits based on both their ADC and TOT values. In the second method the timing calibration data was examined to find emitter and receiver pairs for the cross talk and the probability of cross talk for these pairs was estimated [139]. This could only be used safely (i.e. maintaining a high efficiency for real hits) to clean hits for pairs with a substantial separation so it is used for pairs where OMs at the top of the array is cross talking to OMs in the bottom and vice versa.

7.2.2 Improved Reconstructions

The events that make it through the "flare"-filter are reconstructed again but on top of the cross talk identification the change from the level two hit cleaning is an improved list of bad OMs, where the OM selection is done per run. Better timing calibrations are also used for the data of each of the three years.

To provide consistency over the three years three new first guess reconstructions are performed: A tensor of inertia fit, a direct walk fit and a plane wave fit.

		Number of WIMP events					
		Hard annihilation channels			Soft annihilation channels		
Year	M_χ (GeV/c^2)	L0	L2	L3	L0	L2	L3
1997	100	41097	31148	21305	14463	10390	5738
	250	48123	36839	29236	16305	12295	8596
	500	41905	31591	25919	14348	10911	8242
	1000	43003	32056	26784	13879	10553	8507
	3000	44730	32510	27660	13790	10372	8638
	5000	31493	22430	19202	8971	6622	5545
1998	100	60071	20974	15771	22212	7132	4684
	250	65524	23216	19743	23742	8287	6317
	500	55611	19104	16741	20058	6997	5728
	1000	56366	19154	17002	18915	6668	5686
	3000	58049	19174	17265	18222	6266	5536
	5000	40118	12912	11636	11815	3956	3521
1999	100	18927	15799	14059	3350	2800	2459
	250	32484	26886	24713	8009	6691	5979
	500	30397	24755	22837	8711	7162	6555
	1000	32622	26258	24247	9548	7892	7293
	3000	35132	27582	25438	10344	8325	7687
	5000	25022	19261	17814	6861	5446	5006

Table 7.2: The number of events for the blind subsets of WIMP signal simulations at trigger level (L0) and passing the level two (L2) and three (L3) filtering.

The main muon fit is a Bayesian fit with the direct walk fit as first guess. As a secondary hypothesis for each event a cascade reconstruction is also performed, first a single photoelectron likelihood optimisation with the plane wave as starting solution and then the end result is used as input to a MPE cascade reconstruction.

The filtering on level three requires that the Bayesian fit gives an upgoing track and that it has at least three direct hits in the time residual interval from -10 ns to 25 ns. The number of events in the blind subsets that pass the level two and three filter is given in Table 7.1 for data and background simulations and in Table 7.2 for the WIMP signal simulations.

7.3 Filter Level Four

7.3.1 Multi-Layer Perceptrons

Artificial neural networks were originally motivated by the structure of the biological counterparts in the brain and consist of an interconnected network of "neuron-like" processors. Each neuron, or node, in the network takes a set of inputs, processes them and sends the output further on to other nodes. Each connection between nodes is assigned a weight coefficient that reflects the importance of the link.

Neural networks are used for a multitude of nonlinear classification and modeling problems and their strength lies in the fact that given enough nodes they can approximate virtually any function. There are many classes of neural networks and the one used in this analysis is the feed-forward multi-layer perceptron (MLP), specifically the implementation in the program MLPfit, version 1.40 [140].

The MLP consists of neurons ordered into layers and each neuron receives input from all neurons in the previous layer and the output is fed to each neuron in the subsequent layer. The first layer is called the input layer and the last the output layer. The intermediate layers are known as hidden layers.

The output y_i of a node in the hidden layer(s) is given as $y_i = f(\xi_i)$ where f is a transfer function and $\xi_i = \theta_i + \sum_j w_{ij} x_j$, where the sum is carried out over all the inputs from the previous layer and θ_i is the potential of the node (which is set to zero in this analysis). For the node(s) in the output layer $y_i = \xi_i$.

There are several different forms used for the transfer function but one of the most common and the one used here is the sigmoid function

$$f(\xi) = \frac{1}{1 + e^{-\xi}} \tag{7.1}$$

The parameters of a neural net are determined through a process called training, in which the net learns by example. There are different kinds of training but in the supervised training which is used for MLPs the desired output is known and the weights w_{ij} are adjusted so that the output estimated by the network is as close as possible to that of the training examples.

For a given network structure the training is a nonlinear minimisation problem for the error function that expresses the difference between the actual and desired result. There are a number of different forms of this function, here the sum of the squared differences is used

$$E = \sum_j \sum_p \left(y_{pj}^t - y_{pj}^o\right)^2 \tag{7.2}$$

where the index j is summed over all output nodes and p over all training examples.

The training starts with random initial values for the weights and continues iteratively. In each iteration, known as an epoch, the network weights are adjusted so that the error is reduced. During the training two samples are used, one is used for the actual weight optimisation and the second is used as a test sample where the error function is calculated and used to find the right number of training epochs.

The test sample is needed to guard against a problem known as overtraining. A desired property of a neural network is generalisation, i.e. that the input-output

relation given by the network is correct for examples that was not used in the training of the network. When the training is performed over too many iterations relative to the number of examples the network may memorise the given examples while not being able to generalise to examples not previously seen. Therefore the training sample needs to be large enough as well as a good representation of the complete set of possible examples.

The test sample is used to ensure that the training does not continue for too many iterations, the appropriate number of epochs is given by the minimum of the test sample error function. The error function value for the training sample continues to decrease throughout the training but the values for the test sample will start to increase after a while, signaling that the training is not improving the network performance anymore.

7.3.2 Selected Variables

The input variables for the neural network was chosen from a set of potentially suitable variables through the process of step-wise ranking and the combinations were systematically tested using a fixed network structure.

The zenith angle of the Bayesian muon fit (Fig. 7.1(a) and (b)) was chosen as the primary variable and then all combinations of two variables were tested yielding the difference in the number of direct hits in the time residual interval from -15 ns to 75 ns between the muon and cascade fit as the best partner (Fig. 7.1(c)).

These two were then the base pair in the testing of the best case with three variables. The process with higher number combinations continued until there was no more improvement in the neural net performance which occurred for the case of nine out of the original set of variables for $M_\chi = 250$ GeV/c^2 hard annihilation channel analysis for 1997 data, a tenth variable was later found which improved the network for some of the channels.

These ten inputs, the distributions are shown in Fig. 7.1 – 7.3 for the blind 1999 data set, were then used for the optimisation process of each of the 36 channels.

7.3.3 Network Optimisation

Given the ranking of the nine input variables in the case of $M_\chi = 250$ GeV/c^2 hard annihilation channel for the 1997 detector an individual re-optimisation was performed for each channel at the same time as the network configuration was optimised.

The networks chosen for this analysis have one hidden layer and for a given set of input variables the optimisation was done by testing every configuration

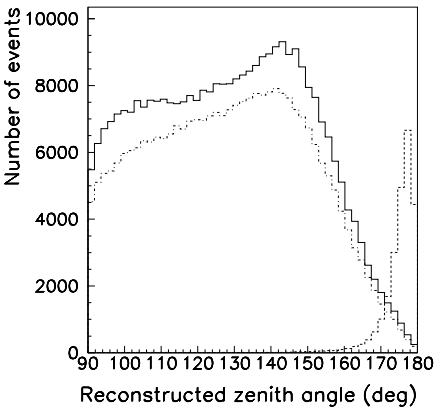

(a) Input 1, the reconstructed zenith angle of Bayesian muon reconstruction.

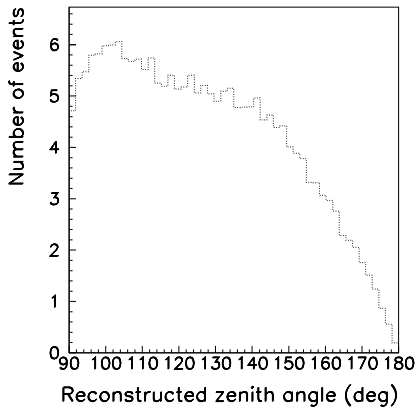

(b) Input 1, the reconstructed zenith angle of Bayesian muon reconstruction for the atmospheric neutrino simulation.

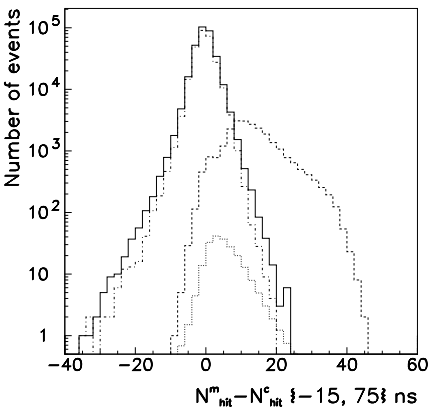

(c) Input 2, the difference between the Bayesian muon fit and the cascade fit in the number of hits with time residuals in the interval $\{-15, 75\}$ ns.

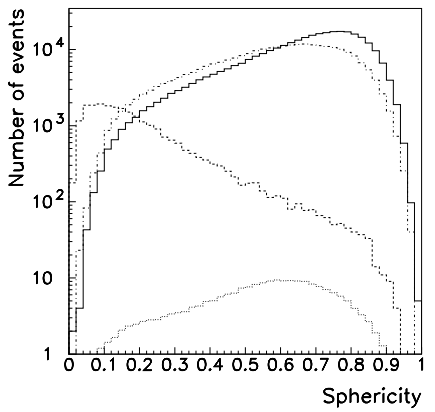

(d) Input 3, the sphericity or $3 \times I_1/(I_1 + I_2 + I_3)$ for the tensor of inertia fit.

Figure 7.1: Neural network variables shown for the 1999 analyses, data is drawn as a full line, 250 GeV/c^2 hard spectrum WIMP signal is dashed, upgoing atmospheric neutrino background is dotted and downgoing muon background is dash-dotted.

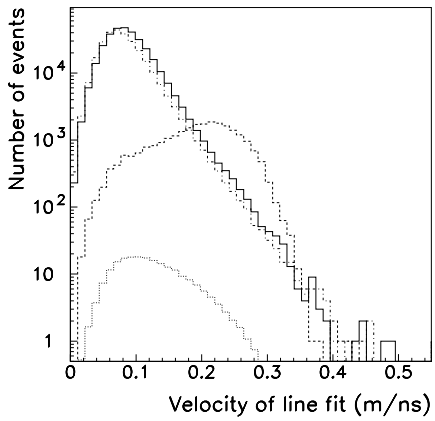

(a) Input 4, the velocity of the Line Fit.

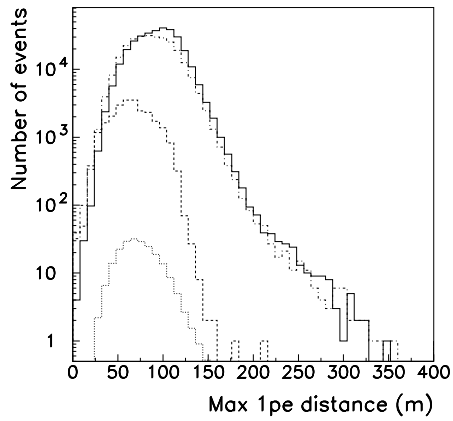

(b) Input 5, the largest distance of one photoelectron hits of the Bayesian muon fit.

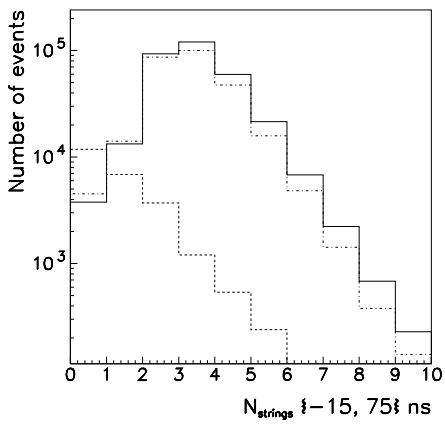

(c) Input 6, the number of strings with hits that have time residuals in the interval $\{-15, 75\}$ ns for the cascade fit.

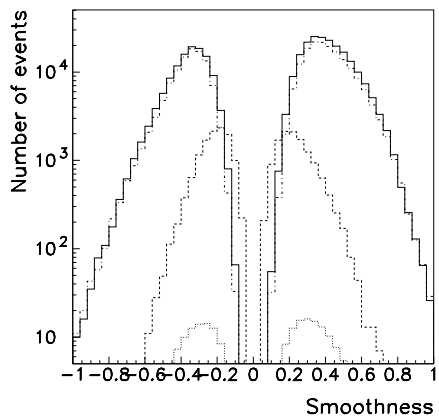

(d) Input 7, the smoothness of hits that has time residuals in the interval $\{-15, 75\}$ ns for the the Bayesian muon fit.

Figure 7.2: Neural network variables shown for the 1999 analyses, data is drawn as a full line, 250 GeV/c^2 hard spectrum WIMP signal is dashed, upgoing atmospheric neutrino background is dotted and downgoing muon background is dash-dotted.

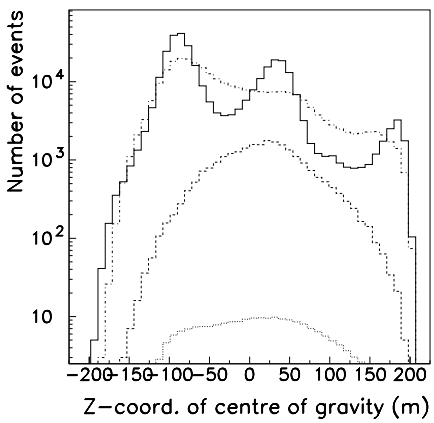

(a) Input 8, the z-coordinate of the "centre of gravity" for the hits in the event.

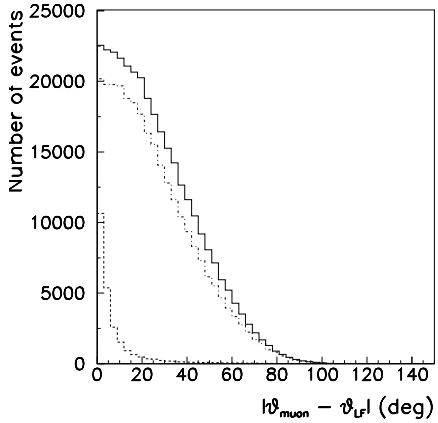

(b) Input 9, the absolute difference between the zenith angle of the Bayesian muon fit and the line fit.

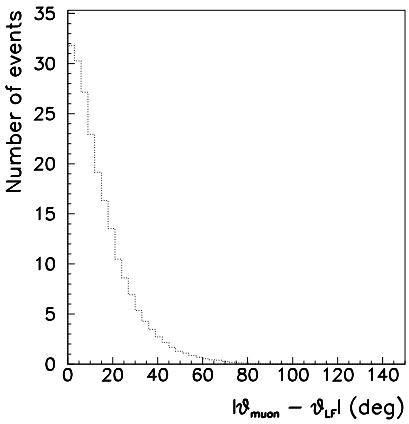

(c) Input 9, the absolute difference between the zenith angle of the Bayesian muon fit and the line fit for the atmospheric neutrino simulation.

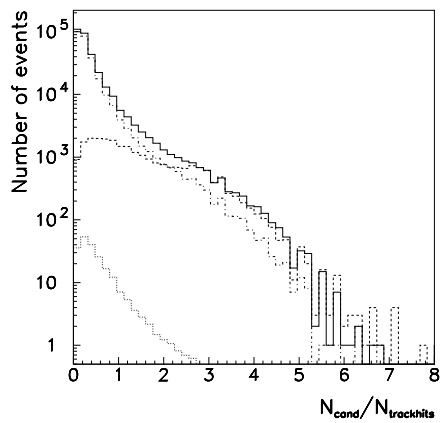

(d) Input 10, the number of track candidates divided by the number of track hits for the direct walk fit.

Figure 7.3: Neural network variables shown for the 1999 analyses, data is drawn as a full line, 250 GeV/c^2 hard spectrum WIMP signal is dashed, upgoing atmospheric neutrino background is dotted and downgoing muon background is dash-dotted.

		Hard annihilation channels		Soft annihilation channels	
Year	M_χ (GeV/c^2)	Network	Comment	Network	Comment
1997	100	9-13-1	standard nine	8-30-1	without input 6
	250	10-29-1	with input 10	9-34-1	standard nine
	500	10-33-1	with input 10	10-19-1	with input 10
	1000	10-25-1	with input 10	8-29-1	without input 4
	3000	10-20-1	with input 10	10-13-1	with input 10
	5000	10-35-1	with input 10	10-13-1	with input 10
1998	100	8-32-1	without input 4	9-19-1	standard nine
	250	10-20-1	with input 10	8-23-1	without input 7
	500	10-21-1	with input 10	8-21-1	without input 7
	1000	10-24-1	with input 10	9-17-1	standard nine
	3000	10-26-1	with input 10	10-21-1	with input 10
	5000	10-21-1	with input 10	10-16-1	with input 10
1999	100	8-23-1	without input 3	8-19-1	without input 3
	250	9-27-1	standard nine	8-29-1	without input 3
	500	10-15-1	with input 10	9-35-1	standard nine
	1000	10-11-1	with input 10	10-35-1	with input 10
	3000	10-26-1	with input 10	10-35-1	with input 10
	5000	10-22-1	with input 10	10-15-1	with input 10

Table 7.3: Neural network configurations for the 1997-99 analyses.

possible, limited only by the number of events available for the training through the criterion that the number of events divided by the number of weights in the neural net should not be below ten. For each channel the networks possible with nine input nodes was tested one by one, first 9-1-1, followed by 9-2-1 and so on up to 9-35-1. The input variables themselves were tested by adding inputs and testing all network structure combinations (10-1-1, 10-2-1, ...) as well as removing each of the nine variables and testing each of the possible networks with eight input nodes. For the cases where there was no improvement in going from eight to nine input variables for the network the range of networks with seven input variables was also tested, again by removing each variable and testing all the networks possible, but finally eight was the minimum number of inputs used in the analyses.

The neural networks were trained with a sample of about 2500 signal events and the same amount of data was used as background so that the total size of the learning sample was 5000 events. The test sample was of the same size and composed in the same manner. The data events were picked from runs 550-557 for 1997 and for 1998 and 1999 they were sampled over the whole year. A study was made to check if the result of the neural network was sensitive to the sampling by testing events from a single run, tens of runs and over the full year. There was not any noticeable difference between the latter two cases.

This process finally resulted in the 36 neural networks in Table 7.3 being chosen as the best ones for the different WIMP masses and annihilation channels.

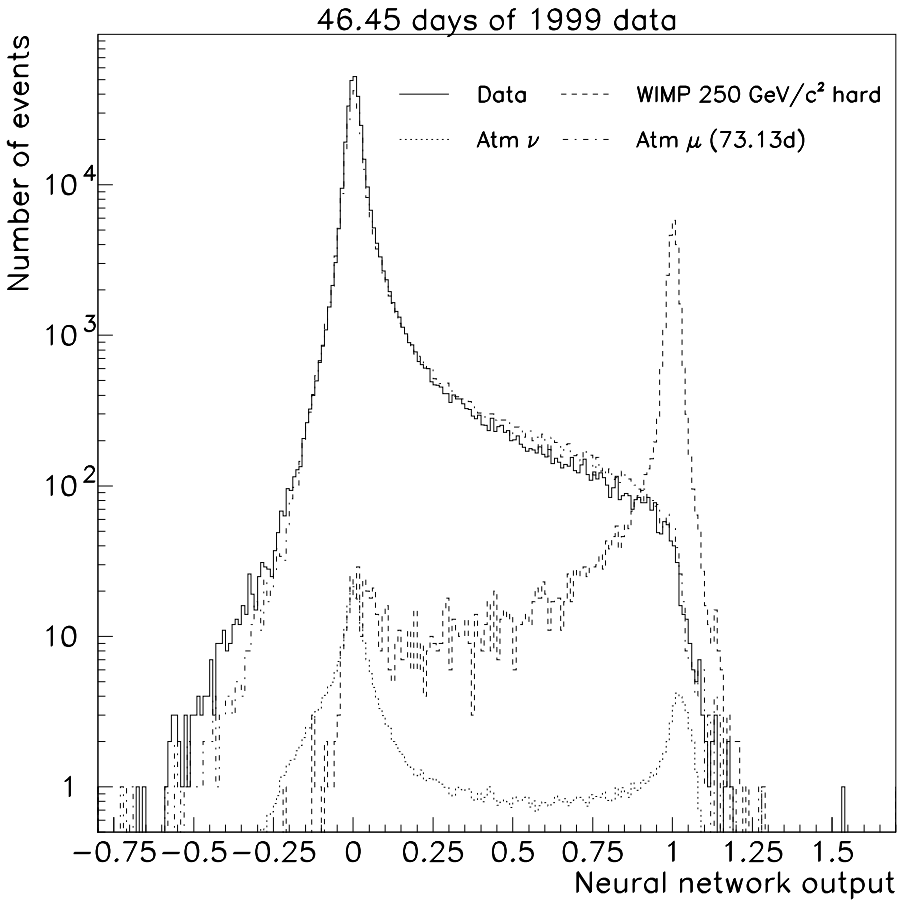

Figure 7.4: The output variable of the neural network for $M_\chi = 250$ GeV/c^2 hard annihilation channel WIMP signal trained with 1999 data. All events at filter level three for the blind subsets are shown. Data is drawn as a full line, WIMP signal is dashed, upgoing atmospheric neutrino background is dotted and downgoing muon background is dash-dotted.

Variable	Description
$v1$	Reduced likelihood for the Bayesian muon reconstruction
$v2$	Reduced likelihood for the cascade reconstruction
$v3$	Space angular difference direct walk fit - line fit
$v4$	Space angular difference muon fit - line fit
$v5$	Space angular difference muon fit - direct walk fit
$v6$	Direct walk measure, number of track candidates normalized to the number of track hits
$v7$	Smoothness of hits with time residual in the interval $\{-10, 15\}$ ns
$v8$	Smoothness of amplitude of the hits along muon track
$v9$	The ratio of late cascade fit hits to all hits (time residual > 75 ns)
$v10$	The ratio of late muon fit hits to all hits (time residual > 75 ns)
$v11$	Velocity of line fit
$v12$	Sphericity

Table 7.4: The variables used in the level five filtering.

The output variable of the neural network in the case of $M_\chi = 250$ GeV/c^2 hard annihilation channel WIMP signal trained with 1999 data is shown in Fig. 7.4.

The level four filtering is performed and optimised together with the level five post-neural network cuts which are presented in the next section. The result after cutting only on the neural network output variable for each of the analyses is shown in Table C.1 in appendix C. The number of signal events, N_{wimp}, is given for a second sample for each analysis, independent from the sample used for training the neural networks.

7.4 Filter Level Five

7.4.1 Quality Cuts

The muon reconstruction on level three is not perfect and most of the data events that pass the neural network cut are misreconstructed downgoing atmospheric muons that mimic signal.

Although the neural networks are very good at separating signal from background they are limited in a way by the quality of the input variables. However the events that pass the level four cut on the neural net output value have certain characteristics that are exploited on filter level five. The goal of this filter level is to remove these "fakes" so that what is left is a sample of upgoing muons induced by neutrinos.

Certain classes of events were easily removed by cutting on regions in the likelihood space of the two different reconstruction hypotheses, the muon fit versus the cascade fit, while others required tighter cuts on both new variables as well as variables already used in the neural networks together with with these likelihoods. The variables used for the level five filtering are listed in Tab. 7.4.

There remained a certain number of "fakes" that were caused by isolated hits that had not been cleaned away by the time isolation cut on level three since they consisted of pairs or triplets of hits. A new time isolation cut was implemented for level five to ignore these hits if they occurred more than 500 ns before or after the nucleus of hits in the event. The events were then reconstructed again with a new direct walk first guess and a new Bayesian muon fit using only hits that passed this added criterion. Finally, a zenith cut of 140° on the new muon reconstruction was also applied.

7.4.2 Cut Optimisation

The question of what value of the neural network output to cut on at level four was addressed through an optimisation against the quality cuts in the level five filtering. A hard neural net cut means that fewer "fakes" have to be removed by the quality cuts which therefore can be chosen to be softer. Vice versa, a loose level four cut means that there are more misreconstructed downgoing events to remove on the level five which is accomplished by using harder cuts (see plot of the neural network outputs for signal and background in Fig. 7.4).

The optimisation was done step-wise starting at 80 % signal efficiency for the WIMP signal from level three to level four (i.e. the neural network cut). Level five quality cuts were then found in order to remove the "fakes" that passed the neural network cut for 80 % signal efficiency. After this the level four cut was lowered which increased the amount of signal events that passed the network filter. But lowering the level four cut also meant more misreconstructed downgoing muons on level four and the quality cuts on level five were tightened to remove these and this process continued until the signal efficiency dropped irrecoverably (no possibility to achieve higher efficiency by reducing the neural network cut further). The combination of cuts on level four and five that gave the best signal efficiency was then selected. This could potentially lead to an over-optimisation so the final level five cuts were chosen as one set, chosen from the 36 individual sets, that worked for all channels.

After studying the events that passed loose cuts on level four for the various analyses it became clear that the same kind of events were classified by the different neural networks as almost signal-like although they were clearly not signal-like when inspected more closely.

The likelihoods of the muon and cascade fit were ranked lower as a neural network variable than the number of hits with time residuals in the interval from -15 ns to 75 ns and appeared to be somewhat correlated to it as the combination did not improve the network performance. Instead they became very useful as level five variables since the "fakes" that passed the level four cut often had better

Cut	Requirement
1	$v1 > 11$ AND $v2 > 12$ $(v1 - v2) > 2$ $v1 > 9.0$ AND $(v1 - v2) > 0.5$ $v1 > 8.5$ AND $(v1 - v2) > 1.5$
2	$v3 \geq 30$ $v4 \geq 30$ $v5 \geq 30$
3	$v1 > 9.0$ AND $v6 < 0.45$ $v1 > 8.5$ AND $v6 < 0.4$ $v1 > 8.0$ AND $v6 < 0.35$ $v1 > 8.5$ AND $(v1 - v2) > 1.0$ AND $v6 < 0.55$ $v1 > 8.5$ AND $(v1 - v2) > 0.5$ AND $v6 < 0.5$ $(v1 - v2) > 0$ AND $v6 < 0.45$ $v12 > 0.18$ AND $v6 < 0.55$
4	$v1 > 8.5$ AND $(v1 - v2) > 0.5$ AND $\mid v7 \mid > 0.45$ $v1 > 8.5$ AND $(v1 - v2) > 0.5$ AND $\mid v8 \mid > 0.45$
5	$v1 > 8$ AND $v9 > 0.41$ AND $v10 > 0.38$ $v1 > 9$ AND $(v1 - v2) > 0$ AND $v9 > 0.9$ $v2 < 8$ AND $\mid v7 \mid > 0.5$ AND $v9 > 0.75$ $v11 < 12$ AND $v9 > 0.49$ AND $v10 > 0.49$
6	$v11 < 0.05$ $v1 > 9.5$ AND $(v1 - v2) > 1$ AND $v11 < 0.12$ $v1 > 9$ AND $(v1 - v2) > 0.5$ AND $v11 < 0.11$ $v1 > 9$ AND $(v1 - v2) > 0$ AND $v11 < 0.1$ $v1 > 8.5$ AND $(v1 - v2) > 0.5$ AND $v11 < 0.08$ $v2 < 8.5$ AND $v11 < 0.08$ $v2 < 8$ AND $v11 < 0.09$ $v2 < 8$ AND $(v1 - v2) > 0$ AND $v11 < 0.1$ $v2 < 7.5$ AND $(v1 - v2) > 0.5$ AND $v11 < 0.14$ $v2 < 7$ AND $(v1 - v2) > 1$ AND $v11 < 0.18$ $v2 < 8.5$ AND $v3 \geq 30$ AND $v11 < 0.1$ $v2 < 8.5$ AND $(v1 - v2) > 0$ AND $v3 \geq 25$ $v2 < 8$ AND $v12 > 0.18$

Table 7.5: The level five cuts, the variable definitions are given in Table 7.4. An event was rejected if any of these criteria was satisfied. The AND indicates a logical AND, so that $v1 > 11$ AND $v2 > 12$ means that the event was rejected if both $v1 > 11$ and $v2 > 12$ were fulfilled.

cascade than muon likelihoods as well as being outliers in other distributions.

Most well reconstructed events have a fair agreement between the solution of the initial guess and the more sophisticated track reconstruction, therefore the space angular difference is a good measure to cut on. Three variations are used, both between the muon fit and the two muon track first guesses as well as between the two first guesses themselves.

One class of events that was targeted with the combination of variables v1, v2 and v6 (defined in Table 7.4) was downgoing muons or muon bundles that either stopped just outside the detector or passed by without entering the instrumented volume. Although the resulting light output gave rise to an upward reconstructed muon track, the cascade fit was usually a better solution and the direct walk first guess could not find many track candidates, resulting in a low v6-value.

Another measure of bad reconstruction quality was if there was a lot of late hits, with a time residual greater than 75 ns, indicating that the solution found did not take into account the topology of the event well enough.

A third category of misreconstructed events had a good cascade fit, not so good muon fit and low values of the velocity of the line fit.

There was also a class of "double" events in data, seemingly uncorrelated sets of hits at the top and bottom of the detector neither consistent with an upgoing hypotheses on their own but coincidently working together to give an upward going track solution. These were cut away by the likelihood of the muon track together with the smoothness along the track of the amplitude of the hits or of the hits with low time residuals.

The final set of "fake"-cleaning cuts at level five is presented in Table 7.5. This set was applied to all the individual analyses. The results for the blind subset after the level five filtering is presented in Table C.2 in appendix C.

7.5 Filter Level Six

7.5.1 Model Rejection Potential

The cuts up to and including level five were designed to remove the remaining background of misreconstructed downgoing atmospheric muons. Since there is no apparent excess of nearly vertical upgoing muons we need to be able to set the best limit on any potential WIMP signal and for this we use the method of model rejection potential [141].

In order to find an unbiased way to estimate the limiting cut of an analysis, i.e. without looking at the data sample, it is possible to use Monte Carlo simulations of the experiment to calculate what the average upper limit would be if the measurement was repeated a large number of times. The average upper limit,

or *sensitivity*, of the measured quantity with an expected number of background events N_{bkg} and no signal is the sum of each possible upper limit corresponding to the number of observed events N_{obs} weighted by the probability P of observing N_{obs} for the given background.

$$\bar{\mu}_{90}(N_{bkg}) = \sum_{N_{obs}=0}^{\infty} \mu_{90}(N_{obs}, N_{bkg}) P(N_{obs}, N_{bkg}) \tag{7.3}$$

The average upper limit can be used together with the signal expectation N_{sig} to form the model rejection factor (MRF)

$$\frac{\bar{\mu}_{90}(N_{bkg})}{N_{sig}} \tag{7.4}$$

which corresponds to the scaling factor used to set an average flux upper limit for a given signal flux. Therefore the best limit will on average be set for the lowest MRF and this fact is used for the optimisation of the limiting cut in this analysis.

The variable of choice is the zenith angle of the reconstructed muon track. The number of events above a given angular cut is summed up and for the atmospheric neutrino simulation the average upper limit is calculated. This is then divided with the number of expected signal events (which has been renormalized, but the actual number is not important only the shape of the distribution which is preserved) to get the MRF.

To calculate the 90 % confidence level upper limits the method of Feldman-Cousins (FC) [142] will be used and the probability for each upper limit is Poissonian so Eq. (7.3) becomes

$$\bar{\mu}_{90}^{FC}(N_{bkg}) = \sum_{N_{obs}=0}^{\infty} \mu_{90}^{FC}(N_{obs}, N_{bkg}) \frac{N_{bkg}^{N_{obs}}}{N_{bkg}!} e^{-N_{bkg}} \tag{7.5}$$

which is the sensitivity that will be used in the MRF.

Several optimisations are performed, the first three are for the individual limits for each year and the last is for the combined limit for all three years. The individual limits are optimised for the livetime of the remaining data samples when the blind sample is removed which is ~ 80 % of the total deadtime corrected livetime for each year (100.05 days in 1997, 145.68 days in 1998 and 176.18 days in 1999). For the combined limit the expected background is estimated for the sum of the individual livetimes, 421.92 days. Each year is optimised individually as if the total expected background came from that year.

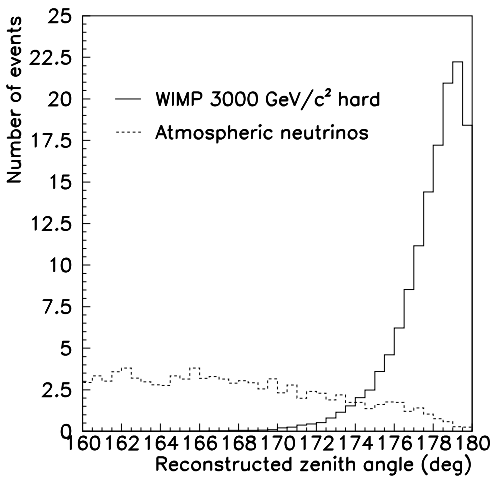

(a) The zenith distribution of the scaled WIMP signal and the atmospheric neutrinos corresponding to the deadtime corrected livetime of the data sample that is used for the final limit calculations.

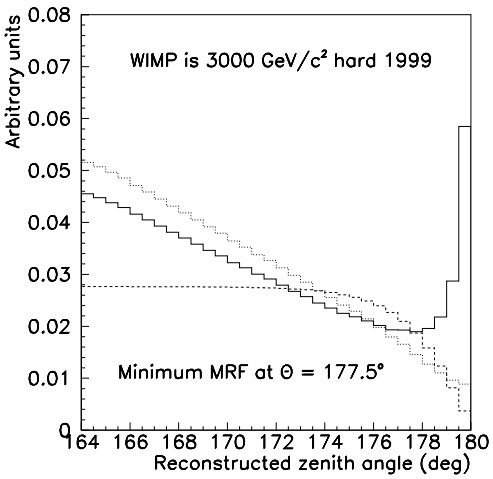

(b) The MRF for the distributions in (a), also shown is the curve for the integrated number of signal hits (dashed) and the average upper limit for the integrated atmospheric neutrino background (dotted).

Figure 7.5: An example of the model rejection potential method, from the analysis for the $M_\chi = 3000$ GeV/c^2 hard annihilation channel WIMP signal and 1999 data.

7.5.2 Zenith Cut

For each WIMP channel in the analysis the integrated number of events for the signal Monte Carlo sample as a function of the zenith angle is calculated as well as the average upper limit for the integrated number of events of the atmospheric neutrino background corresponding to the deadtime corrected livetime of the data sample that is used for the limit calculations. For the individual limits per year this is ~ 80 % of the original data sample livetime (since ~ 20 % was used for the cut optimisation) while for the combined limit this value is the total non-blind sample livetime. The minimum of the MRF is then found to obtain the optimum angle for the final zenith cut. An example is shown in Fig. 7.5 for the case of $M_\chi = 3000$ GeV/c^2 hard spectrum WIMP signal and 1999 data.

The zenith cuts used and the resulting number of events for the blind data subsets after filter level six is given in appendix C - in Table C.3 for the individual optimisation per year, and in Table C.4 for the combined livetime. The precision

		Combined optimisation			
		Hard channels		Soft channels	
Year	M_χ (GeV/c^2)	N_{data}	$N_{atm.\nu}$	N_{data}	$N_{atm.\nu}$
1997	100	45	62.84	34	41.76
	250	38	52.53	48	65.16
	500	40	51.86	48	61.41
	1000	33	50.56	29	45.94
	3000	30	50.30	36	51.92
	5000	31	48.51	35	52.28
1998	100	33	39.18	22	32.30
	250	30	38.06	15	22.36
	500	16	29.66	16	27.22
	1000	23	31.61	24	30.80
	3000	13	21.74	17	25.80
	5000	22	29.11	30	34.67
1999	100	48	69.80	48	85.01
	250	54	82.56	52	77.13
	500	46	70.62	48	75.35
	1000	49	72.35	47	75.36
	3000	36	62.95	53	85.23
	5000	39	63.95	51	76.99

Table 7.6: The number of events of data and the atmospheric neutrino background simulations that remain after the level five filter for all the analyses 1997-99.

of the cut value is equal to the bin size 0.5°

The efficiency of each analysis can be represented by the effective volume for the signal

$$V_{eff} = V_{gen} \cdot N_{L6}/N_{gen}, \tag{7.6}$$

where N_{L6} is the number of WIMP signal events that pass the final cut and N_{gen} is the number of events originally generated in the volume V_{gen}, see Fig. 7.6.

7.6 Unblinded Results

After all the cuts for the different signals have been developed and the various distributions agree the optimisation samples are discarded. The cuts were then applied to the remaining $\sim$ 80 % of the data for the three years which will be used to derive the results of this analysis.

The total livetime of this three year sample is 421.92 days, made up of 100.05 days in 1997, 145.68 days in 1998 and 176.18 days in 1999.

7.6.1 Filter Level Five

The number of events observed in data after the level five filtering and the number expected from the atmospheric neutrino simulation is presented in Table 7.6.

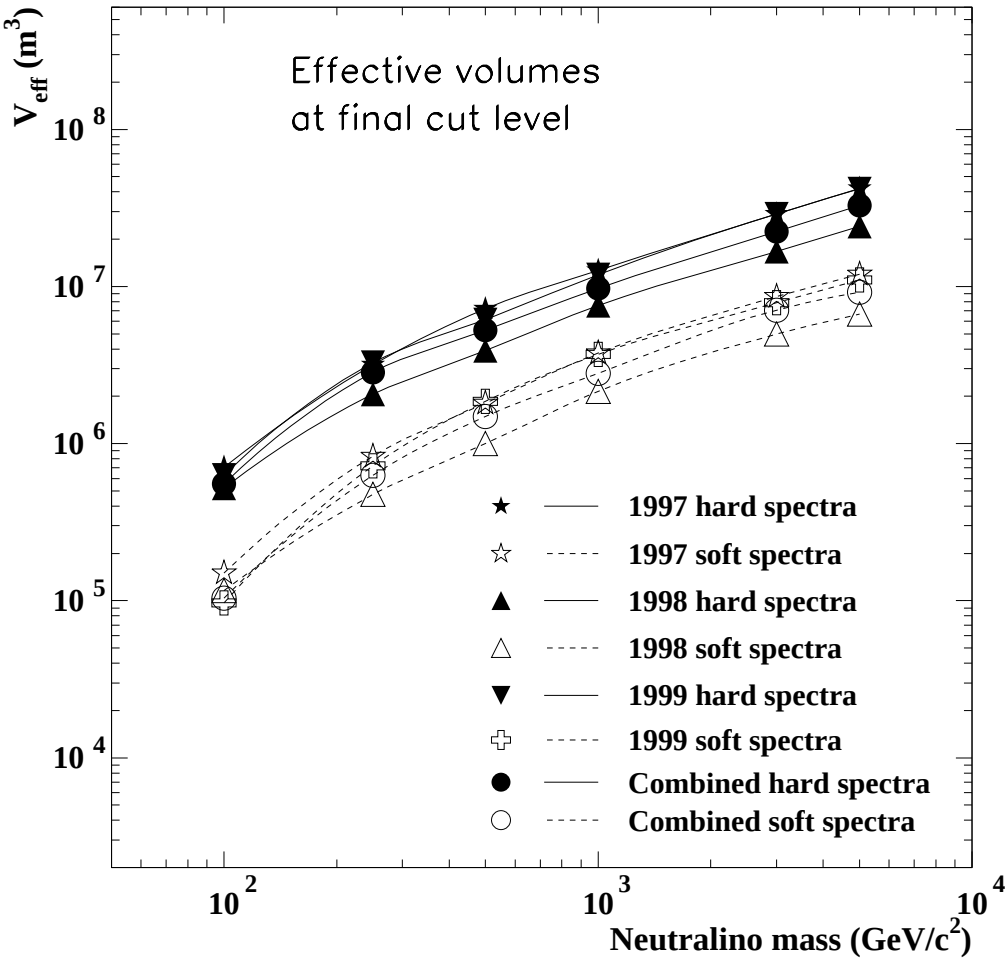

Figure 7.6: The effective volumes for the simulated WIMP signal after filter level six.

Joint sets at level five			
Year	N_{data}	$N_{atm.\nu}$	N_{data} / $N_{atm.\nu}$
1997	52	68.15	0.76 ± 0.11
1998	42	45.53	0.92 ± 0.14
1999	62	98.84	0.63 ± 0.08

Table 7.7: The number of events in the joint sets of data and the atmospheric neutrino background simulations that remain after the level five filtering in 1997, 1998 and 1999.

The twelve analyses for each year are highly correlated and there is substantial overlap between the events that pass the different filter chains. One way to try to bypass this correlation issue when comparing the filtered data to simulation is to produce a joint set of the events that pass the level five filtering of any analysis for each year. This is accomplished by putting the resulting events for all twelve sets in each year together and removing all the duplicates so that each event only occurs once. It is possible to compare the shape of the distributions of the unblinded data samples and the simulated atmospheric neutrino expectation at level five by means of a Kolmogorov-Smirnov (KS) test (see e.g. [143]). The result for the total livetime when combining the three yearly joint sets is presented in Fig. 7.7. From the top plot, which shows the angular distributions between 140° and 180° it is clear that they show excellent agreement. In the KS test the cumulative distributions for the two sets are compared, these are shown in the middle plot, by finding the largest deviation between the two curves $D_{max} = \max |F_{data}(\theta) - F_{atm.\nu}(\theta)|$. Finally, the bottom plot is the cumulative difference function D_{KS} which gives the KS test value $D_{max} = 0.057$. This corresponds to a probability of 68.4 % for the null hypothesis that these two distributions, the data events and the atmospheric neutrino simulation, are drawn from the same underlying population. This does not say anything about the absolute normalisation of the two distributions or the ratio of the number of events in data to the expectation from the Monte Carlo simulation of the atmospheric neutrino background. The number of events in the joint sets of each year as well as the ratios are given in in Table 7.7. The weighted mean of these three ratios is 0.72 ± 0.06. Using this to calculate a χ^2 the result is 3.95 with 2 degrees of freedom which translates into a probability of 13.9 %.

7.6.2 Filter Level Six

The final results for each analysis in the combined optimisation, the level six cut along with the number of events that pass this cut, is given in Table 7.8 (the numbers for the individual optimisations are given in appendix C, Table

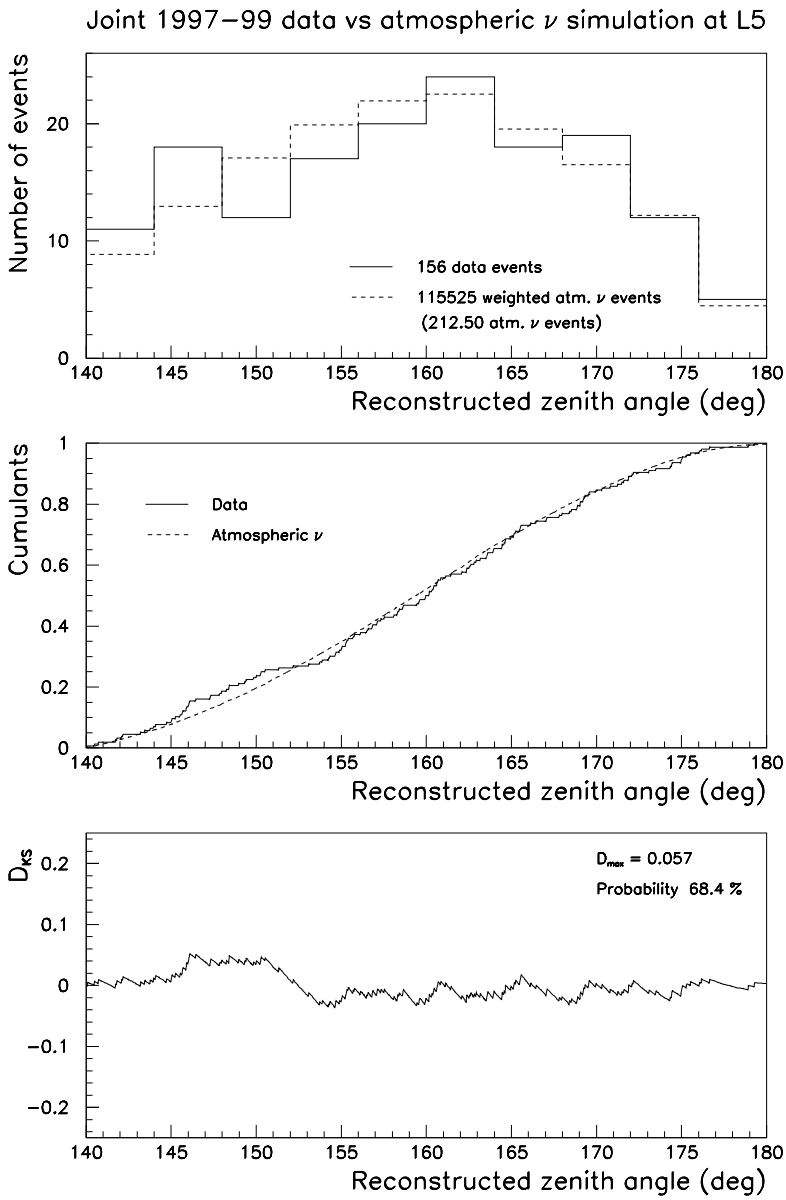

Figure 7.7: Comparing the joint distributions of the combined data and the simulated atmospheric neutrino background at level five with a Kolmogorov-Smirnov test. Top: the normalised distributions, center: the cumulative distributions and bottom: the cumulative difference with the largest value, D_{max}, and the probability.

		Combined optimisation							
		Hard annihilation channels				Soft annihilation channels			
Year	M_χ	θ_{cut}	N_{wimp}	N_{data}	$N_{atm.\nu}$	θ_{cut}	N_{wimp}	N_{data}	$N_{atm.\nu}$
	100	174.0°	5170	2	3.34	173.5°	834	2	3.31
	250	175.5°	11783	2	2.27	175.5°	2238	2	2.26
1997	500	176.5°	11287	2	1.40	175.5°	3022	2	2.24
	1000	177.5°	10914	1	0.75	176.5°	3314	2	1.44
	3000	177.5°	13179	1	0.75	176.5°	4233	2	1.44
	5000	177.5°	9628	1	0.74	177.5°	2431	1	0.76
	100	174.0°	3687	1	3.14	174.0°	607	1	2.87
	250	175.0°	7665	1	2.05	175.0°	1537	1	2.04
1998	500	176.0°	7114	1	1.41	176.0°	1674	1	1.38
	1000	176.5°	7602	0	1.08	176.0°	2190	1	1.41
	3000	176.5°	8411	0	1.13	176.5°	2313	0	1.08
	5000	176.5°	5993	0	1.16	176.5°	1630	0	1.15
	100	173.5°	4734	8	7.21	173.5°	556	7	6.91
	250	174.5°	12151	6	5.24	174.0°	2332	9	6.27
1999	500	176.5°	10275	1	2.15	175.5°	2777	3	3.62
	1000	176.5°	12688	1	2.17	176.5°	3042	1	2.22
	3000	177.5°	12278	1	1.08	176.5°	3874	1	2.22
	5000	177.5°	8887	1	1.17	176.5°	2690	1	2.22

Table 7.8: The results after the level six cut for the combined livetime of 421.92 days in 1997-99, M_χ in units of GeV/c^2.

C.5). As indicated in section 7.5.2 the zenith cuts for the combined analyses were optimised yearly as if the expected background for that year had a livetime of 412.92 days. The efficiencies after each of the various filter levels relative to the trigger level for the four different sets of events in one of the analyses are shown in Fig. 7.8.

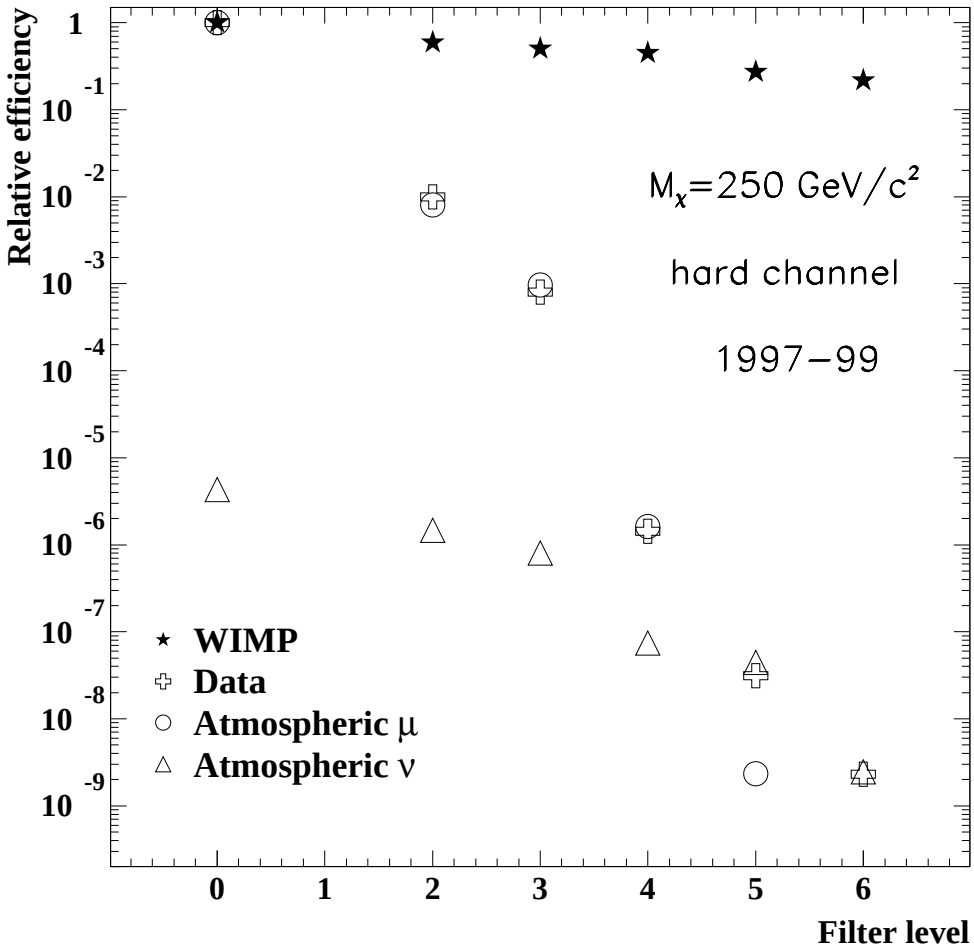

Figure 7.8: The efficiencies relative to the trigger level for the combined data, WIMP signal, atmospheric muon and atmospheric neutrino simulations after the different filter levels in the M_χ =250 GeV/c^2 hard annihilation channel analysis.

Chapter 8

Flux Limits

8.1 Calculating Limits

After the level six filtering the number of observed events agrees with the background expectation of atmospheric neutrinos. This leaves little room for any potential nearly vertically upgoing signal and it is therefore possible to calculate an upper limit at a certain confidence level on any muon flux from neutralino annihilations at the centre of the Earth.

The chosen confidence level (CL) in this work is the common choice of 90 % and the unified approach of Feldman-Cousins (FC) [142] for the construction of confidence belts has been used.

Using the 90 % CL limit μ_{90} on the number of muons from the expected signal together with the effective volume V_{eff}, as defined in Eq. (7.6) and shown in Fig. 7.6, and the experimental livetime T_{eff} it is possible to constrain the conversion rate of neutrinos into muons $\Gamma_{\mu\nu}$ per unit volume and time around the detector

$$\Gamma_{\mu\nu} \leq \frac{\mu_{90}}{V_{\text{eff}} \cdot T_{\text{eff}}} \tag{8.1}$$

for muons with an energy larger than the threshold energy E_{thr}. The rate $\Gamma_{\mu\nu}$ is model dependent through the use of V_{eff} which has been determined for twelve fixed combinations of neutralino masses and annihilation channels in the simulations of the neutralino signal.

In order to convert the upper limit on the conversion rate in Eq. (8.1) to an upper limit on the muon flux from neutralino annihilations at the centre of the Earth it is useful to first calculate the limit on the annihilation rate of the neutralinos. The conversion rate $\Gamma_{\mu\nu}$ is directly proportional to the annihilation

rate Γ_A [104,144] through

$$\Gamma_{\mu\nu} = \Gamma_A \cdot \frac{1}{4\pi R_\oplus^2} \int d\mathrm{E}_\nu \sigma_{\nu N}(\mathrm{E}_\nu) \rho_N \sum_X BR(\chi\bar{\chi} \to X) \Big(\frac{dN}{d\mathrm{E}_\nu}\Big)_X \tag{8.2}$$

where $R_\oplus$ is the radius of the Earth, $\sigma_{\nu N}$ is the neutrino-nucleon cross section, ρ_N is the nucleon density in the ice around the detector and $BR(\chi\bar{\chi} \to X)$ is the different branching ratios for the neutralino annihilation with associated neutrino spectrum $\left(\frac{dN}{d\mathrm{E}_\nu}\right)_X$. In this work the simulated signal samples have been generated for a specific neutralino mass and annihilation channel so the sum over spectra in Eq. (8.2) consists of a single term for each sample. The annihilation rate depends on the neutralino model assumptions used and the derived 90 % CL limits on Γ_A can be compared directly with the predictions of other models. Since the detector thresholds and efficiencies are taken into account in the calculation of the limits these are also directly comparable to those of other experiments.

The neutralino annihilation rate at the centre of the Earth is then used to calculate the 90 % CL upper limit on the muon flux ϕ_μ for any given energy threshold $\mathrm{E_{thr}}$ by using the relation [104,144]

$$\phi_\mu(\mathrm{E}_\mu \geq \mathrm{E_{thr}}) = \frac{\Gamma_A}{4\pi R_\oplus^2} \int_{\mathrm{E_{thr}}}^{\infty} d\mathrm{E}_\mu \frac{dN}{d\mathrm{E}_\mu} \tag{8.3}$$

where the differential term $dN/d\mathrm{E}_\mu$ includes all the assumptions necessary to account for the production of muons from neutrinos created by neutralino annihilations as well as the muon propagation to the detector. This calculation can be done for any energy threshold and not just the actual effective energy threshold of the detector. In order to compare the 90 % CL upper limits on the muon flux derived in this work with published results of other experiments as well as earlier analyses the threshold of 1 GeV have been used. The conversion factors used with Eqs. (8.2) and (8.3) for converting $\mu_{90} \to \Gamma_A \to \phi_\mu$ has been calculated with code based on simulations presented in [131].

8.2 Combined Limits

As presented in the previous chapter the data events and the simulated background of muons induced by atmospheric neutrinos have been filtered separately for each year, neutralino mass and annihilation channel. The number of observed events and the background expectation for all three years as presented in Table 7.8 are added per neutralino mass and annihilation channel to form a combined result for data from 1997-99 for the twelve different analyses.

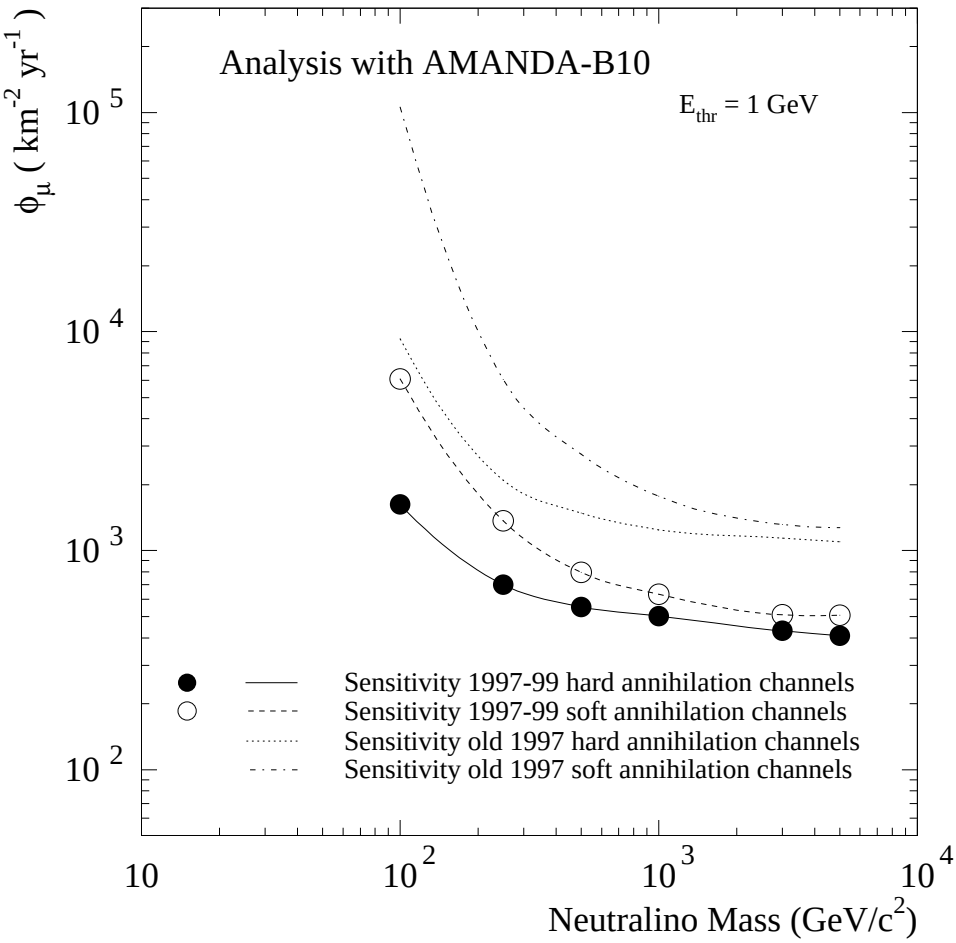

Figure 8.1: The muon flux sensitivity for the combined 1997-99 data corresponding to 421.92 days of livetime. The sensitivity for the old 1997 analysis [104], with a livetime of 130.1 days, is shown for comparison. No systematic uncertainties have been included in the calculation of the upper limits.

Annihilation rate and muon flux limits for combined analyses, T_{eff} = 421.92 days						
Channel	M_χ (GeV/c^2)	N_{data}	$N_{atm.\nu}$	μ_{90}^{FC}	Γ_A (s^{-1})	ϕ_μ^{FC} (km^{-2}yr^{-1})
Hard	100	11	13.7	4.3	4.1×10^{13}	906.4
	250	9	9.6	5.7	3.8×10^{12}	604.7
	500	4	5.0	3.5	6.0×10^{11}	372.9
	1000	2	4.0	2.3	1.1×10^{11}	235.9
	3000	2	3.0	2.9	1.9×10^{10}	283.4
	5000	2	3.1	2.9	7.8×10^{9}	263.6
Soft	100	10	13.1	3.7	9.6×10^{14}	3000.1
	250	12	10.6	8.3	9.1×10^{13}	1644.7
	500	6	7.2	4.3	9.2×10^{12}	580.2
	1000	4	5.1	3.5	2.1×10^{12}	417.5
	3000	3	4.7	2.9	2.8×10^{11}	289.2
	5000	2	4.1	2.1	1.1×10^{11}	217.8

Table 8.1: The Feldman-Cousins muon flux upper limits ϕ_μ^{FC} for the combined 97-99 data analyses. The results have been calculated without including systematic uncertainties.

The sensitivity is the average upper limit, as defined in Eq. (7.5), i.e. the limit that would be set if there was no signal present and all the observed events can be attributed to the background and if the experiment could be repeated a number of times (hypothetically). Using the combined result for the atmospheric neutrino background to calculate the average 90 % CL upper limit $\langle \mu_{90}^{FC} \rangle$ it is then possible to calculate the muon flux sensitivity for the 1997-99 analysis. Likewise, using the corresponding values in Table II in [104] the sensitivity of the previous AMANDA-B10 neutralino analysis can be derived and the two are plotted and compared in Fig. 8.1. The livetime has increased with a factor of 3.2 from 130.1 days to 421.92 days between the two sets of average limits but there are also differences in the simulations used for estimating the effective volume of the signal and number of expected background events. Still, even though the more accurate simulations have decreased the sensitivity slightly the sensitivity has increased with a factor of 2.7 for the 5000 GeV/c^2 hard annihilation channel and 17.4 for the 100 GeV/c^2 soft annihilation channel.

For the combined analysis with data from 1997-99 the 90 % confidence level upper limits for the number of neutralino signal events, the annihilation rate and the muon flux is presented in Table 8.1 for the twelve combinations of neutralino mass and annihilation channels. The upper limits on the muon flux from neutralino annihilations at the centre of the Earth are plotted in Fig. 8.2 where they are also compared to the results in the previous analysis published in [104]. These upper limits have been calculated without including the effects of systematic uncertainties, which when included will raise the limits slightly. Fluctuations in the small number of observed events account for the fact that the limit points do not

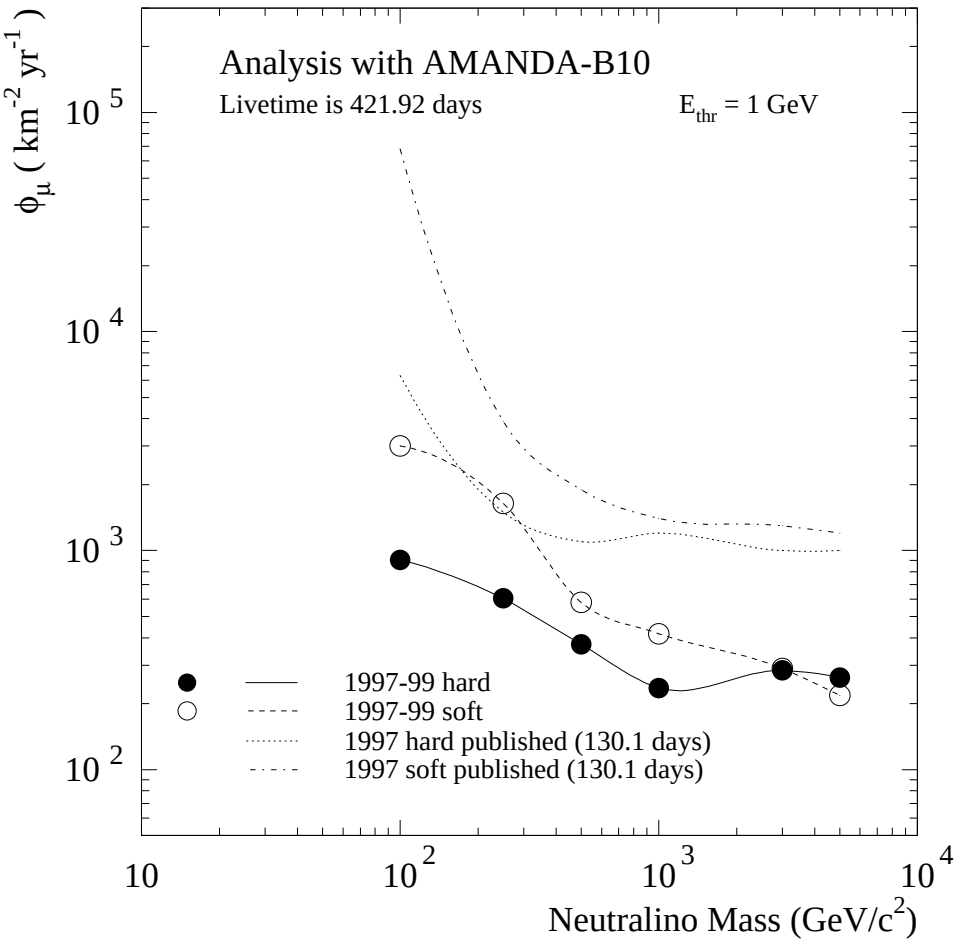

Figure 8.2: The upper limits on the muon flux from neutralino annihilations at the centre of the Earth for the combined 1997-99 data corresponding to 421.92 days of livetime. The published limits for the old 1997 analysis [104], with a livetime of 130.1 days, is shown for comparison. No systematic uncertainties have been included in the calculation of the upper limits.

decrease in the smooth way illustrated in the sensitivity plot. It is a feature of the Feldman-Cousins way of constructing confidence belts that downward fluctuations improves the limits and in most of the analyses the number of observed events is slightly lower than the expectation (see the columns with N_{data} and $N_{atm.\nu}$ in Table 8.1). In the case of the 250 GeV/c^2 soft annihilation channel the slight excess results in a worse limit.

8.3 Systematic Uncertainties

The inclusion of systematic uncertainties for the signal and background estimates in the limit calculations is done using the POLE program [145,146] which is a generalisation of the method proposed in [147]. The calculation takes into account the uncertainty in the signal detection efficiency as well as both the theoretical and the detection efficiency uncertainty of the background.

The theoretical uncertainty in the atmospheric neutrino flux calculation is estimated to be ~ 20 % and that it is a uniform distribution, i.e. there is an equal probability for all values within ± 20 % of the flux used as input to the simulation. A conservative assumption of ± 25 % will be used in the limit calculations.

The systematic uncertainty in the detection efficiency is dominated by three contributions: OM sensitivity, muon energy loss and the implementation of the ice properties in the detector simulation.

The uncertainty in the OM sensitivity is in part due to the transmissivity of the glass and optical gel and in part due to the quantum and collection efficiency of the PMT. The transmissivity of the optical modules have been measured by the collaboration and the uncertainty is ~ 10 %. The efficiency of the PMTs has an uncertainty of up to 20 % according to the manufacturer Hamamatsu. Adding these two contributions the uncertainty in the OM sensitivity is thus ~ 20 %. Simulation studies of atmospheric neutrinos [148] have shown that this will propagate through to an uncertainty in the muon rate of ~ 30 % for muons with an energy in the range 10^2–10^3 GeV (which is the typical energy range for the muons in this work), while for higher energies ($> 10^3$ GeV) it is lower (~ 10 %).

From the simulation of the muon propagation to the detector there is a $\lesssim 10$ % uncertainty in the muon range [12]. The muon flux at the detector is proportional to the range of the muon [129] and therefore a 10 % uncertainty on the number of muons have been chosen as the contribution of this effect to the overall systematic uncertainty.

The uncertainty in the detection efficiency due to the implementation of the ice properties in the detector simulation has been estimated by using two different ice models in the simulation of the neutralino signal as well as in the atmospheric

	Systematic uncertainties							
	Hard annihilation channels				Soft annihilation channels			
M_χ (GeV/c^2)	σ^{ice}_{wimp}	$\sigma^{ice}_{atm.\nu}$	σ^{tot}_{wimp}	$\sigma^{tot}_{atm.\nu}$	σ^{ice}_{wimp}	$\sigma^{ice}_{atm.\nu}$	σ^{tot}_{wimp}	$\sigma^{tot}_{atm.\nu}$
100	12 %	8 %	34 %	33 %	20 %	11 %	37 %	33 %
250	10 %	16 %	33 %	35 %	9 %	16 %	33 %	35 %
500	8 %	21 %	33 %	38 %	10 %	17 %	33 %	36 %
1000	8 %	22 %	33 %	38 %	9 %	19 %	33 %	37 %
3000	8 %	15 %	33 %	35 %	7 %	25 %	32 %	40 %
5000	10 %	17 %	33 %	36 %	8 %	19 %	33 %	37 %

Table 8.2: The uncertainty in the signal and background efficiency due to the effects of ice in the simulations as well as the total uncertainty when including effects of OM sensitivity, muon propagation and neutrino-nucleon cross section.

neutrino background. The MAM-model which is used for the limit results have been compared with the KGM-model. The standard deviation of the number of events that remain after the final level six filter is used to calculate an uncertainty for each of the 36 analyses. For every mass and annihilation channel the three years are combined to an uncertainty for the combined result. The systematic effect from the ice for signal, σ^{ice}_{wimp}, and background, $\sigma^{ice}_{atm.\nu}$, as well as the total systematic uncertainty of signal and background, σ^{tot}_{wimp} and $\sigma^{tot}_{atm.\nu}$, is presented in Table 8.2.

There are other effects that could contribute to a systematic uncertainty but the effects are small compared to the three mentioned above.

Potential contamination of misreconstructed downgoing atmospheric muons in the final sample has been evaluated by using a second set of simulated events. This set corresponds to 109.7 days of atmospheric muons for the 1999 detector configuration (the livetime of 1999 data is 176.2 days). No events passed the level six filtering for any of the twelve combinations of neutralino mass and annihilation channel. In order to quantitatively say something about any such background contamination it is necessary to simulate more background livetime than the data sample in question. But zero observed events for this limited case does not contradict the approach of excluding any atmospheric muon contribution in the final limit calculations, which is in fact conservative since including any estimate on atmospheric muons in the limit calculation would produce better limits.

In the simulations of the neutralino signal the simplified assumption that the neutrino-nucleon interaction and subsequent muon propagation takes place in ice alone is used. For the samples with a high neutralino mass the generation volume is so large that it also dips down into the rock beneath the glacial ice surrounding the detector.

The flexibility of using two different media has not yet been implemented in

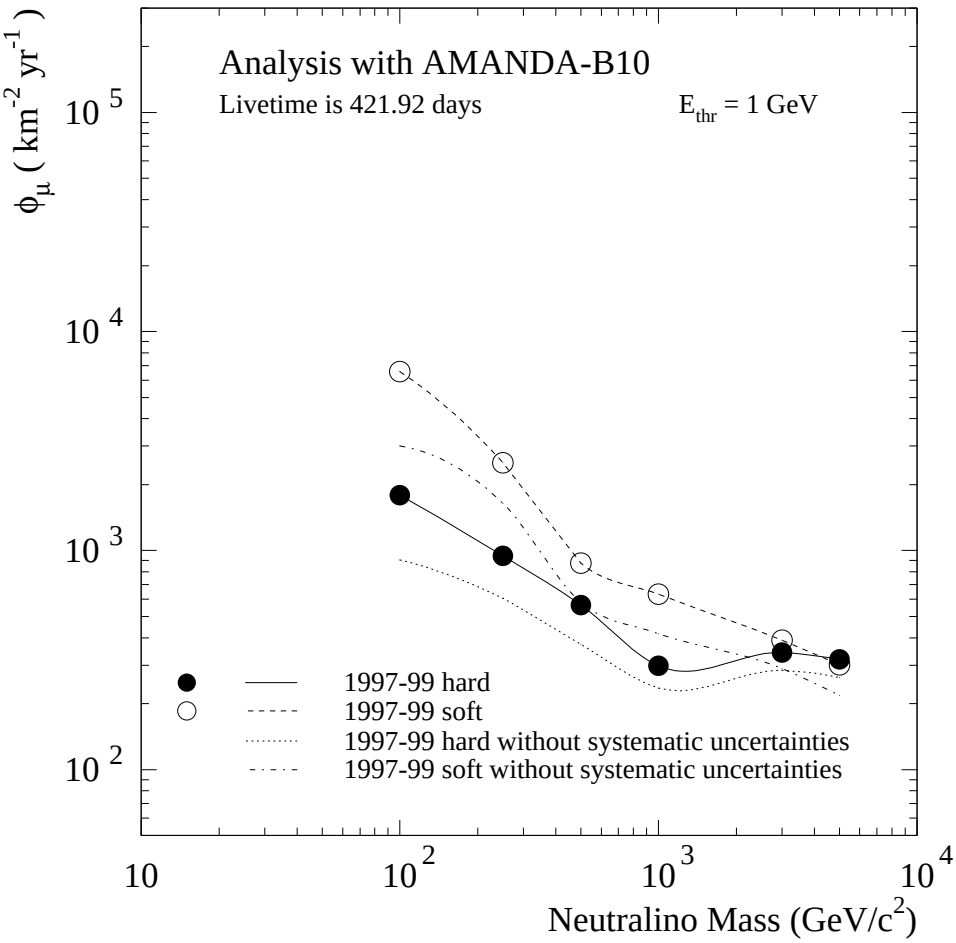

Figure 8.3: The upper limits on the muon flux from neutralino annihilations at the centre of the Earth for the combined 1997-99 data corresponding to 421.92 days of livetime. The published limits for the old 1997 analysis [104], with a livetime of 130.1 days, is shown for comparison. Systematic uncertainties have been included in the calculation of the upper limits.

Annihilation rate and muon flux limits for combined analyses, T_{eff} = 421.92 days						
Channel	M_χ (GeV/c^2)	N_{data}	$N_{atm.\nu}$	μ_{90}	Γ_A (s^{-1})	ϕ_μ (km^{-2}yr^{-1})
Hard	100	11	13.7	8.5	8.1×10^{13}	1791.8
	250	9	9.6	8.9	5.9×10^{12}	944.2
	500	4	5.0	5.3	9.1×10^{11}	564.6
	1000	2	4.0	2.9	1.3×10^{11}	297.4
	3000	2	3.0	3.5	2.3×10^{10}	342.1
	5000	2	3.1	3.5	9.4×10^{9}	318.1
Soft	100	10	13.1	8.1	2.1×10^{15}	6567.8
	250	12	10.6	12.7	1.4×10^{14}	2516.6
	500	6	7.2	6.5	1.4×10^{13}	877.1
	1000	4	5.1	5.3	3.2×10^{12}	632.2
	3000	3	4.7	3.9	3.8×10^{11}	388.9
	5000	2	4.1	2.9	1.5×10^{11}	300.7

Table 8.3: The 90 % confidence level upper limits on the annihilation rate Γ_A and the muon flux ϕ_μ calculated with the inclusion of systematic uncertainties for the combined 97-99 data analyses.

the software used for the generation of the neutralino signal simulation samples. However, "standard rock" is defined to have a mean Z=11 and a mean A=22 which is similar to the the values used for ice (Z=10 and A=18). Therefore the ratio of protons to neutrons is similar and although the density of rock is not taken into account it is possible to check the effect on the muon propagation by the use of different media. As the increase in neutrino-nucleon interactions due to the higher density of rock is not considered this will be an overestimation of the overall effect of using both rock and ice.

To check this effect another set of muon samples for each neutralino mass and annihilation channel were generated where again all the neutrino-nucleon interactions occurred in ice. The two different media were then taken into account in the propagation of the muon from the vertex to the detector. For the hard annihilation channels the effect is a decrease in the number of events after the level six filtering for the three heaviest neutralino masses with 19 % (1000 GeV/c^2), 41 % (3000 GeV/c^2) and 49 % (5000 GeV/c^2). In the case of the soft annihilation channels only the two heaviest M_χ are affected, with a drop of 15 % (3000 GeV/c^2) and 23 % (5000 GeV/c^2). This effect have not been included in the calculation of the final results.

8.4 Comparison with Theory and Other Experiments

As described in chapter 2 there are several other experiments that have performed searches for dark matter using direct as well as indirect detection techniques. A comparison of the limits presented in Table 8.3 in the previous section with results

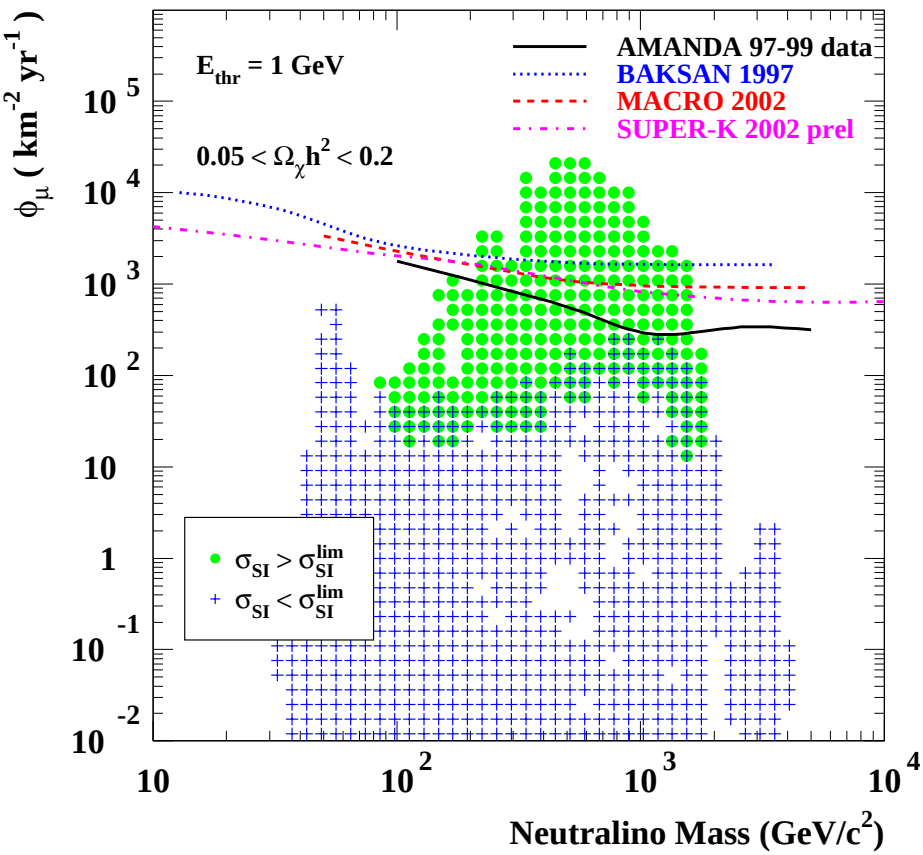

Figure 8.4: The AMANDA limits on the muon flux from neutralino annihilations at the centre of the Earth for the three year 97-99 combined data set compared with those of Baksan, Macro and Super-Kamiokande. MSSM model predictions [151] are also shown, the grey dots indicate models that are excluded by EDELWEISS and the plus signs those that are not excluded.

from the indirect searches with the Baksan underground scintillator telescope [149], the Macro detector [97] and Super-Kamiokande [100,150] are shown in Fig. 8.4 (this figure is analogous to Fig. 2.4). For the comparison the limits of the other experiments have also been converted to limits with a threshold of 1 GeV (1.5 GeV for Super-Kamiokande). The Super-Kamiokande limits have also been corrected to represent the total flux instead of the flux inside a cone that contains 90 % of the signal.

The points in Fig. 8.4 represent muon flux predictions from neutralino annihilations calculated with different combinations of parameters in the Minimal Supersymmetric Standard Model (MSSM). The particular MSSM model used (see [151] for more details) have seven free parameters that are varied to create a grid of flux predictions and the models with the highest fluxes are included in the figure. The parameters are the Higgsino mass parameter μ, the gaugino mass parameter M_2, the mass of the CP-odd Higgs boson m_A, the ratio of the Higgs vacuum expectation values $\tan\beta$, the sfermion mass scale $M_{\tilde{q}}$ and the parameters A_t and A_b from the supersymmetry breaking assumptions. Further restrictions on the models included in Fig. 8.4 are that they should not have been ruled out by accelerator experiments and that they should yield relic densities of neutralinos such that $0.05 < \Omega_\chi h^2 < 0.2$.

The results from direct detection experiments are not directly comparable to those using indirect detection, and they are in a sense complementary. The direct detection experiments set limits on the spin-independent neutralino-nucleon cross section σ_{SI} for given neutralino masses. They are more sensitive to high velocity neutralinos while the indirect techniques which require that dark matter particles collect in gravitational wells are more sensitive to low velocity WIMPs. The MSSM models used to calculate the flux points in Fig. 8.4 have also been evaluated with respect to the cross section limits σ_{SI}^{lim} set by the EDELWEISS experiment [72] and the models that are excluded by their measurements where $\sigma_{SI} > \sigma_{SI}^{lim}$ are indicated by grey full circles in Fig. 8.4. The models that are not excluded are plotted with plus signs.

This comparison is of course dependent on the assumptions made about the velocity distribution of the neutralino particles in the galaxy and especially within the solar system. For the comparison the standard Maxwell-Boltzmann distribution, based on the results in [152], was used and if a more realistic distribution had been used the result of which models are excluded could change due to the different sensitivities for high and low velocity neutralinos [151].

The neutralino particles that presumably have accumulated at the centre of the Earth have been trapped from a local distribution in the solar system. This local distribution have diffused through the system due to interactions with the planets. This process have recently been re-investigated and the result is

a new velocity distribution which has the effect of lowering the predicted muon flux in the MSSM models [151]. The model predictions using the new velocity distribution from the new solar system diffusion analysis is shown in Fig. 8.5.

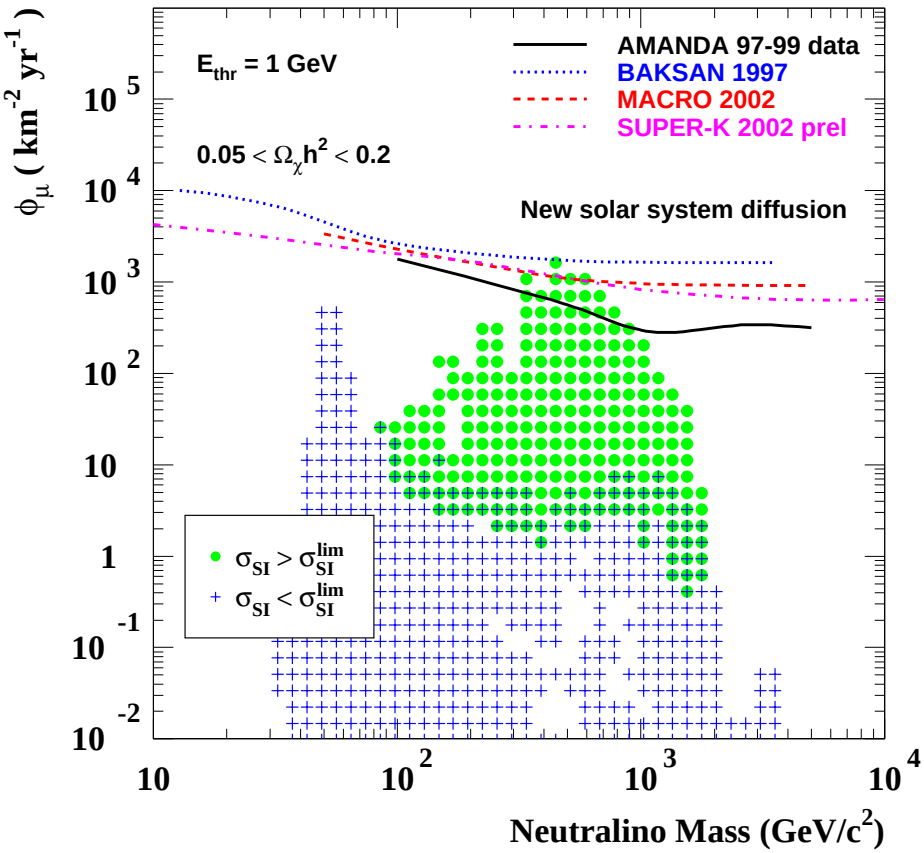

Figure 8.5: The AMANDA limits on the muon flux from neutralino annihilations at the centre of the Earth for the three year 97-99 combined data set compared with those of Baksan, Macro and Super-Kamiokande. MSSM model predictions with new estimates on the WIMP diffusion in the solar system [151] are also shown, the grey dots indicate models that are excluded by EDELWEISS and the plus signs those that are not excluded.

Chapter 9

Conclusions and Outlook

A search has been performed for nearly vertically upgoing muons with AMANDA data from the three years 1997-99 as these could be a signature of dark matter in the form of neutralinos accumulating and annihilating at the centre of the Earth. The number of muons found as well as the angular distribution of these is compatible with the expected background induced by atmospheric neutrinos. The results have been used to derive limits as a function of neutralino mass on the annihilation rate and the neutrino induced muon flux.

The limits are a significant improvement over the ones that were obtained and published for an earlier AMANDA analysis that used only data taken in 1997. As shown in a comparison with other indirect detection experiments (see Fig. 8.4) the new set of limits is currently better than those of the Macro and Super-Kamiokande collaborations.

One improvement over the old 1997 analysis is that the cuts for each neutralino mass and annihilation channel have been optimised individually. Although in hindsight the gain from this was not as large as was hoped beforehand. Instead the largest improvement comes from the use of neural networks for the rejection of background events which increased the signal to background ratio.

The problems with the 1998 level two filtering is annoying and in principle it should be redone, but practically this may not be feasible. A 50 % increase in the effective volume for the 1998 signal samples would yield $\sim 10 - 20$ % improvement in the effective volume for the combined samples. Under the assumption that the 1998 points in Fig. 7.6 are brought close to the level of the 1997 points or maybe even higher due to the low multiplicity threshold of the 1998 detector it might even be slightly larger than this. A $10 - 20$ % improvement in the effective volume would translate into a ~ 10 % improvement of the sensitivity for the combined analysis.

An improved sensitivity could also be achived by increasing the livetime

through the inclusion of later years. However there is a difference in the detector setup that makes such a combination non-trivial. With the larger AMANDA-II that was completed before the 2000 season a higher multiplicity threshold had to be used for the detector trigger condition during the years 2000-04. Since this raises the energy treshold of the detector it severly impacts the search for low energy muons such as those of interest in the low mass neutralino searches. For this reason a new separate correlation trigger have been implemented that requires that five out of nine OMs on a string are hit. This would recover some of the low energy muons and especially the nearly vertically upgoing ones. With simulations that take this into account it should be possible to combine the various years in proportion to their livetime. The difference in trigger condition means that the simulated samples should be combined before the cut optimisation is performed.

Better statistics for the signal simulation at lower neutralino masses (below 100 GeV) could also make it possible to train neural networks for these more difficult cases.

The systematic uncertainties are dominated by the uncertainty in the OM sensitivity and this can not really be improved upon. However, there is an improved detector simulation under development that will feature routines with a more realistic implementation of the photon propagation. This could change the estimation of the effect on the muon rate by the change in the OM sensitivity, but it is impossible to guess if it does (or if it will improve or worsen the uncertainty estimate).

A proper evaluation of the effect of the rock beneath the detector needs to be done, preferably by the full inclusion of the two different media in the signal simulation so that this effect could be accounted for with the high mass neutralinos.

The improved photon propagation routines will also be applied to the track and cascade reconstruction where it will replace the current pdf for the photon arrival times at the PMTs (see Eq. (5.7)). For future analyses better reconstructions could help to eliminate the need of some of the higher level cuts, i.e. simplify the analysis, and improve the efficiency of the neural networks.

Appendix A

Timing Calibration

A.1 Optical Fibre Transit Times

There are two types of optical fibres used in AMANDA, single-mode (SM) and multimode (MM) fibres. In an optical fibre the core carries most of the light and the surrounding glass cladding bends the light and confines it to the core. The single-mode fibre is designed to transmit light of a particular wavelength by having the core diameter be close in size to the wavelength of the light. The only source of pulse spreading in a SM fibre is chromatic dispersion, occurring since light of different wavelengths travel at different speeds.

The multimode fibre is designed to transmit a broader band and the core diameter is relatively large compared to the wavelength so that the light can propagate through the fibre along many different paths (modes). There are two main types of MM fibres. The step index fibre where the core has one single refractive index and the graded index fibre where the index of refraction across the core is gradually changed from a minimum near the edges to a maximum at the center. The light therefore propagates faster away from the centre so that rays traversing the fibre along longer paths take approximately the same time as the ones with shorter paths. In this way the pulse spreading in reduced considerably compared with the step indexed fibres.

The MM fibre used in AMANDA is the Corning 62.5/125, a graded index optical fibre with a 62.5 μm core diameter and a 125 μm cladding diameter. The SM fibre is also manufactured by Corning.

In the AMANDA-B10 design the fibres are paired up so that one fibre of each type is connected to each diffusion ball down in the ice. For the inner four strings a diffusing nylon sphere is located next to every OM while for the six outer strings it is located next to every second OM. The idea was to primarily use the SM fibres for timing calibration as the MM pulse is slightly wider than the SM pulse after

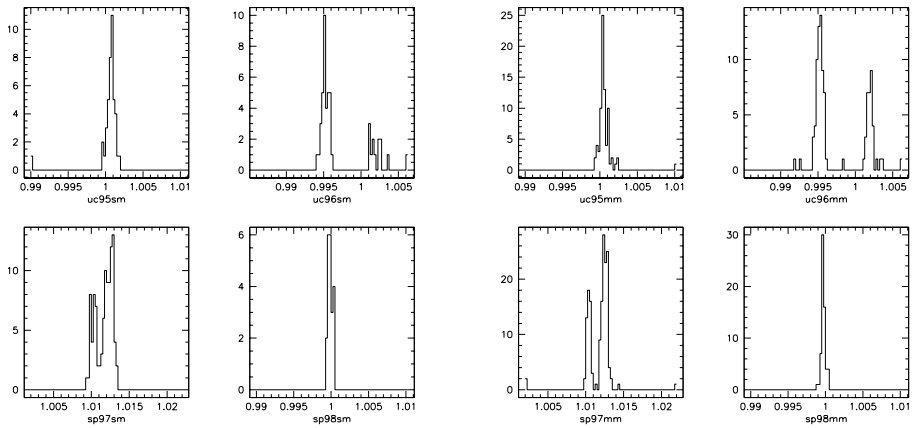

(a) Single-mode length ratios. Top left is the set measured at UC Irvine in October 1995 (strings 1-4) and top right is the set measured at UC Irvine in October 1996 (string 5-10). Bottom left is the set measured at the South Pole in January 1997 and bottom right is the set measured at the South Pole in January 1998.

(b) Multimode length ratios. Top left is the set measured at UC Irvine in October 1995 (strings 1-4) and top right is the set measured at UC Irvine in October 1996 (string 5-10). Bottom left is the set measured at the South Pole in January 1997 and bottom right is the set measured at the South Pole in January 1998.

Figure A.1: The plots show the optical fibre length ratios with respect to the set measured at the South Pole in December 1997. Plots from [153].

propagating through two kilometres of fibre.

The fast YAG laser pulses used for the timing calibration have a wavelength of 532 nm. It turned out not to be possible to measure the SM fibre transit times in the ice using this laser as there was not enough light returned to the surface (only a few SM fibres were successfully measured this way). Instead they were measured with a separate Optical Time Domain Reflectometer (OTDR) system that used 850 nm light.

The set of fibre transit times that is used for both the 1997-98 and 1998-99 timing calibrations is derived from several sets of OTDR measurements made at UC Irvine in October 1995 (for strings 1-4) and October 1996 (for strings 5-10) before the optical fibres were shipped to the Antarctic and on location with the fibres frozen into the ice at the South Pole in January 1997, December 1997, January 1998 and February 1998. For the UCI measurements a Tektronix OF150

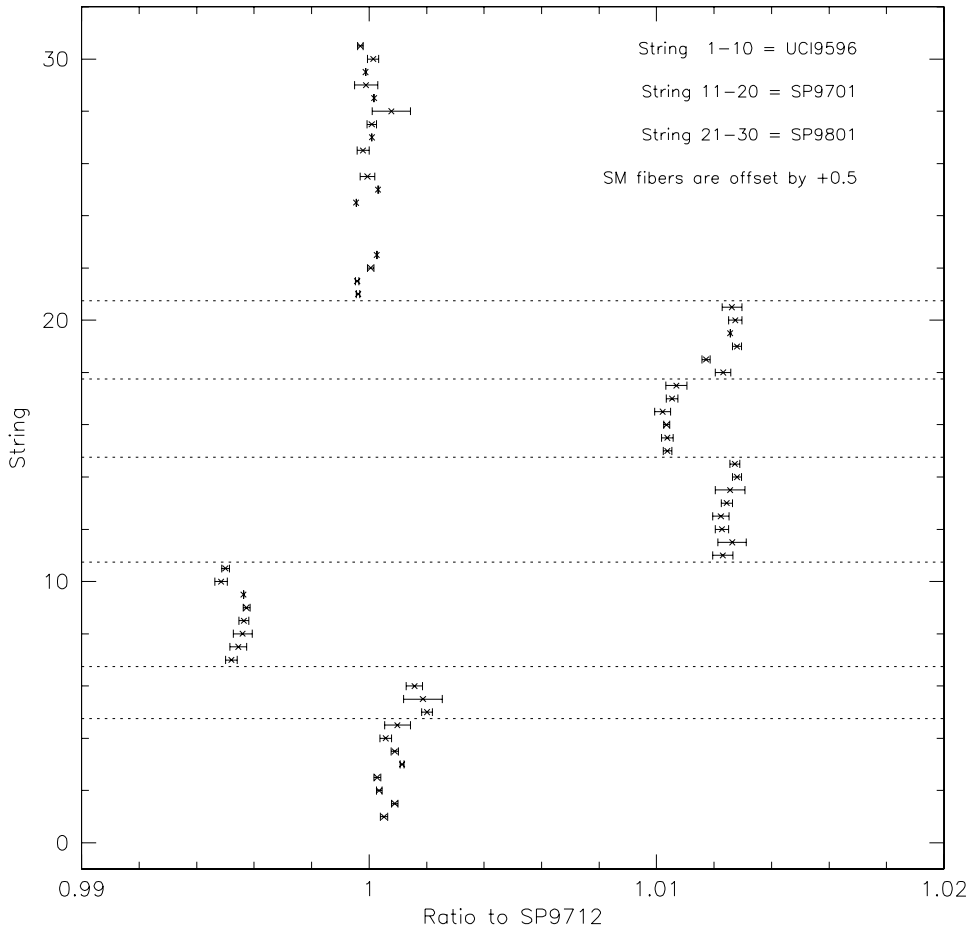

Figure A.2: The ratios of the measured AMANDA-B10 optical fibre lengths to the measurements taken at the South Pole in in December 1997. The UCI multimode ratios are numbered as string 1, 2, 3, ..., 10 and the UCI single-mode ratios as 1.5, 2.5, 3.5, ..., 10.5 (i.e. string number + 0.5). The January 1997 South Pole multimode lengths are numbered as 11, 12, ..., 20 and the single-mode as 11.5, 12.5, ..., 20.5 corresponding to the actual string numbers 1, 2, ..., 10. Finally the January 1998 multimode measurements for B10 are shown as string number 21, 22, ..., 30 and the single-mode as 21.5, 22.5, ..., 30.5. Plots from [153].

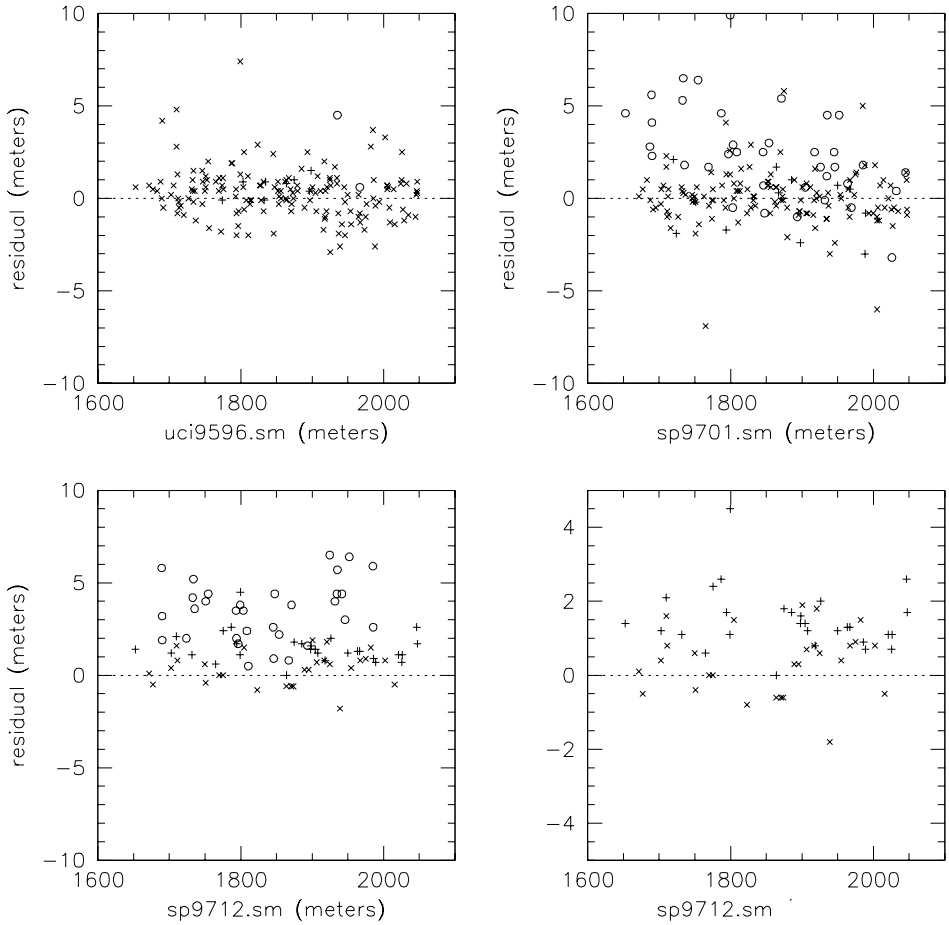

Figure A.3: The difference in length for single-mode fibres between the original data and the final, cross-calibrated, for the measurements done at UC Irvine (top left) and at the South Pole in January 1997 (top right) and December 1997 (bottom left). Plots from [153].

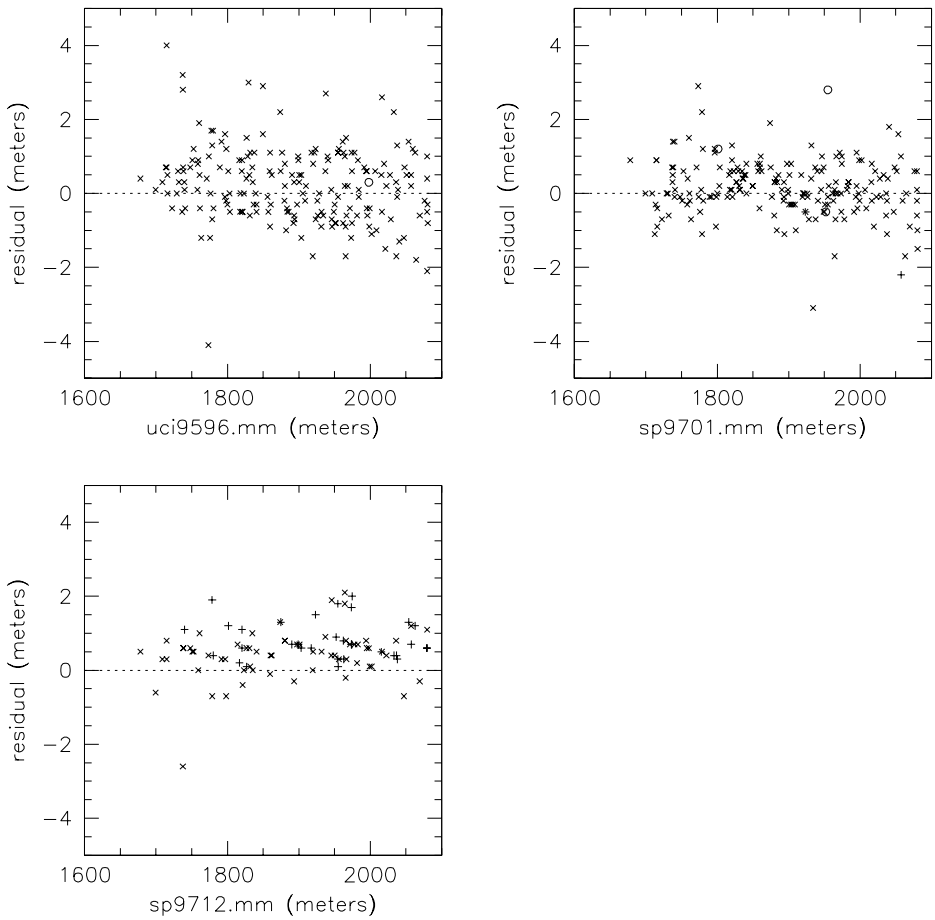

Figure A.4: The difference in length for multi-mode fibres between the original data and the final, cross-calibrated, for the measurements done at UC Irvine (top left) and at the South Pole in January 1997 (top right) and December 1997 (bottom left). Plots from [153].

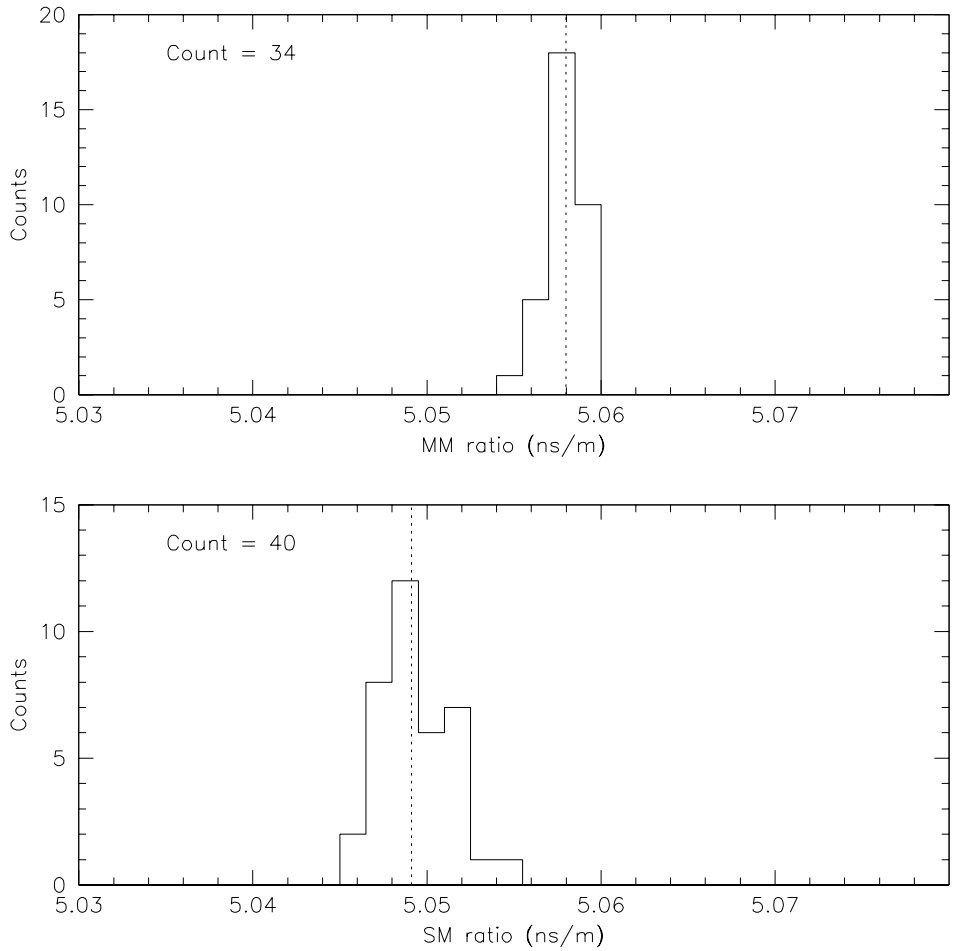

Figure A.5: The 850 nm to 532 nm conversion factor. The top plot shows the multimode data and the bottom plot the single-mode data. The single-mode data is not good enough (too wide) so only the multimode factor is used. Plots from [153].

was used.

The fibre length given by an OTDR measurement is affected by how fast light travels through it. It is important to calibrate the OTDR to the refractive index of the fibre in question and to use the same calibration constant for repeated measurements. In Fig. A.1 it appears that the length of certain fibres have changed over time (which is clearly unphysical) and the most plausible explanation is that the calibration factor used during the OTDR measurements had not been the same at the various times. To be able to use them all the different sets have been cross-calibrated and normalized to the complete set taken in December 1997 (see Fig. A.1) in order to compare them. The December 1997 set was chosen because the calibration factor was known to be constant since the measurements were made over a short period of time which apparently was not the case with earlier measurements. It was also assumed for the other sets that the calibration factor was constant for each string, again since that measurement was performed over a short period of time.

The ratios with respect to the December 1997 set is plotted in Fig. A.2 in a string by string manner for both the SM and MM data. In this plot the measurements are grouped as indicated by the dotted lines and after a calculation of the statistics of each group they were rescaled to the median value of the December 1997 set. This gives the 'master' length set which consists of the rescaled January 1998 values, or if that is not good or does not exist then the December 1997 measurement or lastly the rescaled UCI data. The difference between the data in the original sets and the final set is plotted as residuals in Figs. A.3 (SM) and A.4 (MM).

To get the 850 nm to 532 nm conversion (as the timing calibration is done with 532 nm laser light) the multimode measurements were used with the assumption

$$t_{MM,532} = constant \times L_{MM,850} \tag{A.1}$$

For the constant factor the SM and MM data is shown in Fig. A.5. The MM data have a $\sigma = 0.0008$ which corresponds to 1.7 ns for transit times over two kilometre of optical fibre. The SM data have a $\sigma = 0.002$ giving an uncertainty of 4 ns. Therefore the data was judged not to be sufficiently good for a SM conversion directly, mainly due to difficulties with getting enough light to propagate down the SM fibres and up again in order to do the OTDR measurement. So the MM times had to be used to get the SM times through

$$t_{SM,532} = t_{MM,532} + \Delta\mathrm{LE} \tag{A.2}$$

where the leading edge (LE) is the raw time read out from the DAQ when it was triggered by the laser pulses and ΔLE is the difference $\mathrm{LE}_{SM} - \mathrm{LE}_{MM}$.

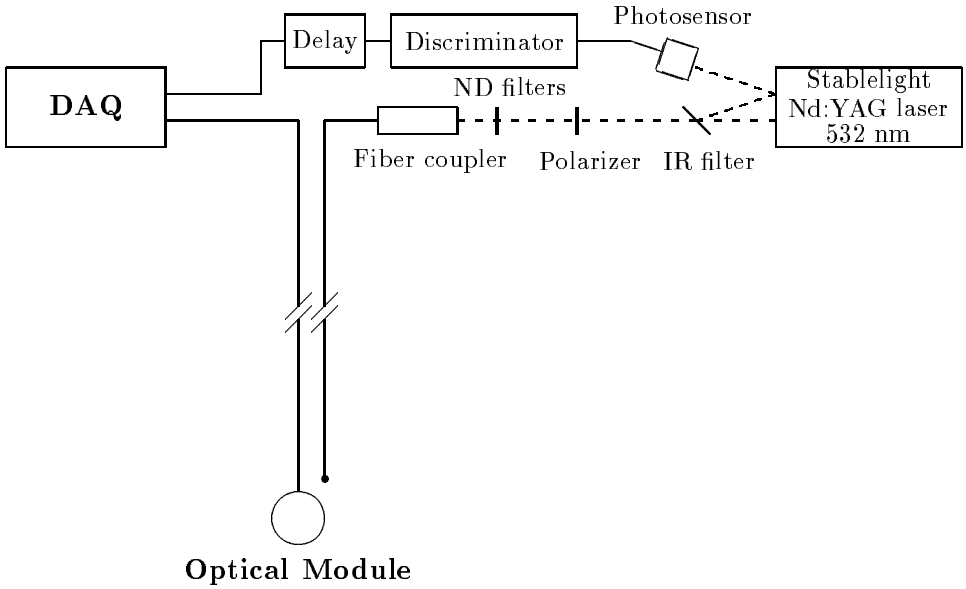

Figure A.6: The timing calibration setup.

A.2 Cable Transport Correction

The setup used for taking the timing calibration data is illustrated in Fig. A.6. The light source is a Uniphase Stablelight^{TM} laser with a Nd:YAG crystal which after frequency doubling (Q-switching) the original 1064 nm light produce 532 nm light pulses with a width of five nanoseconds. The laser beam was put through an IR filter and the reflected part used for getting a trigger by sensing it with a fast photo diode and the trigger pulse was then inverted before inputted into a discriminator (LeCroy 821). The discriminator signal was then delayed, 16-20 μs using a Stanford Research Systems DG535 four channel digital delay/pulse generator, to compensate for the optical fibre and electrical cable transit times of the light and the OM response before being inputted into the regular trigger of AMANDA-B10. This ensures that the return pulses induced by the laser arrives within the time window set for the read out of ADC and TDC buffers.

From the 1998-99 season onward the output of the discriminator in Fig. A.6 was also routed into a channel not in use (channel 44 in 1998-99) so that the initial trigger time could be read out as a reference (in fact the delayed time is inputted as well into the same same channel through an OR logic). These times were recorded as a precautionary measure, possible time drifts in the delay unit

can easily be detected this way.

In 1997-98 the DAQ interface consisted of a display of the array showing every one hundred hit with the colour and size of the OMs indicating LE and ADC values. The intensity of the light sent down to the OM through the optical fibre was regulated by inserting Neutral Density (ND) filters in the beam path before the fibre coupler. To get the right intensity it was necessary to estimate the one photoelectron (pe) level of the illuminated OM from the display by eye. In 1997-98 each main DAQ calibration run consisted of two minutes of data taking at one pe, then one minute at a medium level and ending with around 20 seconds at a high intensity. In this fashion the whole ADC range was covered (see the top plot labeled SPE peak in Fig. A.8) in as short a runtime as possible as the laser was only running at around a hundred Hz due to DAQ limitations.

With the new DAQ installed at the end of the 1997-98 season it was possible in 1998-99 to do the light level estimation in a better way. For a background run taken just before the array was taken off-line a Gaussian was fitted to the one photoelectron peak for each functioning OM. The new interface allowed for the on-line viewing of the ADC histogram for the OM being calibrated and therefore the process of adjusting the neutral density filters to get the desired output level for the calibration run could be performed in a quicker and a more accurate manor. After short test runs to get the right intensity so that the ADC spectrum lined up with the one pe peak value, data was taken for a couple of minutes with the laser running at around one kHz. In some cases the light intensity had to be increased toward the end of the run to get enough statistics over the whole ADC range of interest.

String 1-4 are coaxial cables while strings 5-10 are twisted quad cables. The twisted pair design, with the two conducting lines of channels wrapped around each other, allows more OMs per string. In AMANDA the lines of two OMs are combined into quads and they are susceptible to cross-talk, a signal from one channel inducing a signal the other (also occurs between quads). For calibration runs this meant having to turn off the HV for odd/even OMs when taking $T0$ data on strings 5-10 otherwise cross-talk would ruin the data.

The photomultiplier pulse has propagated up nearly two kilometres of electrical cable when it is measured in the surface electronics and has thereby not only been delayed but also been distorted. If the original PMT pulse have a width of 20 ns and an amplitude of 2.5 V it will have a width of 400 ns and an amplitude of 2.5 mV when it arrives at the DAQ. The arrival time of the pulse is determined by a discriminator threshold setting for the TDC and the pulse deformation therefore leads to a time walk for low amplitude signals. This finite rise-time problem also has to be corrected for.

The correction for the pulse propagation in the cable was found by fitting the

LE time versus the ADC value to get the LE time of an infinite pulse. Looking at data from a typical 1998-99 season calibration run in Fig. A.7 it is clear that by fitting a straight line in LE versus the inverse of the square root of the ADC the objective could be met (see top left corner plot in Fig. A.9 for the actual fit).

This gives the two parameter correction

$$\mathrm{LE}_{corrected} = \mathrm{LE}_{raw} - t_0 - \frac{\alpha}{\sqrt{\mathrm{ADC}}} \tag{A.3}$$

which takes care of both the delay (by t_0) and the deformation of the pulse (by the α component).

The 1997-98 calibration data was taken with different laser intensities to cover the whole range of the ADC spectrum, first very roughly around the one photoelectron (pe) level (ADC $\sim 100 - 150$) and then at a few higher levels to get enough statistics up to and around ADC ~ 2000. In 1998-99 a fixed intensity was used for each run, chosen to match the one pe level for each OM (as extracted from unfiltered data collected just before the detector was taken off-line for calibration and maintenance).

Due to a problem with the timing calibration data in the previous season two separate sets of data were taken in 1997-98 with the timing DAQ, a stand alone DAQ system, and also for the first time the main DAQ. The timing DAQ data was used to get the ΔLE mentioned in the previous section while the main DAQ data (cross checked with the other data) was used to get the set of t_0s.

Up to and including the 1997-98 season the LE for an infinite pulse, $T0$ in Fig. A.8, was used to calculate the t_0. To improve the timing calibration for the odd numbered OMs on strings 5-10, which are almost ten metres away from the light source, the fitted peak value of the $\mathrm{LE}_{corrected}$ distribution started being used instead in the 1998-99 season. This is illustrated in the left plot in the middle row in Fig. A.9. Fitting a Gaussian to the rising edge of that distribution excludes the contribution of scattered photons seen as the tail on the right side. The 4 ns time difference in that plot is about the average value.

Before the 1997-98 season the line fitting in the LE vs $1/\sqrt{\mathrm{ADC}}$ profile plot was done over the whole range. This is fine for strings 1-4 where the data is almost perfectly linear. For strings 5-10 it turned out not to be the case although the data is linear in the region of interest (low pe:s). So a switch was made so that the fit was only performed over $100 \leq \mathrm{ADC} \leq 300$. In 1998-99 the information about the one pe level for each OM was used better and the fits were made in the range $(\mathrm{ADC}_{1pe} - 50) \leq \mathrm{ADC} \leq (\mathrm{ADC}_{1pe} + 250)$.

The measured LE consists of several parts (see Fig. A.6)

$$\mathrm{LE}_{corrected} = t_{transit} + t_{ice} + t_{pmt} + t_{cable} + t_{electronics} \tag{A.4}$$

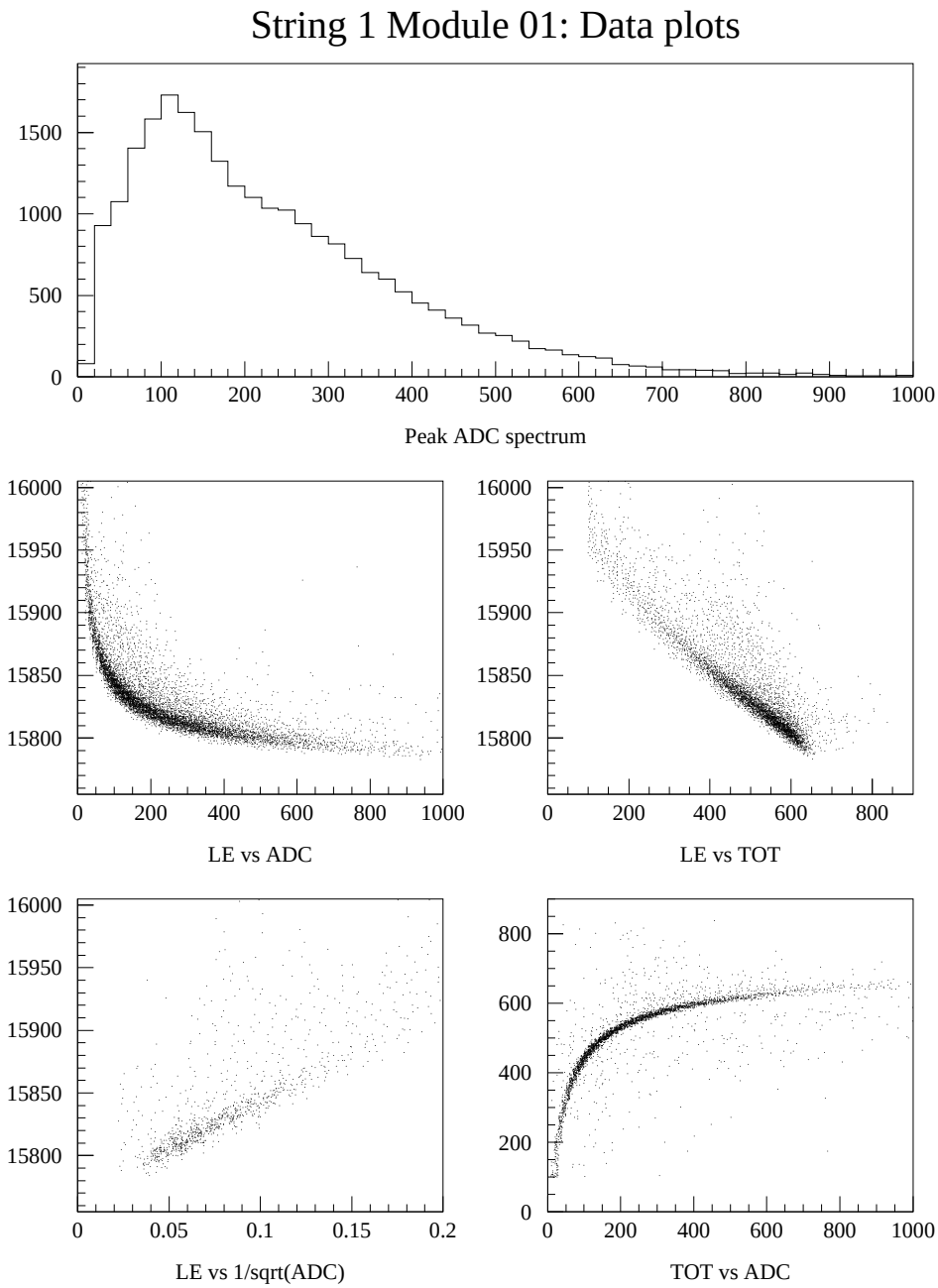

Figure A.7: The data plots of a calibration run for module one on string one from the 1998-99 season. Top plot is the one pe ADC spectrum. Lower left plot shows the linearity of LE vs $1/\sqrt{\mathrm{ADC}}$.

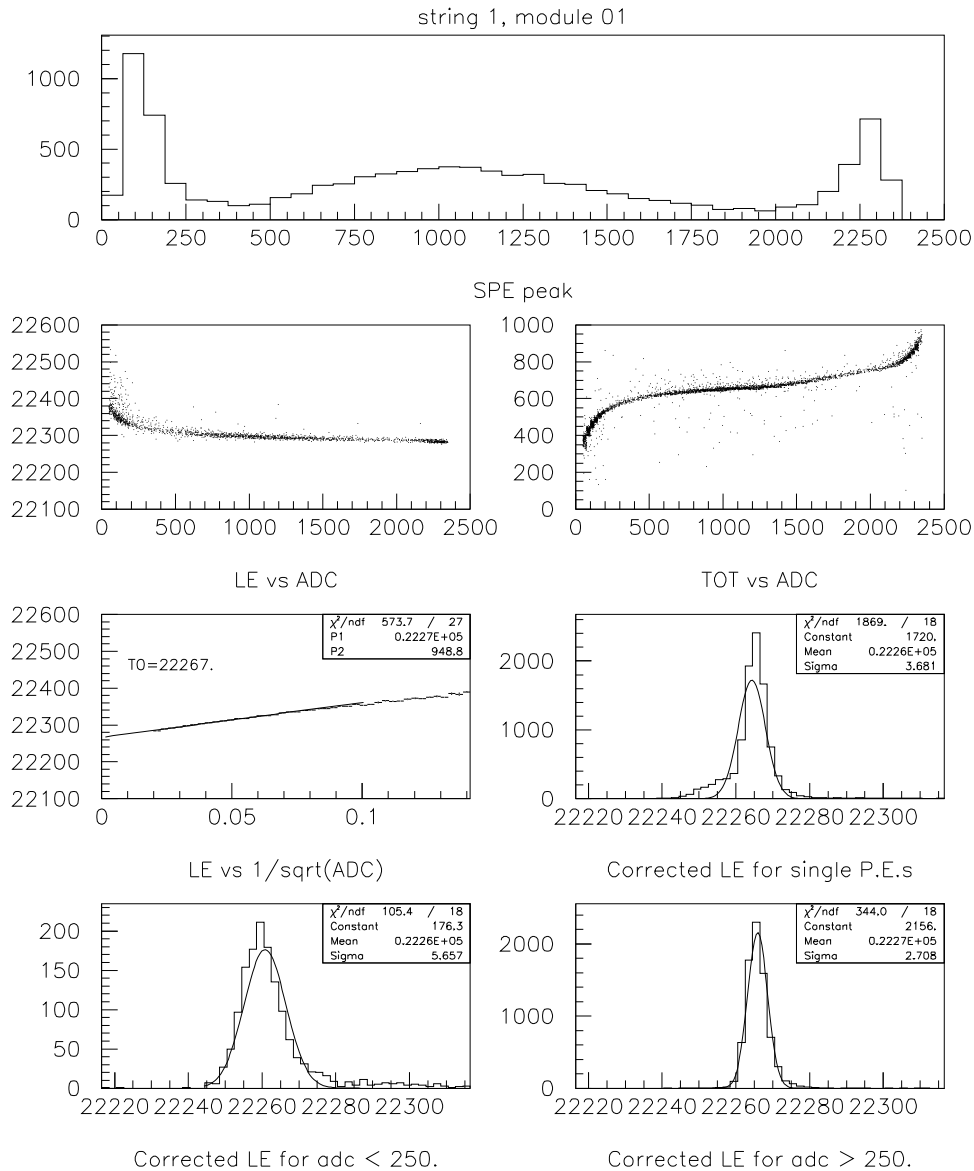

Figure A.8: $T0$ fit in 1997-98. Top plot shows the ADC spectrum of the run, three different laser intensities was used. The fit is done on the profile plot of LE vs $1/\sqrt{\text{ADC}}$ on the left in the third row. At the bottom are plots of the LE data corrected with the fit parameters $T0$ and α through equation A.3.

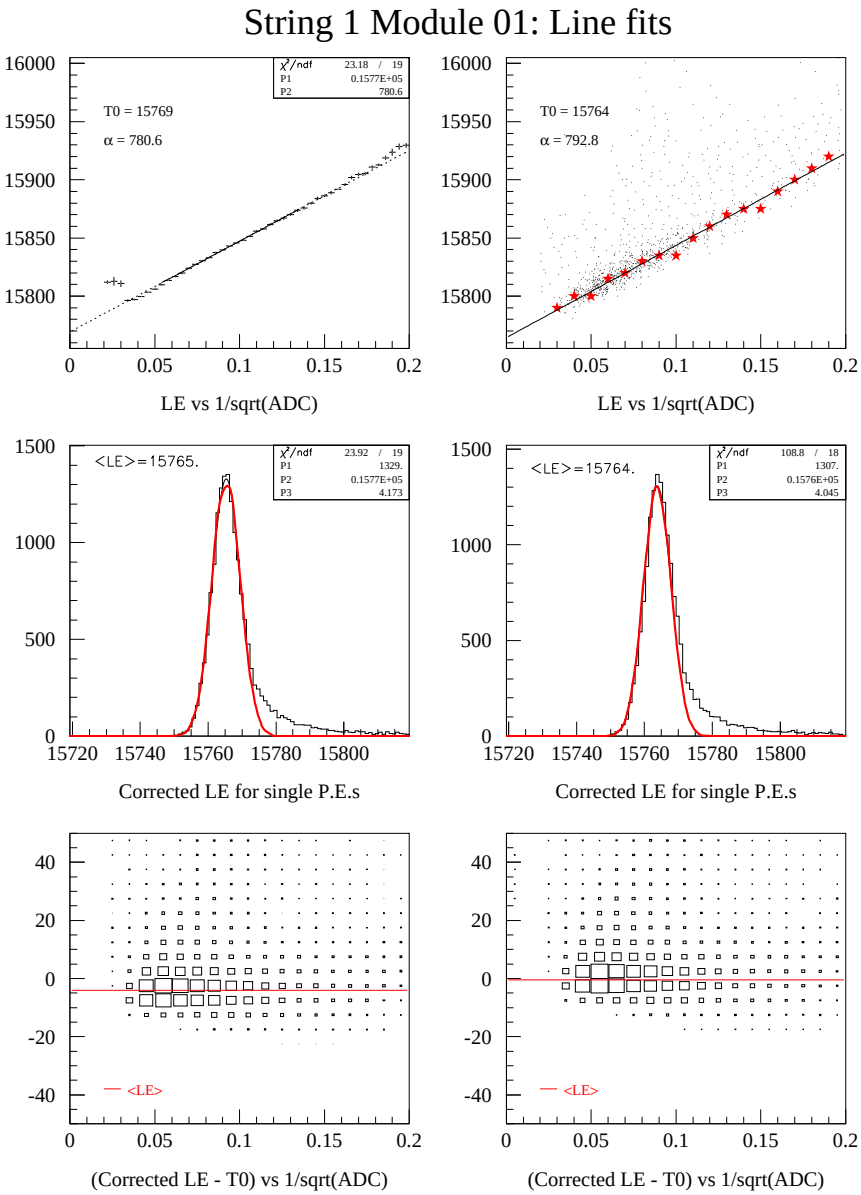

Figure A.9: $T0$ fit in 1998-99. The corresponding data plots are shown in A.7. The three plots in the left column are the actual fit on a profile plot of the data (top), the distribution of LE data corrected through equation A.3 (middle) and a lego plot of the corrected and shifted LE data vs $1/\sqrt{\text{ADC}}$ (bottom).

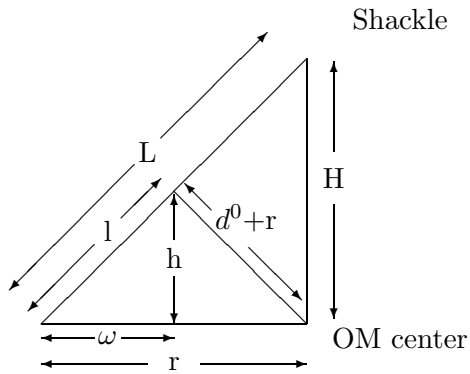

Figure A.10: A schematic plot of the geometry of the top quadrant of the OM defining the quantities used for the fibre ball distance correction.

where $t_{transit}$ is the optical fibre transit time for the laser pulses, t_{ice} is the propagation time from the fibre to the PMT, t_{pmt} is the PMT transit time (dependent on the high voltage), t_{cable} is the time it takes the PMT signal to travel up the electric cable and $t_{electronics}$ is the time required for the signal to be processed up in the surface electronics.

The next step in the analysis chain is to subtract $t_{transit}$ and t_{ice} from the corrected mean LE time. In 1997-98 the t_{ice} term was calculated with the assumption that the diffusing nylon ball was located 0.3 m from the OMs on string 1-4 where there is a SM and MM fibre ending next to each OM. Exception is of course made in the cases of non-working fibres where the closest working fibre is a certain distance away (e.g. on string 1, OM nr 14 has its closest working fibre end ten metres away). For strings 5-10 there are only optical fibres to every second OM but the OMs are only ten metres apart (unlike stings 1-4 where they are 20 m apart). The fibre balls on these strings were therefore assumed to be either 0.5 m away or 9.5 m depending on which OM in the pair that was being calibrated. Again further distance is added if a certain fibre is not working and the another fibre had to be used.

In the 1998-99 analysis a more detailed approach was introduced. Each even numbered module have a fibre ball located at a radial distance d^0 from the surface of the OM, as illustrated here (Fig. A.10) in a schematic of the geometry of the

top quadrant of the OM in Fig. 3.3. The supporting steel wire with length L is attached on the harness at the side of the OM and in a shackle at height H above the centre of the OM. The measured quantity for the fibre ball is the height h from the centre of the harness around the equator of the OM. If α denotes the angle between L and the radius r then $\tan(\alpha) = h/\omega$ and $\cos(\alpha) = r/L$. The distance between the OM and the fibre ball is given as

$$d = \sqrt{h^2 + \left(r - \frac{|h|}{\tan(\arccos(\frac{r}{L}))}\right)^2} - r \tag{A.5}$$

where the numbers for the radius of the OM is 15 cm and for the length of the steel wire 1.2 m. For the odd numbered modules (or any OM not immediately next to the fibre ball) the distance is given by

$$d = \sqrt{(z_1 - z_2 - h)^2 + \left(r - \frac{|h|}{\tan(\arccos(\frac{r}{L}))}\right)^2} - r \tag{A.6}$$

where z_1 is the z coordinate of the odd OM (or the OM being calibrated) and z_2 of the even OM (or the OM next to the fibre ball).

A further complication with using the fitted mean of the corrected LE distribution is that a scattering correction must be used since the scattering in the ice not only give rise to the tail in the distribution but will also shift the whole thing toward later times. Monte Carlo simulations of light propagation in ice [154] yielded the results of Fig. A.11. This is also put into the ice propagation time so that

$$t_{ice} = \frac{d}{c_{ice}} + t_{scattering}(d) \tag{A.7}$$

where d is the distance between the fibre ball and the OM and $t_{scattering}(d)$ as shown in Fig. A.11. Although the OMs in AMANDA-B10 have been painted on top to make the upper hemisphere non-transparent, some of the even numbered OMs on strings 5-10 have a little window on top that allows direct light from the fibre ball when it is mounted above the OM. In those cases the $t_{scattering}$ formula used is that for a source below the OM.

One problem that was discovered by using two separate data sets was a 60 ns shift for a group of OMs. This was explained by an inverted common stop signal to a TDC unit in the main DAQ (starting with OM 13 on string 9 down to OM 6 on string 10). As this inversion therefore also was present in the data no correction for it was applied to the t_0:s. In the 1998-99 season calibration data it became evident that two more common stop pulses had been inverted (covering string 5 and most of string 6). In the raw LE times in the 1998 data this could not be seen and therefore a correction for it was introduced in the final 98 t_0:s.

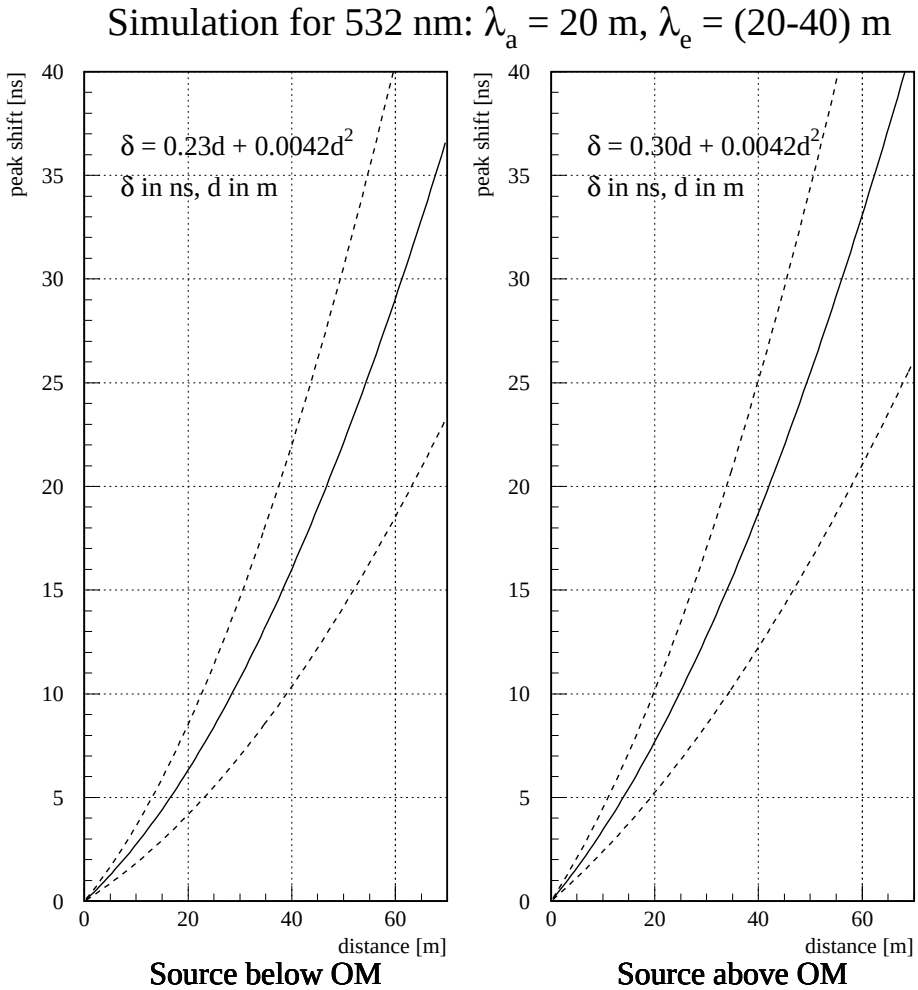

Figure A.11: The scattering correction needed since the fitted mean of the corrected LE distribution is used instead of $T0$. An isotropic source is assumed, left is the source placed below the OM and right above. The dashed curves correspond to the extreme cases of the effective scattering length in the ice $\lambda_{eff} = 20$ m and $\lambda_{eff} = 40$ m. The solid curves are what have been used in the t_0 calculation.

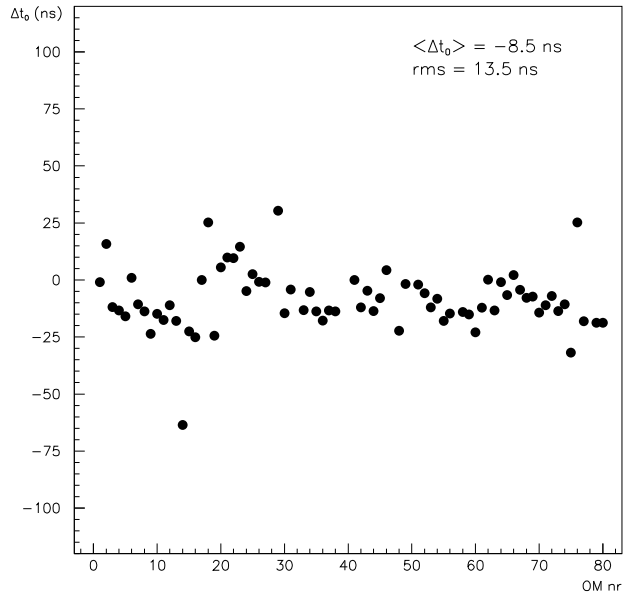

Figure A.12: The difference in t_0 values for 1996 and 1997.

The last step in the analysis is to calculate the relative t_0:s where one OM has been chosen as zero point. For the 1995, 1996 and 1997 t_0:s the top module on string 3 had been used. From a calibration point of view this turned out not to be a perfect OM in the long run as the t_0 for it changed over the years when the fitting method changed slightly. So from 1998-99 onward module 18 on string 6 was chosen as anchor. That OM has a very stable t_0 and the value it had in 1997-98 (1795 ns) is now fixed so that all t_0:s are relative to that value.

The final t_0:s are then calculated as

$$t_0 =< \mathrm{LE}_{corrected} > -t_{ice} - t_{transit} - T0_{s6m18} + 1795 \tag{A.8}$$

where all the times are in nanoseconds and $T0_{s6m18}$ is the $T0$ of module 18 on string 6. This can be compared with

$$t_0 = T0 - t_{ice} - t_{transit} - T0_{s3m1} \tag{A.9}$$

which were used for the 1997 t_0:s.

A comparison of the the 1997 t_0-results with measurements done after the deployment of the first four strings in 1996 is shown in Fig. A.12 and the comparison between 1997 and 1998 for the whole AMANDA-B10 array in Fig. A.13.

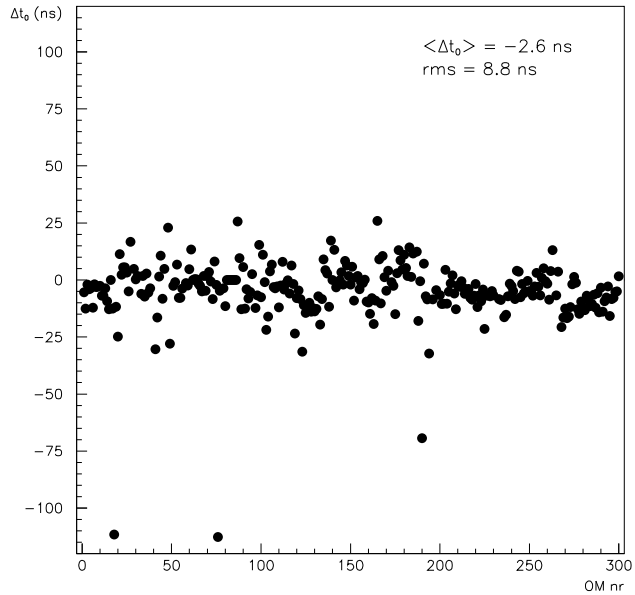

Figure A.13: The difference in t_0 values for 1997 and 1998.

The two OMs that deviate the most (located around -110ns) are module 19 on string 1 (OM nr 19) and module 16 on string 4 (OM nr 76). The big difference for the latter is due to the fact that the amplification on that OM is too large and the fit in the previous years were performed over the wrong ADC range.

Some problems encountered during the analysis were SM/MM mix-ups (or misassignments) during data taking. This could be resolved by comparing t_0 differences with fibre transit time differences. Swapped quads was another problem as some connectors had been wrongly . Wrong fibre transit times for a few OMs of a special class was also found. These were MM fibres 14, 16, and 18 on string 7 that end up inside hybrid OMs since they were designed to also be used for optical read out of modules 28, 32 and 36 (OM nr 186, 190 and 194 respectively). Inside these OMs some extra fibre were coiled up, 7.7 metres (38.6 ns) for MM 14 and 32.9 metres (165ns) for MM 16 and 18.

Appendix B

Filter Specifics

B.1 Filter Level Two

A "standard" hit cleaning have been established for AMANDA-B10 analysis. It consists of six demands on the hits that are used for the reconstruction of an event. The first requirement is that only hits inside a time window of 4500 ns around the event are to be used, the starting time of this window is 19000 ns into the event in all three years included in this work. Hits with too large or too low amplitudes are also excluded, the calibrated amplitude needs to be in the range from 0.3 to 1000 photoelectrons. To get rid of a part of the cross talk a TOT cut is implemented, $125 < \mathrm{TOT} < 2000$, since many cross talk pulses have short pulse widths. The fourth criterion is that only the first pulse in each channel is used. Hits that are isolated from the others by at least 70 m in radius or 500 ns in time are also rejected from use in the reconstruction. A sixth demand is the exclusion of hits from "bad OMs", channels that are known to be misbehaving or dead.

B.1.1 1997

In the 1997 filtering a line fit is calculated for the events and then a zenith cut $> 50^\circ$ is applied to the result. The events that pass this level one filter are reconstructed with a maximum likelihood reconstruction. The level two filtering is a cut on the reconstructed zenith angle of the likelihood fit $> 80^\circ$ followed by a cut that requires that the likelihood fit has three or more hits with time residuals in the interval from -10 ns to 25 ns. The RECOOS flags used in the 1997 level two filtering are shown in Table B.2.

Bad OM list used in the 1997 level two filtering
28, 32, 39, 40, 47, 49, 50, 57, 62, 78-80, 83-86, 96, 143, 167, 172, 186, 190, 195, 197, 199, 215, 227, 231-235, 252, 255, 259, 260, 261, 267

Table B.1: The list of optical modules that are excluded from use in the reconstruction on filter level one and two for 1997 data.

Nr	Reconstruction	RECOOS Flags
1	Line fit	-r n -i m -p w=0. -X g=f -i m -p n=300:4500 -p j=15 -p a=96. -p t=1:5 -X o=2 -y R=0.:4500. -y I=70.:500.:1 -y a=0.3:1000. -y b=125:2000. -y A=1
2	Muon LH	-r m -i f -p f=1 -X g=f -m p -z a_upandel -x x,y,z,zenith,azimuth -p n=300:4500 -p j=15 -p a=96. -p t=1:5 -X o=2 -y R=0.:4500. -y I=70.:500.:1 -y a=0.3:1000. -y b=125:2000. -y A=1

Table B.2: The reconstructions performed at filter level one and two for 1997, in addition to these flags the list of excluded OMs in Table B.1 is also used.

B.1.2 1998

In the 1998 filtering the hits from four extremely noisy channels (OMs 40, 190, 234, 258) are removed from the data stream before the level one filtering. The 1998 data was filtered twice since some erroneous calibration values for OMs on strings 11-13 were used in first filter pass. The first filtering also included some hits on strings 11-13 in the reconstruction. Three first guess algorithms were used and a cut is done on the zenith angle of the line fit $> 70°$. A muon and a cascade likelihood fit were performed in the level one filtering but not cut upon.

After un- and recalibrating the data that passed the previous level one filtering it was reconstructed again using only hits on the first ten strings of the detector. Three first guesses and were followed by a $> 70°$ cut on the zenith angle of the new line fit. The events that passed got a new muon and a new SPE cascade likelihood reconstruction as outline in Table B.4.

The level two filter cuts for the 1998 data are the same as in the 1997 filtering. However, there is one very important difference. The reconstruction variables that where used did not belong to the final muon likelihood reconstruction. Instead it was the reconstructed muon from the first iteration that had the demand that the zenith angle $> 80°$ and three direct hits in the time residual interval from -10 ns to 25 ns. Since this muon reconstruction had been performed using hits from strings 11-13 which had been wrongly calibrated the effect is a drop in efficiency

Iteration	Bad OM list used in the 1998 level two filtering
1	3, 18, 28, 32, 34, 39-42, 47, 50, 57, 61, 62, 74, 75, 78, 81-86, 94, 96, 117, 143, 167, 172, 186, 188-190, 194, 195, 197-199, 201, 215, 216, 224, 225, 227, 234, 235, 249, 258, 263, 264, 267, 280, 290, 303-310, 336-355, 361, 364, 366, 379-394, 399-401, 408, 410, 412, 413, 415-419, 421-428
2	3, 18, 28, 32, 34, 39-42, 47, 50, 57, 61, 62, 74, 75, 78, 81-86, 94, 96, 117, 143, 167, 172, 186, 188-190, 194, 195, 197-199, 201, 215, 216, 224, 225, 227, 234, 235, 249, 258, 263, 264, 267, 280, 290, 303-428

Table B.3: The list of optical modules that are excluded from use in the reconstruction in the first iteration of filter level one for 1998 data and the second iteration of the level one and level two.

Nr	Reconstruction	RECOOS Flags
1	First guess	-y R=0.:4500. -y a=0.3:1000. -y b=125:2000:1:302 -y I=70.:500.:1 -y A=1 -r n -i a -X g=f -p w=0. -X s=n -p t=0:10 -p n=300:4500 -p j=15 -p a=96. -X o=2
2	Muon LH	-y R=0.:4500. -y a=0.3:1000. -y b=125:2000:1:302 -y I=70.:500.:1 -y A=1 -r m -i f -p f=2 -X g=f -m p -X s=o -z a_upandel -x x,y,z,zenith,azimuth -p t=0:0 -p n=300:4500 -p j=15 -p a=96. -X o=2
3	SPE Cascade	-y R=0.:4500. -y a=0.3:1000. -y b=125:2000:1:302 -y I=70.:500.:1 -y A=1 -r m -i f -p f=3 -X g=n -m p -X s=n -z a_pp_upandel -l xyzt -x x,y,z,time -p p=1003 -p t=0:0 -p n=300:4500 -p j=15 -p a=96. -X o=2
4	First guess	-y R=0.:4500. -y a=0.3:1000. -y b=125:2000:1:302 -y A=1 -y I=70.:500.:1 -r n -i a -X g=f -p w=0. -X s=n -p t=0:10 -p n=1000:4500 -p j=15 -p a=96. -X o=2
5	Muon LH	-y R=0.:4500. -y a=0.3:1000. -y b=125:2000:1:302 -y A=1 -y I=70.:500.:1 -r m -i f -p f=7 -X g=n -m x -X s=o -z a_upandel -x x:step=10,y:step=10,z:step=10, zenith:step=0.1,azimuth:step=0.25 -p t=0:0 -p n=1000:4500 -p j=15 -p a=96. -X o=2
6	SPE Cascade	-y R=0.:4500. -y a=0.3:1000. -y b=125:2000:1:302 -y A=1 -y I=70.:500.:1 -r m -i f -p f=8 -X g=n -m x -X s=n -z a_pp_upandel -l xyzt -x x:step=10,y:step=10, z:step=10,time:step=25 -p p=1003 -p t=0:0 -p n=1000:4500 -p j=15 -p a=96. -X o=2

Table B.4: The reconstructions performed at filter level one and two for 1998, nr 1-3 is the first iteration and nr 4-6 the second iteration. The list of excluded OMs in Table B.3 is used for the respective iteration.

Bad OM list used in the 1999 level two filtering
3, 18, 28, 32, 39, 40, 44, 47, 50, 57, 61, 62, 78, 81-86, 94, 96, 117, 143, 167, 172, 186, 190, 195, 197, 199, 215, 216, 227, 231, 232, 235, 243, 244, 262, 265, 267, 303-428

Table B.5: The list of optical modules that are excluded from use in the reconstruction on filter level one and two for 1999 data.

Nr	Reconstruction	RECOOS Flags
1	First guess	-y R=0.:4500. -y a=0.3:1000. -y b=125:2000:1:302 -y A=1 -y I=70.:500.:1 -r n -i a -X g=f -p w=0. -X s=n -p t=0:10 -p n=1000:4500 -p j=15 -p a=96. -X o=2
2	Muon LH	-y R=0.:4500. -y a=0.3:1000. -y b=125:2000:1:302 -y A=1 -y I=70.:500.:1 -r m -i f -p f=2 -X g=n -m x -X s=o -z a_upandel -x x:step=10,y:step=10,z:step=10, zenith:step=0.1,azimuth:step=0.25 -p t=0:0 -p n=1000:4500 -p j=15 -p a=96. -X o=2
3	SPE Cascade	-y R=0.:4500. -y a=0.3:1000. -y b=125:2000:1:302 -y A=1 -y I=70.:500.:1 -r m -i f -p f=3 -X g=n -m x -X s=n -z a_pp_upandel -l xyzt -x x:step=10,y:step=10, z:step=10,time:step=25 -p p=1003 -p t=0:0 -p n=1000:4500 -p j=15 -p a=96. -X o=2

Table B.6: The reconstructions performed at filter level one and two for 1999, in addition to these flags the list of excluded OMs in Table B.5 is also used.

for atmospheric neutrino induced events.

B.1.3 1999

During detector maintenance some cables were swapped before the 1999 data taking season, this meant that a few TDC and ADC channels in the data stream were misassigned. After this was discovered a solution of remapping the channels before calibration was implemented.

Filter level one consists of three first guesses with a cut on the zenith angle of the line fit $> 70°$. After a muon and a SPE cascade likelihood reconstruction the level two filtering demands $> 80°$ for the zenith angle of the muon fit and that it has three direct hits with time residuals in the interval from -10 ns to 25 ns. The 1999 level two filtering is detailed in Table B.6.

Year	Bad run list
1997	508, 510, 511, 523, 525, 529, 534, 539, 543, 544, 546, 548, 551-553, 555, 560, 561, 571, 575, 586-588, 592, 595, 598-600, 602, 605, 607, 612, 618, 619, 627, 634, 635, 641, 647-649, 651, 659-662, 674, 678, 710, 711, 723, 737, 762-775, 786-789, 796, 798, 806, 809, 816, 820-828, 833-853, 857, 860, 863-874, 885, 890, 912-915, 918, 919, 929, 932, 938, 940, 941, 958, 966, 967-1002, 1004, 1010, 1011, 1014, 1021, 1023, 1024, 1027, 1030, 1036, 1045, 1053, 1054, 1057, 1060, 1077, 1081-1085, 1087, 1107, 1109, 1110, 1114, 1116
1998	60-63, 74, 88-125, 143, 145-147, 232, 239, 240, 304, 306-308, 347, 349, 351, 352, 366, 369, 376, 451-455, 535, 577, 578-580, 655, 670, 674, 677, 688, 723, 731, 732, 735-740, 742, 744, 747-756, 784, 789-796, 799, 804-809, 812, 814-817, 820-835, 839-843, 845-848, 850-875
1999	1-7, 16, 17, 21-30, 33, 35, 39-47, 67, 69, 71, 73-91, 102, 106, 108, 109, 111, 112, 116, 149-157, 243, 251, 276, 291, 326, 345, 346, 379, 389, 412-426, 428, 494-511, 517-521, 531, 549, 685-700

Table B.7: The list of runs that are excluded from level three and onward in the analysis for each of the three years 1997-99.

B.2 Filter Level Three

At filter level three the runs that have been identified as bad in some form are skipped and only events in good runs are processed further, the excluded runs are listed in Table B.7.

The flare events are removed from the data stream, the data is uncalibrated and cross talk cleaned with *xt-filt*. After recalibrating the data some extra channels ($channelnumber > 428$) are purged from the data stream.

The standard reconstruction hit cleaning as defined for filter level two is used at level three as well but with the addition of a higher TOT cut for hybrid OMs, $200 < \text{TOT} < 2000$ for OMs 87, 89, 91, 93, 95, 97, 123, 125, 127, 129, 131, 133, 190, 194, 195, 197, 199, 201, 203, 205, 231, 232 and 235.

The first new reconstruction on level three is a tensor of inertia fit as the centre of gravity parameter will be used in the neural networks at filter level four. For the muon track reconstruction the new first guess is a direct walk fit which is used as input to a Bayesian muon reconstruction. The filtering on level three is a zenith cut on the Bayesian reconstruction removing all downgoing events ($> 90°$) and events with less than three direct hits with time residuals in the interval from -10 ns to 25 ns. Finally, cascade reconstructions are performed for use in the next filter level. A plane wave first guess is used as starting point for a SPE cascade likelihood reconstruction. This in turn is used as input to a MPE cascade

Run	Bad OM list
All	28, 32, 34, 39, 40, 47, 49, 50, 57, 62, 78, 83-86, 96, 143, 167, 172, 186, 190, 195, 197, 199, 215, 227, 231-235, 252, 255, 259-261, 267, 289, 290
500-544	79, 80
545-760, 762-770	79, 80, 263
761	35, 79, 80, 263
771-773	80, 263
774-824	263
1093-1116	18

Table B.8: The list of optical modules that are excluded from level three and onward in the analysis of 1997 data.

Run	Bad OM list
All	18, 28, 32, 34, 36, 39-42, 47, 50, 57, 61, 62, 78, 81-86, 96, 143, 167, 172, 186, 189, 190, 195-199, 201, 215, 227, 229, 231, 232, 235, 249, 258, 263, 264, 267, 303-428
60-99	21, 185, 302
100-119	21, 302
119-144	21
145-225	3, 21
226-359	3, 21, 234
360-451	3, 234
452-537	3, 234, 280, 290
538-651	3, 94, 117, 234, 280, 290
652-709	3, 94, 117, 224, 225, 234, 280, 290
710-876	3, 94, 117, 224, 225

Table B.9: The list of optical modules that are excluded from level three and onward in the analysis of 1998 data.

Run	Bad OM list
All	3, 18, 28, 32, 36, 39-42, 44, 47, 50, 57, 61, 62, 78, 81-86, 94, 96, 117, 143, 167, 169, 172, 186, 189, 190, 195, 197, 199, 215, 216, 227, 229, 231-235, 243, 244, 259-262, 265, 267, 289, 290, 303-428
11	254, 264
97	16
160-162	234, 249, 258
215-224, 661, 664, 667-670, 678, 682, 683	302
308, 477	263
450	198, 263
477	263
674	277
675, 676	277, 289

Table B.10: The list of optical modules that are excluded from level three and onward in the analysis of 1999 data.

reconstruction. The details of the reconstructions on level three are presented in Table B.11 and the list of OMs that are excluded in the reconstruction for each of the three years is given in Table B.8 (1997), Table B.9 (1998) and Table B.10 (1999).

B.3 Filter Level Four

Filter level four is where the filtering of data diverges into twelve different analyses through the different signal samples used in the training of the neural networks. The cut values used for each neural network in given in Table B.12.

B.4 Filter Level Five

A harder time isolation hit cleaning is implemented on level five. It is similar to the time isolation cut in the standard hit cleaning but instead of single hits it excludes hits that come in pairs or triplets more than 500 ns before or after the other hits in the event. The events are then reconstructed again with a new direct walk first guess used as input for a new Bayesian likelihood muon track

Nr	Reconstruction	RECOOS Flags
1	Tensor of Inertia	-y u=6 -v -r n -i i -X g=f -p w=0. -X s=n
2	Direct Walk	-y u=6 -v -r n -i s -X g=n -X s=n
3	Muon, Bayesian	-y u=6 -v -r m -i f -X g=f -m p -z a_upandel+a_zwght2 -x x,y,z,zenith,azimuth -p n=1000:4500 -p j=15 -p a=96. -p t=1:5 -X o=2
4	Plane Wave	-y u=6 -v -r n -i q -X g=f -p w=0. -X s=n
5	SPE Cascade	-y u=6 -v -r m -i f -X g=f -p m=0 -X s=n -m x -z a_pp_upandel -lxyzt -x x:step=5,y:step=5,z:step=5,time:step=20 -p p=1003 -p t=0:0 -p n=1000:4500 -p j=15 -p a=96. -X o=2
6	MPE Cascade	-y u=6 -v -r m -i f -X g=f -p m=0 -X s=n -m x -z a_upandel_ps_mpe -lxyzt -x x:step=5,y:step=5,z:step=5,time:step=20 -p p=1003 -p t=0:0 -p n=1000:4500 -p j=15 -p a=96. -X o=2

Table B.11: The reconstructions performed at filter level three for 1997. These are also applied for 1998 and 1999 with the change of the user line with the hits that pass the cross talk cleaning from -y u=6 to 8 and 9 respectively due to the change in the number of reconstructed tracks in the level two filtering. Additionally, the list of OMs that are excluded in the reconstruction for each year is given in Table B.8 (1997), Table B.9 (1998) and Table B.10 (1999).

	The neural network cut value					
	Hard annihilation channels			Soft annihilation channels		
M_χ (GeV/c^2)	1997	1998	1999	1997	1998	1999
100	0.935	0.925	0.955	0.910	0.880	0.935
250	0.915	0.950	0.955	0.890	0.955	0.945
500	0.915	0.900	0.945	0.930	0.965	0.910
1000	0.895	0.955	0.955	0.885	0.915	0.935
3000	0.900	0.970	0.960	0.890	0.920	0.935
5000	0.900	0.860	0.975	0.885	0.915	0.920

Table B.12: The neural network cut values used in filter level four for all the analyses 1997-99.

Nr	Reconstruction	RECOOS Flags
1	Direct Walk	-y u=7 -v -r n -i s -X g=n -X s=n
2	Muon, Bayesian	-y u=7 -v -r m -i f -X g=f -m p -z a_upandel+a_zwght2 -x x,y,z,zenith,azimuth -p n=1000:4500 -p j=15 -p a=96. -p t=1:5 -X o=2

Table B.13: The reconstructions performed at filter level five for 1997. These are also applied for 1998 and 1999 with the change of the user line with the hits that pass the new isolation cleaning from -y u=7 to 9 and 11 respectively. Additionally, the list of OMs that are excluded in the reconstruction for each year is given in Table B.8 (1997), Table B.9 (1998) and Table B.10 (1999).

reconstruction with the added hit cleaning of the removal of these isolated pairs and triplets of hits. The details of the RECOOS calls is given in Table B.13.

After the new Bayesian muon reconstruction a cut is made that the zenith angle of this track is greater than 140°, i.e. only upgoing events within a forty degree cone around the vertical axis are kept.

Finally, the main filtering on level five is the application of the cuts specified in Table 7.5.

Appendix C

Cut Optimisation Samples

In order to avoid biasing of the analysis only a subset of the data is used during the optimisation of the cuts on filter levels four and five (filter level six is optimised using simulations alone and does not require any data). The size of the cut optimisation subset is around 20 % of the total size of the data. This subset is later discarded and the final results are calculated using the other 80 % of the data.

Two separate neutralino signal simulation samples have been produced, one is used for the optimisation of cuts on levels four through six while the other is used for the estimation of the signal efficiencies presented throughout this work. The level six cut is optimised with a zenith angle comparison of the reconstructed events in the neutralino signal simulation with those in the atmospheric neutrino simulation. The atmospheric neutrino simulation have therefore been split in two halves, the first is used for the zenith cut optimisation while the second is used to estimate how many muons induced by upgoing atmospheric neutrinos that pass the filter cuts. For the cut optimisation on filter level four and five three sets of atmospheric muons is simulated, the simulated livetime is 30.15 days for the 1997 detector configuration, 63.07 days for 1998 and 73.13 days for 1999.

The level four filtering is performed through the application of a neural network, individually optimised for each neutralino mass and annihilation channel. For each event the values of the selected input variables (varies between the analyses) are used to calculate an output value of the neural network. The networks have been trained with small samples of data and simulated neutralino signal events so that events that are similar to background have output values around zero and events that are signal like have output values around one. The cut applied to the neural network output value on filter level four have been optimised together with the cuts on filter level five and the cut values used in the thirty-six analyses are presented in Table C.1 together with the number of events that pass

Year	Channel	M_χ (GeV/c^2)	NN_{cut}	N_{wimp}	N_{data}	$N_{atm.\mu}$	$N_{atm.\nu}$
		100	0.935	18002	2164	3066	39.4
		250	0.915	26346	954	1640	27.7
	hard	500	0.915	23562	567	1378	27.9
		1000	0.895	24877	396	728	24.3
		3000	0.900	26137	266	332	23.0
1997		5000	0.900	18299	402	449	23.7
		100	0.910	4795	2775	4108	30.1
		250	0.890	7658	2854	3841	42.0
	soft	500	0.930	7334	1596	2395	36.0
		1000	0.885	7833	1568	2483	26.1
		3000	0.890	8068	556	888	26.5
		5000	0.885	5148	703	1484	25.1
		100	0.925	13519	1219	2075	22.2
		250	0.950	17146	320	602	18.2
	hard	500	0.900	15642	389	745	15.1
		1000	0.955	15367	90	151	14.1
		3000	0.970	15302	40	49	8.9
1998		5000	0.860	11240	303	357	13.3
		100	0.880	3889	2060	3846	20.9
		250	0.955	5040	1178	2184	13.2
	soft	500	0.965	4710	480	919	12.7
		1000	0.915	5233	631	1255	16.1
		3000	0.920	5043	265	415	12.4
		5000	0.915	3261	377	518	17.2
		100	0.955	11812	585	791	29.5
		250	0.955	22053	386	451	33.8
	hard	500	0.945	20514	239	289	28.2
		1000	0.955	22359	212	227	27.8
		3000	0.960	23827	259	317	24.9
1999		5000	0.975	16114	56	58	21.9
		100	0.935	1974	1165	1341	38.3
		250	0.945	5212	675	845	33.0
	soft	500	0.910	6026	1118	1365	34.8
		1000	0.935	6673	418	591	30.7
		3000	0.935	7059	226	342	34.3
		5000	0.920	4695	222	227	30.6

Table C.1: The number of events of the cut optimisation sample of data and the signal and background simulations that remain after the level four cut NN_{cut} for all the analyses 1997-99.

the level four cut.

The level five filtering is aimed at removing all remaining misreconstructed downgoing atmospheric muons. The variables that are used are listed in Table 7.4 and the cuts in Table 7.5. The number of events that pass filter level five for the cut optimisation samples of data, the neutralino signal and the atmospheric neutrino simulations is shown in Table C.2. No events in the simulated atmospheric muon samples used for the cut optimisation pass the level five filter.

The zenith angle cut on the Bayesian reconstructed muon track at filter level six is optimised for two different livetimes. The cut is optimised both for the individual years and their respective livetimes as well as the combined livetime of all three years. Only the latter is used in the calculation of the final results but before unblinding of the analysis the individual optimisations were also performed for the evaluation of the data of each year. The cut value used in the level six filtering and the number of events that pass the cut is presented for each analysis in Table C.3 (individual optimisation) and Table C.4 (combined optimisation). The resulting number of events that pass filter level six for the individual optimisation for the 80 % unblinded data samples and the corresponding livetime for the atmospheric neutrino simulation is presented in Table C.5.

The 90 % confidence level upper limits on the muon flux calculated for the individual optimisation with the cut optimisation samples is given in Table C.6. These values are plotted in Figs. C.1 (1997), C.3 (1998) and C.5 (1999). The limits with the combined optimisation is shown in Fig. C.7. Before unblinding the analyses the sensitivity for each year was estimated by scaling the number of atmospheric neutrino events to the livetime of the 80 % samples and calculating the sensitivity for these extrapolated numbers, these sensitivities are plotted in Figs. C.2 (1997), C.4 (1998) and C.6 (1999).

		Hard annihilation channels			Soft annihilation channels		
Year	M_χ (GeV/c^2)	N_{wimp}	N_{data}	$N_{atm.\nu}$	N_{wimp}	N_{data}	$N_{atm.\nu}$
	100	6973	17	18.9	1088	13	12.5
	250	15760	12	15.8	3315	17	19.6
1997	500	15536	12	15.6	3991	17	18.4
	1000	17041	11	15.2	4731	12	13.8
	3000	18452	11	15.1	5341	12	15.6
	5000	12923	10	14.6	3513	11	15.7
	100	5046	12	10.2	840	9	8.4
	250	9483	11	9.9	2127	6	5.8
1998	500	9025	9	7.7	2436	9	7.1
	1000	9571	10	8.2	2875	11	8.0
	3000	9994	8	5.7	2951	8	6.7
	5000	7029	10	7.6	1989	12	9.0
	100	6016	9	18.4	763	11	22.4
	250	14461	12	21.8	2851	11	20.3
1999	500	14417	9	18.6	3698	8	19.9
	1000	16208	10	19.1	4412	9	19.9
	3000	17609	8	16.6	5003	12	22.5
	5000	12419	8	16.9	3340	9	20.3

Table C.2: The number of events of the cut optimisation sample of data and the signal and background simulations that remain after the level five filter for all the analyses 1997-99.

		Zenith cut optimisation for individual years							
		Hard annihilation channels				Soft annihilation channels			
Year	M_χ	θ_{cut}	N_{wimp}	N_{data}	$N_{atm.\nu}$	θ_{cut}	N_{wimp}	N_{data}	$N_{atm.\nu}$
	100	173.0°	5759	2	1.4	171.5°	959	2	1.6
	250	175.5°	11783	1	0.7	174.0°	2694	1	1.1
1997	500	175.5°	13099	1	0.7	175.5°	3022	1	0.7
	1000	176.5°	13561	0	0.4	175.5°	3839	1	0.7
	3000	177.0°	14543	0	0.3	176.5°	4233	0	0.4
	5000	177.0°	10475	0	0.3	176.5°	2925	0	0.4
	100	172.5°	4240	3	1.3	171.5°	740	4	1.4
	250	175.0°	7665	1	0.5	175.0°	1537	1	0.5
1998	500	176.0°	7114	1	0.4	176.0°	1674	1	0.4
	1000	176.0°	8101	1	0.4	176.0°	2190	1	0.4
	3000	176.5°	8411	1	0.3	176.0°	2445	1	0.4
	5000	176.5°	5993	1	0.3	176.5°	1630	1	0.3
	100	172.5°	5136	0	2.5	172.5°	621	0	2.4
	250	174.5°	12151	0	1.4	174.0°	2332	0	1.6
1999	500	176.0°	11189	0	0.7	174.5°	3114	0	1.4
	1000	176.5°	12688	0	0.6	175.0°	3767	0	1.1
	3000	176.5°	14615	0	0.5	176.5°	3874	0	0.6
	5000	176.5°	10435	0	0.6	176.5°	2690	0	0.6

Table C.3: The results for the cut optimisation samples after the level six cut optimised for ~ 80 % of the individual livetime for each year in 1997-99, M_χ in units of GeV/c^2.

		Zenith cut optimisation for combined years							
		Hard annihilation channels				Soft annihilation channels			
Year	M_χ	θ_{cut}	N_{wimp}	N_{data}	$N_{atm.\nu}$	θ_{cut}	N_{wimp}	N_{data}	$N_{atm.\nu}$
	100	174.0°	5170	1	1.0	173.5°	834	1	1.0
	250	175.5°	11783	1	0.7	175.5°	2238	1	0.7
1997	500	176.5°	11287	0	0.4	175.5°	3022	1	0.7
	1000	177.5°	10914	0	0.2	176.5°	3314	0	0.4
	3000	177.5°	13179	0	0.2	176.5°	4233	0	0.4
	5000	177.5°	9628	0	0.2	177.5°	2431	0	0.2
	100	174.0°	3687	2	0.8	174.0°	607	2	0.8
	250	175.0°	7665	1	0.5	175.0°	1537	1	0.5
1998	500	176.0°	7114	1	0.4	176.0°	1674	1	0.4
	1000	176.5°	7602	1	0.3	176.0°	2190	1	0.4
	3000	176.5°	8411	1	0.3	176.5°	2313	1	0.3
	5000	176.5°	5993	1	0.3	176.5°	1630	1	0.3
	100	173.5°	4734	0	1.9	173.5°	556	0	1.8
	250	174.5°	12151	0	1.4	174.0°	2332	0	1.6
1999	500	176.5°	10275	0	0.6	175.5°	2777	0	1.0
	1000	176.5°	12688	0	0.6	176.5°	3042	0	0.6
	3000	177.5°	12278	0	0.3	176.5°	3874	0	0.6
	5000	177.5°	8887	0	0.3	176.5°	2690	0	0.6

Table C.4: The results for the cut optimisation samples after the level six cut optimised as if the expected background for the combined livetime of 421.92 days came from each year in 1997-99, M_χ in units of GeV/c^2.

		Zenith cut optimisation for individual years							
		Hard annihilation channels				Soft annihilation channels			
Year	M_χ	θ_{cut}	N_{wimp}	N_{data}	$N_{atm.\nu}$	θ_{cut}	N_{wimp}	N_{data}	$N_{atm.\nu}$
	100	173.0°	5759	2	4.7	171.5°	959	3	5.4
	250	175.5°	11783	2	2.3	174.0°	2694	3	3.6
1997	500	175.5°	13099	2	2.2	175.5°	3022	2	2.2
	1000	176.5°	13561	2	1.4	175.5°	3839	2	2.3
	3000	177.0°	14543	1	1.0	176.5°	4233	2	1.4
	5000	177.0°	10475	1	1.0	176.5°	2925	2	1.4
	100	172.5°	4240	1	5.0	171.5°	740	5	5.5
	250	175.0°	7665	1	2.0	175.0°	1537	1	2.0
1998	500	176.0°	7114	1	1.4	176.0°	1674	1	1.4
	1000	176.0°	8101	1	1.3	176.0°	2190	1	1.4
	3000	176.5°	8411	0	1.1	176.0°	2445	1	1.3
	5000	176.5°	5993	0	1.2	176.5°	1630	0	1.2
	100	172.5°	5136	10	9.3	172.5°	621	8	8.9
	250	174.5°	12151	6	5.2	174.0°	2332	9	6.3
1999	500	176.0°	11189	2	2.7	174.5°	3114	6	5.3
	1000	176.5°	12688	1	2.2	175.0°	3767	4	4.3
	3000	176.5°	14615	1	2.0	176.5°	3874	1	2.2
	5000	176.5°	10435	1	2.2	176.5°	2690	1	2.2

Table C.5: The results for the unblinded data samples after the level six cut optimised for $\sim$ 80 % of the individual livetime for each year in 1997-99, M_χ in units of GeV/c^2.

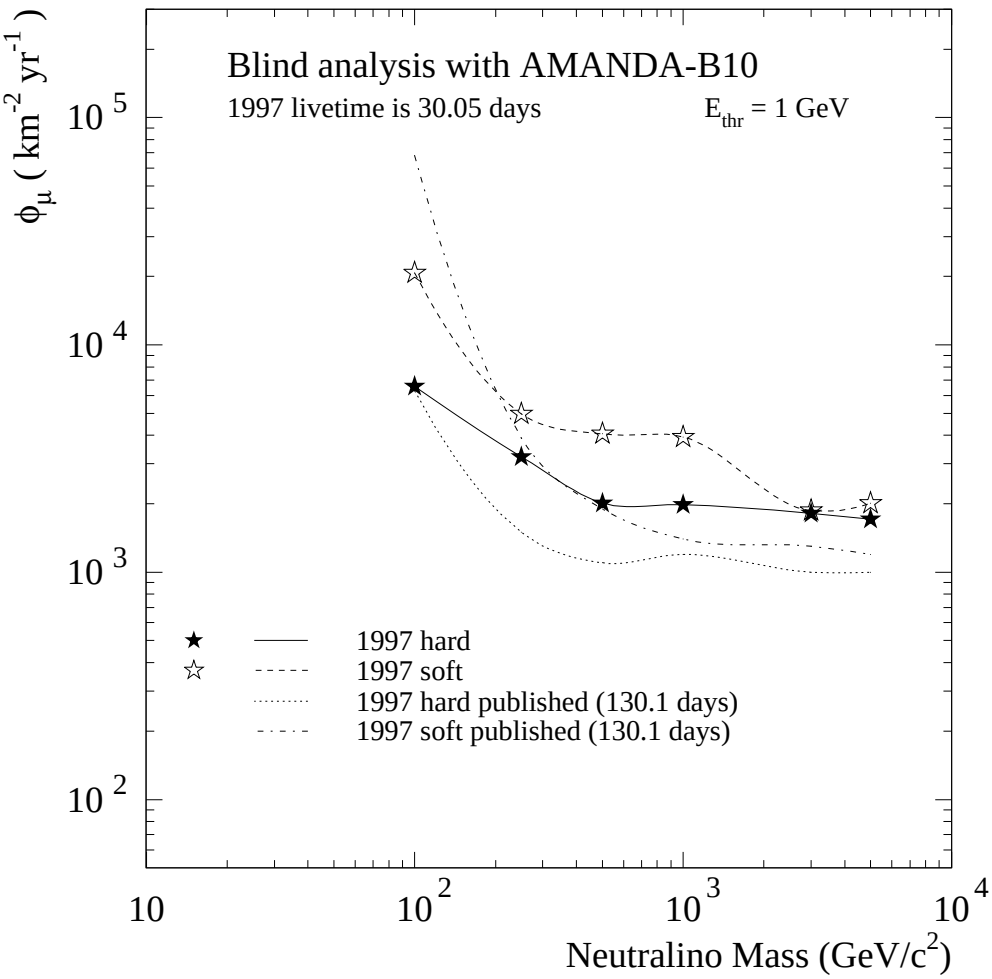

Figure C.1: The limits for the cut optimisation sample of 1997 data corresponding to 30.05 days of livetime. The published limits for the old 1997 analysis, full 130.1 days, is shown for comparison.

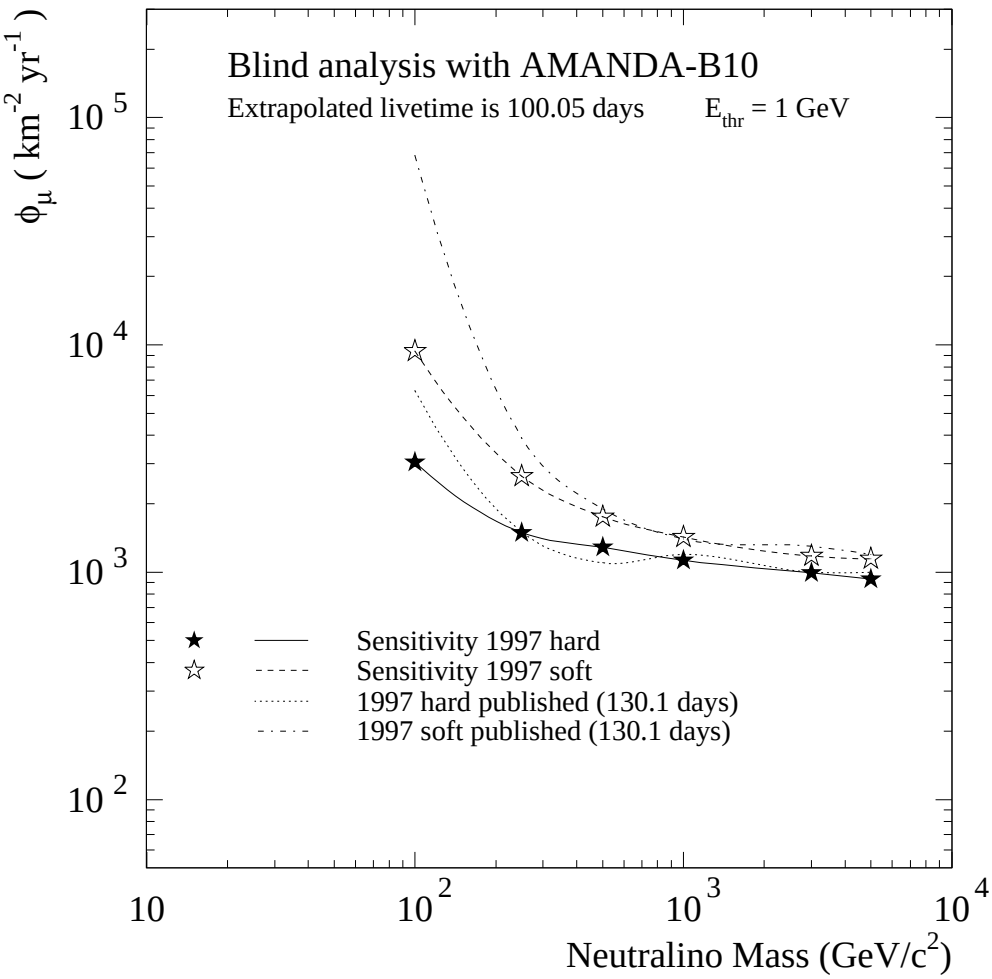

Figure C.2: The sensitivity for the unblinded sample of 1997 data corresponding to 100.05 days of livetime. The published limits for the old 1997 analysis, full 130.1 days, is shown for comparison.

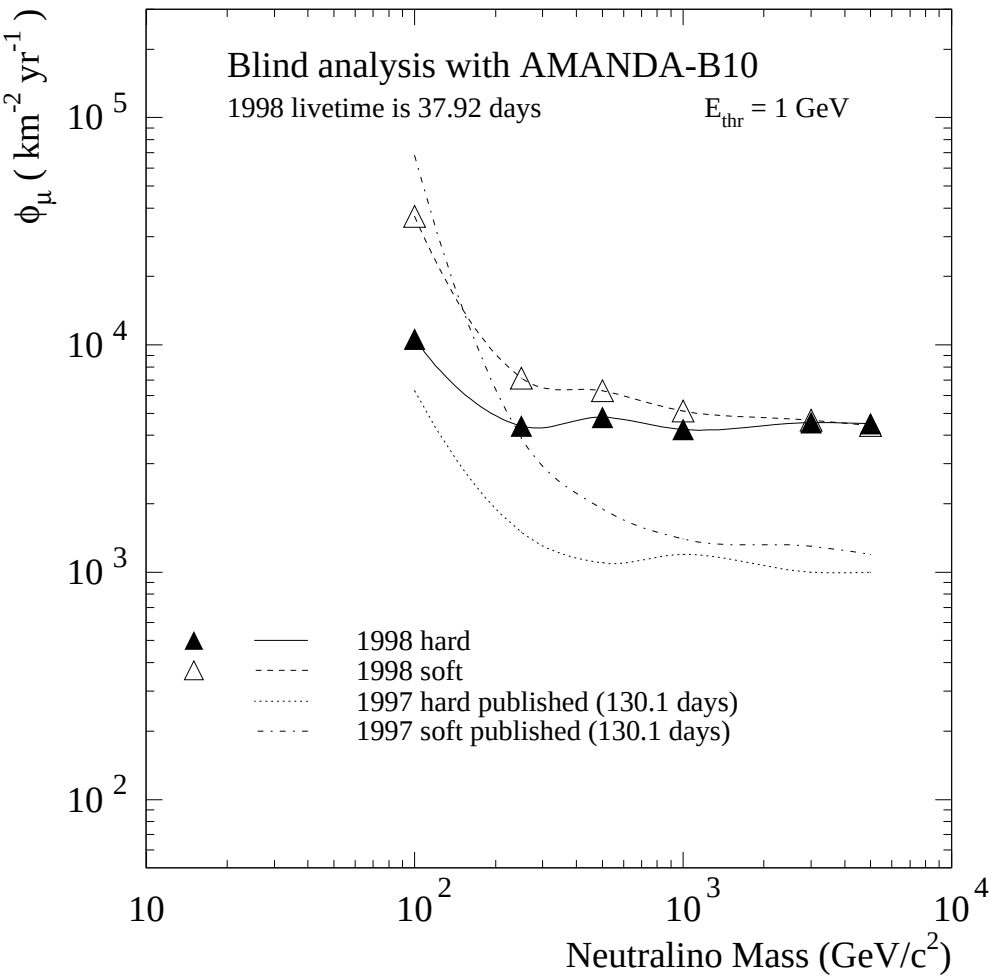

Figure C.3: The limits for the cut optimisation sample of 1998 data corresponding to 37.92 days of livetime. The published limits for the old 1997 analysis, full 130.1 days, is shown for comparison.

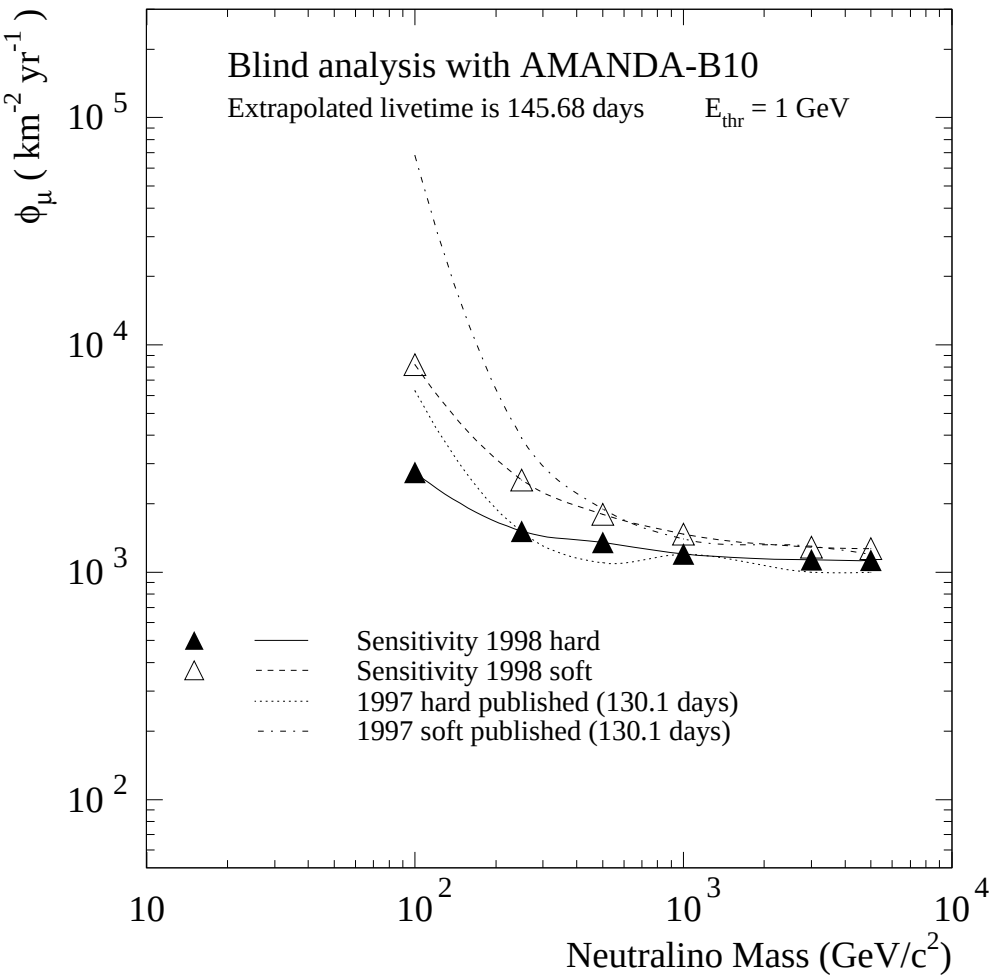

Figure C.4: The sensitivity for the unblinded sample of 1998 data corresponding to 145.68 days of livetime. The published limits for the old 1997 analysis, full 130.1 days, is shown for comparison.

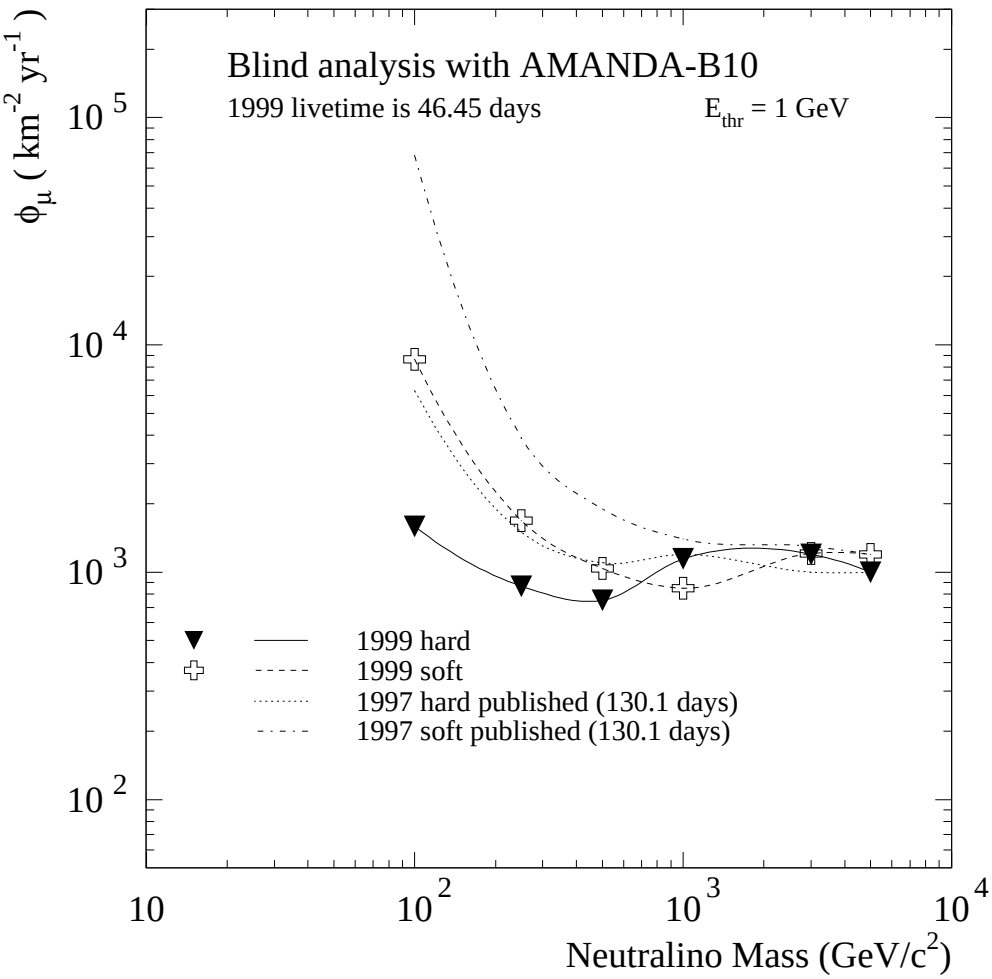

Figure C.5: The limits for the cut optimisation sample of 1999 data corresponding to 46.45 days of livetime. The published limits for the old 1997 analysis, full 130.1 days, is shown for comparison.

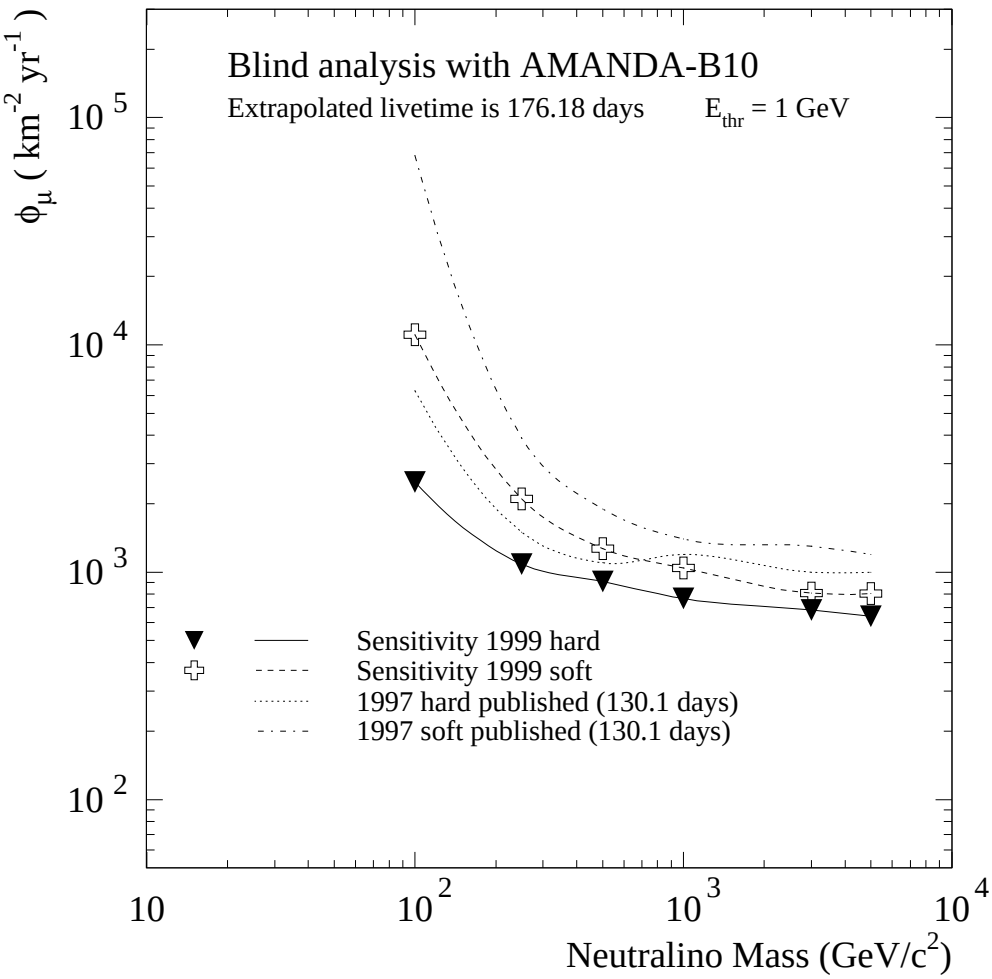

Figure C.6: The sensitivity for the unblinded sample of 1999 data corresponding to 176.18 days of livetime. The published limits for the old 1997 analysis, full 130.1 days, is shown for comparison.

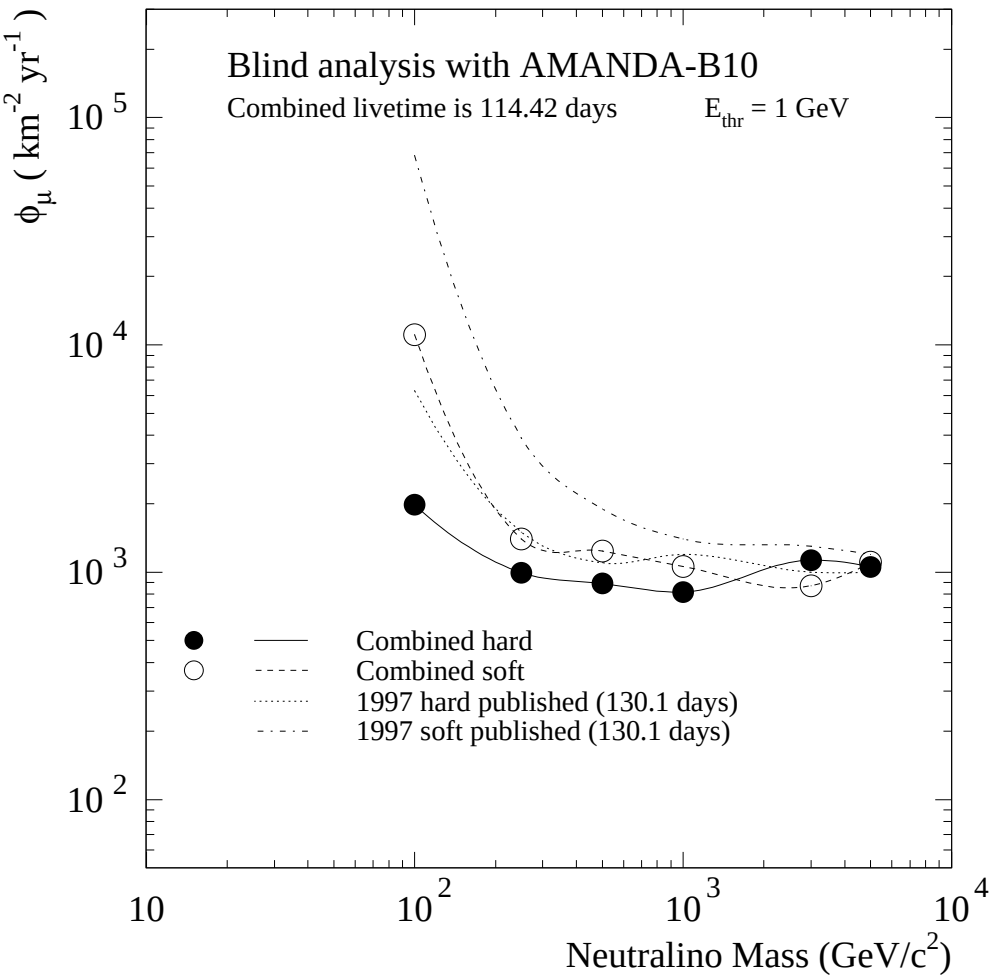

Figure C.7: The limits for the cut optimisation sample of combined 1997-99 data corresponding to 114.42 days of livetime. The published limits for the old 1997 analysis, full 130.1 days, is shown for comparison.

		Hard annihilation channels				Soft annihilation channels			
Year	M_χ	N_{data}	$N_{atm.\nu}$	μ_{90}^{FC}	ϕ_μ^{FC}	N_{data}	$N_{atm.\nu}$	μ_{90}^{FC}	ϕ_μ^{FC}
	100	2	1.4	4.5	10497.3	2	1.6	4.3	33980.1
	250	1	0.7	3.7	4912.8	1	1.1	3.3	6959.0
1997	500	1	0.7	3.7	4027.6	1	0.7	3.7	5761.5
	1000	0	0.4	2.0	2241.8	1	0.7	3.7	3343.3
	3000	0	0.3	2.2	2311.5	0	0.4	2.0	2332.4
	5000	0	0.3	2.2	2159.6	0	0.4	2.0	2273.8
	100	3	1.3	6.0	15205.5	4	1.4	7.1	57533.2
	250	1	0.5	3.8	6195.0	1	0.5	3.8	11154.1
1998	500	1	0.4	4.0	6354.0	1	0.4	4.0	8956.1
	1000	1	0.4	4.0	5873.8	1	0.4	4.0	6888.0
	3000	1	0.3	4.1	5939.7	1	0.4	4.0	6320.3
	5000	1	0.3	4.1	5623.4	1	0.3	4.1	6498.1
	100	0	2.5	1.2	2076.8	0	2.4	1.2	9868.5
	250	0	1.4	1.4	1177.7	0	1.6	1.3	1979.8
1999	500	0	0.7	1.8	1463.2	0	1.4	1.4	1362.6
	1000	0	0.6	1.9	1427.9	0	1.1	1.5	1253.7
	3000	0	0.5	1.9	1316.6	0	0.6	1.9	1510.6
	5000	0	0.6	1.9	1202.1	0	0.6	1.9	1465.6

Table C.6: The Feldman-Cousins flux limits without including systematic uncertainties for the three cut optimisation samples, the respective livetime is 30.05 days (1997), 37.92 days (1998) and 46.45 days (1999). M_χ is given in units of GeV/c^2 and ϕ_μ^{FC} in km^{-2}yr^{-1}.

Acknowledgements

There are many people to whom I owe a debt of gratitude for the things that I have learned on the subject matter of this thesis and from whom it in the end has benefited.

I would especially like to thank my supervisor Prof. Per Olof Hulth for his support and inspiration over the years. I am also greatly indebted to my second thesis advisor Doc. Christian Walck who has helped and encouraged me during the ups and downs of this work. As I started out as a Ph.D. student I spent some time at UC Berkeley and I would like to acknowledge Prof. Buford Price for the support I got while I was staying there. I must also thank Priv. Doz. Dr. Dr. Wolfgang Rhode who brought me to Wuppertal and supported me for two years, during that time the elements of the final analysis started to fall into place.

As a member of the AMANDA collaboration I have of course benefited from the work of the other members and I thank you all. Thanks as well to all support people who have contributed during the construction of AMANDA as well as the data taking itself (thank you winter overs!). With respect to the data analysis I am grateful for the work of Dr. Jodi Lamoreaux on the offline data processing and level two filtering of the 1997-99 data. I also have to salute all the people who have worked on the code used for simulation and reconstruction of AMANDA data. A special thanks goes to Torsten Harenberg who found a way to speed up CORSIKA by a factor of 20, to Dr. Dmitry Chirkin for his work with dCORSIKA and MMC, to Dr. Joakim Edsjö for WIMPSIMP and to Dr. Carlos Perez de los Heros and Anna Davour for their work with GENNIUP. Apart from the people already mentioned the analysis have benefited from discussions with Prof. Klas Hultqvist, Prof. Allan Hallgren, Dr. Tyce deYoung, Dr. Ignacio Taboada, Dr. Stephan Hundertmark and Heiko Geenen.

I have to thank everybody in the particle physics group in Stockholm for the time spent there, especially my past and present AMANDA colleagues Dr. Adam Bouchta, Dr. Eva Dalberg, Dr. Julio Rodriguez Martino, Yulia Mineava and Thomas and Christin Burgess. The same goes for all the people in the astroteilchen group in Wuppertal, it truly was a blast. Finally I have to thank my friends and family who have kept me reasonably sane over the years.

Bibliography

[1] Y. Mineava, Ph.D. thesis, "Search for Neutralino Dark Matter with the AMANDA-II Neutrino Telescope", Stockholm University, 2004.

[2] J. Ahrens *et al.*, *Astrophys. J.* **583** (2003) 1040

[3] J. Ahrens *et al.*, *Phys. Rev. Lett.* **92** (2004) 071102

[4] J. Ahrens *et al.*, *Phys. Rev. Lett.* **90** (2003) 251101

[5] J. Ahrens *et al.*, *Phys. Rev.* **D67** (2003) 012003

[6] R. Hardtke *et al.*, Proceedings of the XXVIII International Cosmic Ray Conference (ICRC), Tsukuba, Japan, (2003) 2717

[7] S. Hundertmark *et al.*, Proceedings of the XXVIII International Cosmic Ray Conference (ICRC), Tsukuba, Japan, (2003) 1309

[8] P. Niessen *et al.*, Proceedings of the XXVII International Cosmic Ray Conference (ICRC), Hamburg, Germany, (2001) 1496

[9] J. Ahrens *et al.*, *Astropart. Phys.* **16** (2002) 345

[10] P. Desiati *et al.*, Proceedings of the XXVII International Cosmic Ray Conference (ICRC), Hamburg, Germany, (2001) 985

[11] J. Rodriguez Martino, Ph.D. thesis, "A Study of the AMANDA Detector Using Atmospheric Muons", Stockholm University, 2003.

[12] D. A. Chirkin, Ph.D. thesis, "Cosmic Ray Energy Spectrum Measurement with the Antarctic Muon and Neutrino Detector Array (AMANDA)", University of California at Berkeley, 2003.

[13] E. Andrés *et al.*, *Nature* **410** (2001) 441

[14] J. Ahrens *et al.*, *Phys. Rev.* **D66** (2002) 012005

[15] H. Geenen *et al.*, Proceedings of the XXVIII International Cosmic Ray Conference (ICRC), Tsukuba, Japan, (2003) 1313

[16] F. Zwicky, *Astrophys. J.* **86** (1937) 217

[17] F. Zwicky, *Helv. Phys. Acta* **6** (1933) 110

[18] F. Zwicky, *Phys. Rev.* **51** (1937) 290

[19] F. Zwicky, *Phys. Rev.* **51** (1937) 679

[20] V. C. Rubin and W. K. Ford Jr., *Astrophys. J.* **159** (1970) 379

[21] M. S. Roberts and R. N. Whitehurst, *Astrophys. J.* **201** (1975) 327

[22] T. Takamiya and Y. Sofue, *Astrophys. J.* **534** (2000) 670

[23] W. Forman, C. Jones and W. Tucker, *Astrophys. J.* **293** (1985) 102

[24] H. J. Rood, T. L. Page, E. C. Kintner and I. R. King, *Astrophys. J.* **175** (1972) 627

[25] S. W. Allen and A. C. Fabian, *Mon. Not. R. Astron. Soc.* **269** (1994) 409

[26] N. Kaiser and G. Squires, *Astrophys. J.* **404** (1993) 441

[27] G. Squires *et al.*, *Astrophys. J.* **461** (1996) 572

[28] N. A. Bahcall, L. M. Lubin and V. Dorman, *Astrophys. J.* **447** (1995) L81

[29] G. Wilson, N. Kaiser and G. A. Luppino, *Astrophys. J.* **556** (2001) 601

[30] S. Burles, K. M. Nollett and M. S. Turner, *Phys. Rev.* **D63** (2001) 063512

[31] S. Burles, K. M. Nollett and M. S. Turner, *Astrophys. J.* **552** (2001) L1

[32] R. H. Dicke, P. J. E. Peebles, P. G. Roll and D. T. Wilkinson, *Astrophys. J.* **142** (1965) 414

[33] A. A. Penzias and R. W. Wilson, *Astrophys. J.* **142** (1965) 419

[34] G. F. Smoot *et al.*, *Astrophys. J.* **396** (1992) L1

[35] D. N. Spergel *et al.*, *Astrophys. J. Suppl.* **148** (2003) 1

[36] D. N. Spergel *et al.*, *Astrophys. J. Suppl.* **148** (2003) 135

[37] D. N. Spergel *et al.*, *Astrophys. J. Suppl.* **148** (2003) 175

[38] C. Alcock *et al.*, *Astrophys. J.* **542** (2000) 281

[39] C. Alcock *et al.*, *Astrophys. J.* **550** (2001) L169

[40] C. Afonso *et al.*, *Ast. & Astrophys.* **344** (1999) L63

[41] C. Afonso *et al.*, *Ast. & Astrophys.* **400** (2003) 951

[42] R. Schaeffer and J. Silk, *Astrophys. J.* **332** (1988) 1

[43] B. Lee and S. Weinberg, *Phys. Rev. Lett.* **39** (1977) 165

[44] J. E. Gunn *et al.*, *Astrophys. J.* **223** (1978) 1015

[45] P. Fayet, *Phys. Lett. B* **69** (1977) 489

[46] H. Goldberg, *Phys. Rev. Lett.* **50** (1983) 1419

[47] J. Ellis, J. S. Hagelin, D. V. Nanopoulos and M Srednicki, *Phys. Lett.* **B127** (1983) 233

[48] H. Pagels and J. R. Primack, *Phys. Rev. Lett.* **48** (1982) 223

[49] S. Weinberg, *Phys. Rev. Lett.* **48** (1982) 1303

[50] J. Ipser and P. Sikivie, *Phys. Rev. Lett.* **50** (1983) 925

[51] F. W. Stecker and Q. Shafi, *Phys. Rev. Lett.* **50** (1983) 928

[52] R. D. Peccei and H. R. Quinn, *Phys. Rev. Lett.* **38** (1977) 1440

[53] S. Weinberg, *Phys. Rev. Lett.* **40** (1978) 223

[54] F. Wilczek, *Phys. Rev. Lett.* **40** (1978) 279

[55] K. Griest and M. Kamionkowski, *Phys. Rev. Lett.* **64** (1990) 615

[56] D. J. H. Chung, E. W. Kolb and A. Riotto, *Phys. Rev. Lett.* **81** (1998) 4048

[57] I. F. M. Albuquerque, L. Hui and E. W. Kolb, *Phys. Rev.* **D64** (2001) 083504

[58] J. L. Feng, A. Rajaraman and F. Takayama, *Phys. Rev. Lett.* **91** (2003) 011302

[59] J. L. Feng, A. Rajaraman and F. Takayama, *Phys. Rev.* **D68** (2003) 063504

[60] K. Benakli, J. Ellis and D. V. Nanopoulos, *Phys. Rev.* **D59** (1999) 047301

[61] R. H. Cyburt, J. Ellis, B. D. Fields and K. A. Olive, *Phys. Rev.* **D67** (2003) 103521

[62] S. G. Ryan *et al.*, *Astrophys. J.* **530** (2000) L57

[63] P. Sikivie, *Phys. Rev. Lett.* **51** (1983) 1415

[64] R. Bernabei *et al.*, *Phys. Lett.* **B424** (1998) 195

[65] R. Bernabei *et al.*, *Phys. Lett.* **B480** (2000) 23

[66] P. Belli, R. Cerulli, N. Fornengo and S. Scopel, *Phys. Rev.* **D61** (2000) 023512

[67] P. Belli, R. Cerulli, N. Fornengo and S. Scopel, *Phys. Rev.* **D66** (2002) 043503

[68] A. M. Green, *Phys. Rev.* **D68** (2003) 023004

[69] D. Abrams *et al.*, *Phys. Rev.* **D66** (2002) 122003

[70] R. Abusaidi *et al.*, *Phys. Rev. Lett.* **84** (2002) 05699

[71] A. Benoit *et al.*, *Phys. Lett.* **B513** (2001) 15

[72] A. Benoit *et al.*, *Phys. Lett.* **B545** (2002) 43

[73] D. S. Akerib *et al.*, *Phys. Rev.* **D68** (2003) 082002

[74] L. Baudis *et al.*, *Phys. Rev.* **D63** (2001) 022001

[75] H. V. Klapdor-Kleingrothaus *et al.*, *Astropart. Phys.* **18** (2003) 525

[76] L. Baudis *et al.*, *Phys. Rev.* **D59** (1999) 022001

[77] A. Morales *et al.*, *Phys. Lett.* **B532** (2002) 8

[78] I. F. M. Albuquerque and L. Baudis, *Phys. Rev. Lett.* **90** (2003) 221301

[79] I. F. M. Albuquerque and L. Baudis, *Phys. Rev. Lett.* **91** (2003) 229903

[80] W. U. Wuensch *et al.*, *Phys. Rev.* **D40** (1989) 3153

[81] C. Hagmann *et al.*, *Phys. Rev.* **D42** (1990) 1297

[82] S. Asztalos *et al.*, *Phys. Rev.* **D64** (2001) 092003

[83] L. Bergström, J. Edsjö and P. Ullio, *Phys. Rev.* **D58** (1998) 083507

[84] H. A. Mayer-Hasselwander *et al.*, *Ast. & Astrophys.* **335** (1998) 161

[85] P. Sreekumar *et al.*, *Astrophys. J.* **494** (1998) 523

[86] P. Ullio, L. Bergström, J. Edsjö and F. Lacey, *Phys. Rev.* **D66** (2002) 123502

[87] P. Jean *et al.*, *Ast. & Astrophys.* **407** (2003) L55

[88] C. Tyler, *Phys. Rev.* **D66** (2002) 023509

[89] F. A. Aharonian *et al.*, *Ast. & Astrophys.* **400** (2003) 153

[90] M. Kamionkowski and M. S. Turner, *Phys. Rev.* **D43** (1991) 1774

[91] S. W. Barwick *et al.*, *Astrophys. J.* **482** (1997) L191

[92] E. A. Baltz and J. Edsjö, *Phys. Rev.* **D59** (1999) 023511

[93] E. A. Baltz, J. Edsjö, K. Freese and P. Gondolo, *Phys. Rev.* **D59** (1999) 023511

[94] L. Bergström, J. Edsjö and P. Ullio, *Astrophys. J.* **526** (1999) 215

[95] S. Orito *et al.*, *Phys. Rev. Lett.* **84** (2000) 1078

[96] M. M. Boliev *et al.*, *Nucl. Phys. B (Proc. Suppl.)* **48** (1996) 83

[97] M. Ambrosio *et al.*, *Phys. Rev.* **D60** (1999) 082002

[98] Y. Fukuda *et al.*, *Phys. Rev. Lett.* **82** (1999) 2644

[99] Y. Fukuda *et al.*, *Phys. Lett.* **B467** (1999) 185

[100] A. Habig *et al.*, Proceedings of the XXVII International Cosmic Ray Conference (ICRC), Hamburg, Germany, (2001) 1558

[101] I. A. Belolaptikov *et al.*, *Astropart. Phys.* **7** (1997) 263

[102] V. Ayutdinov *et al.*, Proceedings of the XXVIII International Cosmic Ray Conference (ICRC), Tsukuba, Japan, (2003) 1353

[103] E. Andrés *et al.*, *Astropart. Phys.* **13** (2000) 1

[104] J. Ahrens *et al.*, *Phys. Rev.* **D66** (2002) 032006

[105] V. S. Berezinskii and G. T. Zatsepin, *Sov. Phys. Usp.* **20** (1977) 361

[106] S. Matsuno *et al.*, *Nucl. Instrum. Meth.* **A276** (1989) 359

[107] J. Babson *et al.*, *Phys. Rev.* **D42** (1990) 3613

[108] D. M. Lowder *et al.*, *Nature* **353** (1991) 331

[109] S. Barwick *et al.*, *J. Phys. G: Nucl. Part. Phys.* **18** (1992) 225

[110] D. Chirkin and W. Rhode, Proceedings of the XXVII International Cosmic Ray Conference (ICRC), Hamburg, Germany, (2001) 1017

[111] P. Askebjer *et al*, *Science* **267** (1995) 1147

[112] P. Askebjer *et al*, *Geophys. Res. Lett.* **24** (1997) 1355

[113] K. Woshnagg *et al*, Proceedings of the XXVI International Cosmic Ray Conference (ICRC), Salt Lake City, USA, (1999) HE.4.1.5

[114] P. B. Price, K. Woschnagg and D. Chirkin, *Geophys. Res. Lett.* **27** (2000) 2129

[115] K. Woshnagg, Private communication (2004), In preparation for publication

[116] R. Gandhi, C. Quigg, M. H. Reno and Ina Sarcevic, *Astropart. Phys.* **5** (1996) 81

[117] R. Gandhi, C. Quigg, M. H. Reno and Ina Sarcevic, *Phys. Rev.* **D58** (1998) 093009

[118] P. B. Price, *Science* **267** (1995) 1802

[119] R. Porrata, Ph.D. thesis, "The Energy Spectrum of Pointlike Events in AMANDA-A", University of California at Irvine, 1997.

[120] P. Ekström, "Simulation and Analysis Methods for Large Neutrino Telescopes", ed. C. Spiering, DESY-PROC-1999-01, 420.

[121] A. Bouchta, "A Preliminary Position Calibration of the Amanda-B Detector", *USIP Report 97-02*, Stockholm University, 1997

[122] D. Heck *et al.*, "Corsika: A Monte Carlo Code to Simulate Extensive Air Showers", FZKA Report No. 6019, Forschungszentrum Karlsruhe, 1998.

[123] J. Wentz *et al.*, *Phys. Rev.* **D67** (2003) 073020

[124] B. Wiebel-Sooth, Ph.D. thesis, "Measurement of the Allparticle Spectrum and Chemical Composition of Cosmic-Rays with the HEGRA Detector", Universität Wuppertal, 1998

[125] G. C. Hill, *Astropart. Phys.* **6** (1997) 215

[126] P. Lipari, *Astropart. Phys.* **1** (1993) 195

[127] A. M. Dziewonski and D. L. Anderson, *Phys. Earth Plan. Inter.* **25** (1981) 297

[128] A. D. Martin, W. J. Stirling and R. G. Roberts, *Phys. Lett.* **B354** (1995) 155

[129] J. Edsjö, Ph.D. thesis, "Aspects of Neutrino Detection of Neutralino Dark Matter", Uppsala University, 1997

[130] L. Bergström, J. Edsjö and P. Gondolo, *Phys. Rev.* **D55** (1997) 1765

[131] L. Bergström, J. Edsjö and P. Gondolo, *Phys. Rev.* **D58** (1998) 103519

[132] T. Sjöstrand *et al.*, *Comp. Phys. Comm.* **135** (2001) 238

[133] S. Hundertmark, "Simulation and Analysis Methods for Large Neutrino Telescopes", ed. C. Spiering, DESY-PROC-1999-01, 276.

[134] A. Karle, "Simulation and Analysis Methods for Large Neutrino Telescopes", ed. C. Spiering, DESY-PROC-1999-01, 174.

[135] P. Miočinović, Ph.D. thesis, "Muon energy reconstruction in the Antarctic Muon And Neutrino Detector Array (AMANDA)", University of California at Berkeley, 2001.

[136] P. Miočinović and P. Niessen, Proceedings of the XXVIII International Cosmic Ray Conference (ICRC), Tsukuba, Japan, (2003) 1341

[137] J. Ahrens *et al*, "Muon Track Reconstruction and Data Selection Techniques in AMANDA", *Nucl. Instrum. Meth.* **A** (2004), Article in Press

[138] D. Pandel, Diploma thesis, "Bestimmung von Wasser- und Detektorparametern und Rekonstruktion von Myonen bis 100 TeV mit dem Baikal-Neutrinoteleskop NT-72", Humboldt-Universität zu Berlin, 1996.

[139] I. Taboada, Ph.D. thesis, " Search for High Energy Neutrino Induced Cascades with the AMANDA-B10 Detector", University of Pennsylvania, March 2002

[140] J. Schwindling and B. Mansoulié, "MLPfit: a tool for Multi-Layer Perceptrons", http://schwind.home.cern.ch/schwind/MLPfit.html

[141] G. C. Hill and K. Rawlins, *Astropart. Phys.* **19** (2003) 393

[142] G. J. Feldman and R. D. Cousins, *Phys. Rev.* **D57** (1998) 3873

[143] A. G. Frodesen, O. Skjeggestad and H. Tøfte, "Probability and statistics in particle physics", Universitesforlaget 1979

[144] E. Dalberg, Ph.D. thesis, "A Search for Neutralino Dark Matter with the AMANDA-B10 Detector", Stockholm University, 1999.

[145] J. Conrad, O. Botner, A. Hallgren and C. Pérez de los Heros, *Phys. Rev.* **D67** (2003) 012002

[146] J. Conrad, *Comp. Phys. Comm.* **158** (2004) 117

[147] R. D. Cousins and V. L. Highland, *Nucl. Instrum. Meth.* **A320** (1992) 331

[148] A. Biron and H. Wissing, "Impact of Varied OM Sensitivities on the AMANDA-B10 Analysis", AMANDA Internal Report/20001202, 2000

[149] M. Boliev *et al.*, Proceedings of Dark Matter in Astro- and Particle Physics, ed. H. V. Klapdor-Kleingrothaus and Y. Ramachers, World Scientific, (1997) 711. See also O. Suvorova, hep-ph/9911415

[150] S. Desai, talk at Identification of Dark Matter, 2002, York, England

[151] J. Lundberg and J. Edsjö, "WIMP diffusion in the solar system including solar depletion and its effect on Earth capture rates", Accepted for publication in *Phys. Rev.* **D** (2004)

[152] A. Gould, *Astrophys. J.* **368** (1991) 610

[153] P. Mock, *Private communication*

[154] K. Woschnagg, *Private Communication*